

DETECTION OF CYANIDE IONS USING CHEMOSENSING
ENSEMBLES UNDER INDICATOR DISPLACEMENT
ASSAYS

Miss Ratanakorn Teerasarunyanon



A Dissertation Submitted in Partial Fulfillment of the Requirements
for the Degree of Doctor of Philosophy in Chemistry
Department of Chemistry
FACULTY OF SCIENCE
Chulalongkorn University
Academic Year 2019
Copyright of Chulalongkorn University

การตรวจวัดไอออนไนซ์โดยใช้เอนเซมเบิลรับรู้ทางเคมีภายใต้การทดสอบการแทนที่อินดิเค
เตอร์



วิทยานิพนธ์นี้เป็นส่วนหนึ่งของการศึกษาตามหลักสูตรปริญญาวิทยาศาสตรดุษฎีบัณฑิต
สาขาวิชาเคมี ภาควิชาเคมี
คณะวิทยาศาสตร์ จุฬาลงกรณ์มหาวิทยาลัย
ปีการศึกษา 2562
ลิขสิทธิ์ของจุฬาลงกรณ์มหาวิทยาลัย

รัตนกร ชีรสรณ์ชานนท์ : การตรวจวัดไอออนไซยาไนด์โดยใช้เอนไซม์รับรู้ทางเคมีภายใต้การทดสอบการแทนที่อินดิเคเตอร์. (DETECTION OF CYANIDE IONS USING CHEMOSENSING ENSEMBLES UNDER INDICATOR DISPLACEMENT ASSAYS) อ.ที่ปรึกษาหลัก :
ศ. ดร.ธวัชชัย คັນทุลาณี

การรับรู้แอนไอออนเป็นสาขาที่น่าสนใจของงานวิจัยกว่าทศวรรษที่ผ่านมา เนื่องจากแอนไอออนมีบทบาทสำคัญหลากหลายในกระบวนการทางเคมี ชีวภาพ และสิ่งแวดล้อม ด้วยเหตุนี้ในวิทยานิพนธ์ฉบับนี้ได้รายงานสามโครงการที่น่าสนใจของการรับรู้แอนไอออนสำหรับการประยุกต์ใช้ในการตรวจจับแอนไอออนฟลูออไรด์และไซยาไนด์

โครงการแรกของวิทยานิพนธ์ศึกษาเคมีของสารประกอบแอนทราซีนที่มีหมู่แทนที่ชนิดโดเมซิลัลบอร์ลหนึ่งและสองหมู่ (สารประกอบ 1 และ 2 ตามลำดับ) สำหรับการจับกับฟลูออไรด์และไซยาไนด์ การศึกษาทั้งหมดให้ข้อมูลเชิงลึกเกี่ยวกับโครงสร้างอิเล็กทรอนิกส์และผลของการจับแอนไอออน ผลการทดลองระบุว่าสารประกอบแอนทราซีนทั้งสองชนิดมีค่าการจับฟลูออไรด์และไซยาไนด์ที่สูงและจับในอัตราส่วนหนึ่งต่อหนึ่งของอัตราส่วน โยสต์-เกสต์และให้ผลยูวีและฟลูออเรสเซนซ์ที่แตกต่างเนื่องจากโครงสร้างอิเล็กทรอนิกส์ที่จำเพาะ

วิธีเอนไซม์รับรู้ทางเคมีเป็นหนึ่งในวิธีที่ได้รับความนิยมอย่างมากสำหรับการตรวจจับแอนไอออน การใช้วิธีการนี้เพื่อตรวจจับแอนไอออนไซยาไนด์ซึ่งมีความเป็นพิษเป็นหัวข้อวิจัยที่จะกล่าวถึงในโครงการที่สองและสาม ในโครงการที่สองการตรวจจับไซยาไนด์สามารถทำได้โดยใช้สารประกอบเชิงซ้อนชนิดโคออร์ดิเนชันของคอปเปอร์ (II) กับลิแกนด์ชนิดแอนทราซีนที่มีไดโรโพลีเอมีนสองหน่วย ($\text{Cu}_2\text{L1}$) เป็นตัวรับรู้และไฟโรกลอสเลอร์ (PGR) เป็นอินดิเคเตอร์ เอนไซม์ $\text{Cu}_2\text{L1-PGR}$ สามารถตรวจจับไซยาไนด์อย่างเฉพาะเจาะจงและได้ค่าขีดจำกัดการตรวจวัดเท่ากับ 0.029 ppm การคำนวณ TD / DFT ระบุว่าที่สภาวะสมดุล $\text{Cu}_2\text{L1-2PGR-2CN}^-$ ซึ่งมีความเสถียรที่สุดเป็นสปีชีส์หลักที่พบในสารละลาย

โครงการสุดท้ายมุ่งเน้นไปที่การพัฒนากระบวนการตรวจจับฟลูออโรเมทริกและการวัดสีซึ่งทำใ้ได้ง่ายและประหยัดค่าใช้จ่ายได้ทำการทดสอบกับเอนไซม์ของอินดิเคเตอร์อริซารินเรคเอส (ARS) และตัวรับรู้อนุพันธ์ของฟีนิลบอร์อนิกหลายชนิด พบว่าการตรวจจับไซยาไนด์ที่ดีที่สุดทำได้ด้วยการแทนที่อินดิเคเตอร์ในเอนไซม์ของ ARS และตัวรับรู้ชนิด 3-ไนโตรฟีนิลบอร์อนิก แอซิด (NPBA) สภาวะที่เหมาะสมสำหรับใช้ตรวจวัดไอออนไซยาไนด์ในระบบตรวจจับนี้คือ ARS-NPBA จับกับในอัตราส่วนหนึ่งต่อสี่ในสารละลายฟอสเฟตบัฟเฟอร์ความเข้มข้น 0.01 โมลาร์ ที่พีเอช 8.0

จุฬาลงกรณ์มหาวิทยาลัย
CHULALONGKORN UNIVERSITY

สาขาวิชา เคมี
ปีการศึกษา 2562

ลายมือชื่อผู้คิด
ลายมือชื่อ อ.ที่ปรึกษาหลัก

5772883723 : MAJOR CHEMISTRY

KEYWORD: Anion recognition, Fluoride sensing, Cyanide sensing, Indicator displacement assay, Lewis acid, Copper complex, Boronic acid, Alizarin Red S

Ratanakorn Teerasarunyanon : DETECTION OF CYANIDE IONS USING CHEMOSENSING ENSEMBLES UNDER INDICATOR DISPLACEMENT ASSAYS. Advisor: Prof. THAWATCHAI TUNTULANI

Anion recognition is an attractive area of research in recent decades as anions play an important role in a wide range of chemical, biological, and environmental processes. This dissertation reports three projects dedicated to anion recognition with applications in fluoride and cyanide sensing.

The first project of the dissertation describes the chemistry of two novel anthracene derivatives bearing one and two dimesitylboryl substituents (compounds 1 and 2, respectively) for the complexation of anions. All investigations provide insights into the electronic structure and effect of fluoride and cyanide binding. The results demonstrate that these boranes have a high affinity for fluoride and cyanide anions which form a 1 : 1 guest-host complex and display differences in UV-vis and fluorescence response due to their unique electronic structures.

Chemosensing ensemble approach is one of the main strategies gained considerable interest for anion sensing. Utilizing this approach to detect the toxic cyanide anion is the subject of the research discussed in the second and third projects. In the second project, colorimetric detection of cyanide is accomplished using dinuclear copper(II) complex of anthracene containing two tripodal tetramine moieties ($\text{Cu}_2\text{L1}$) as a receptor, and pyrogallol red (PGR) as an indicator. The $\text{Cu}_2\text{L1}$ -PGR ensemble is able to detect cyanide selectively with limit of detection of 0.029 ppm. TD/DFT calculations indicate that the most stable $\text{Cu}_2\text{L1}$ -2PGR-2 CN^- complex is the dominant species in the equilibrium mixtures of the solution.

Finally, the last project focuses on the development of fluorometric and colorimetric sensing system, which is simple, rapid and cost-effective. Many ensembles using alizarin red S (ARS) as indicator and derivatives of phenyl boronic acid as receptor are tested. The best detection of cyanide is achieved by displacing the indicator in the ensemble of ARS indicator and 3-nitrophenyl boronic acid (NPBA) receptor. The optimum condition for the determination of cyanide ion by this sensing system is 1 : 4 ARS-NPBA complex in 0.01 M PBS pH 8.0.

Field of Study: Chemistry
Academic Year: 2019

Student's Signature
Advisor's Signature

ACKNOWLEDGEMENTS

First of all, I would like to express my sincere gratitude to my research advisor, Prof. Thawatchai Tuntulani, for great efforts he spent on my projects. I have learned tremendously from him throughout the duration of my Ph. D study. Very special thanks go to Prof. Vithaya Ruangpornvisuti for his help with computational studies. Without the assistance of him, this work would not have been possible.

I would also like to thank Prof. François Gabbai for providing me the opportunity to conduct collaborative research at Texas A&M University. Thanks to all members of the Gabbai group, especially: Dr. Lewis Wilkins and Gyeongjin Park for their mentorship and guidance during my stay in the U.S. It has been my great pleasure working with them and learning from them.

I would like to extend my sincere thanks to all my dissertation committee members, Assoc. Prof. Vudhichai Parasuk, Prof. Vithaya Ruangpornvisuti, Assist. Prof. Chomchai Suksai, and Assist. Prof. Pannee Leeladee for their fruitful discussions and valuable suggestions. I am deeply thankful to all current and former members of Supramolecular Chemistry Research Unit (SCRU) who are both friends and wonderful coworkers. Additionally, thanks to my family and friends for their love and constant support.

Finally, financial support from the Development and Promotion of Science and Technology Talent project (DPST) and the Center of Excellence on Petrochemical and Materials Technology (PETROMAT) are greatly acknowledged.

Ratanakorn Teerasarunyanon

TABLE OF CONTENTS

	Page
ABSTRACT (THAI)	iii
ABSTRACT (ENGLISH).....	iv
ACKNOWLEDGEMENTS.....	v
TABLE OF CONTENTS.....	vi
LIST OF FIGURES	x
LIST OF TABLES.....	xvi
LIST OF ABBREVIATIONS.....	xvii
CHAPTER I INTRODUCTION	1
1.1 Significance of anions	1
1.2 Chemosensor	2
1.3 Chemosensing ensemble	3
1.4 Anion recognition.....	4
1.4.1 Anion recognition by bifunctional boron Lewis acid.....	4
1.4.2 Anion recognition by metal complexes.....	6
1.4.3 Anion recognition by boronic acid.....	7
1.5 Project objectives.....	9
CHAPTER II ANION BINDING PROPERTIES OF 1-(DIMESITYLBORYL) ANTHRACENE AND 1,8-BIS(DIMESITYLBORYL)ANTHRACENE	12
2.1 Introduction.....	12
2.2 Results and discussion	16
2.2.1 Synthesis and characterization of 1-(dimesitylboryl)anthracene (1) and 1,8-bis(dimesitylboryl)anthracene (2)	16
2.2.2 Photophysical properties	25
2.2.3 Electrochemical properties	28
2.2.4 Quantum yields.....	29
2.2.5 Fluoride binding properties	30

3.4.2 Synthesis of Cu ₂ L1	69
3.4.3 Colorimetric and UV-vis experiments	69
3.4.4 Theoretical	70
3.4.4.1 Structure optimizations of all studied species	70
3.4.4.2 UV-vis simulations of all studied species	71
CHAPTER IV ALIZARIN RED S CONJUGATED BORONIC ACID ENSEMBLES FOR THE SELECTIVE DETERMINATION OF CYANIDE IN AQUEOUS MEDIA USING INDICATOR DISPLACEMENT ASSAY APPROACH	72
4.1 Introduction.....	72
4.2 Results and discussion	77
4.2.1 Studies of absorption and emission of ARS–NPBA ensemble	77
4.2.2 Optimization of parameters for cyanide detection	78
4.2.2.1 Effect of type of boronic acids	78
4.2.2.2 Effect of reaction time	81
4.2.2.3 Effect of NPBA concentration	81
4.2.2.4 Effect of pH and concentration of buffer	82
4.2.3 Studies of selectivity and cyanide sensing	84
4.2.4 Studies of limit of detection and interferences	86
4.2.5 Determination of cyanide in real water samples	88
4.2.6 Theoretical calculations.....	89
4.3 Conclusions.....	93
4.4 Experimental Section.....	93
4.4.1 General considerations	93
4.4.2 Spectroscopic experiments	94
4.4.3 Theoretical.....	96
4.4.3.1 DFT optimized structures in solution phases, energetics and thermodynamics properties.....	96
4.4.3.2 Simulated UV-vis and Fluorescence spectra	96
CHAPTER V CONCLUSIONS.....	98
REFERENCES	100

VITA..... 110
APPENDIX..... 111



จุฬาลงกรณ์มหาวิทยาลัย
CHULALONGKORN UNIVERSITY

LIST OF FIGURES

Chapter I

Figure 1.1	Schematic diagram showing binding of a guest by a chemosensor.....	2
Figure 1.2	Schematic diagram of two ensemble concepts (displacement and complexation).	3
Figure 1.3	Schematic representation of the switching of π -conjugation in the LUMO of boron-based π -electron systems.....	5
Figure 1.4	Colorimetric change of tris(9-anthryl)borane upon addition of F^- in THF.	5
Figure 1.5	Reaction of bifunctional boranes based 1,8-naphthalenediyl, and ortho-phenylene backbone with small nucleophilic anions.....	6
Figure 1.6	Examples of dinuclear copper [28] and zinc [29] complexes in M-IDA..	7
Figure 1.7	Various complexometric indicators commonly used in IDA.	7
Figure 1.8	The reversible formation of a cyclic boronate ester and oxidative removal of the boronic acid.	8
Figure 1.9	Diagram illustrating the change in geometry at the boron center on interaction with nucleophiles.	8
Figure 1.10	Schematic illustration of the receptor-reporter ensemble system [31].	8
Figure 1.11	Chemical structures of 1 and 2	9
Figure 1.12	Chemical structures of Cu_2L1	10
Figure 1.13	Proposed mechanism for detection of CN^- based on ARS and boronic acid derivatives.	11

Chapter II

Figure 2.1	Fluoride binding of triarylboranes.	12
Figure 2.2	Examples of some common monofunctional boranes I , II and III	13
Figure 2.3	Diboranes IV , V , VI and VII bind the fluoride anions to afford the corresponding chelating complexes.....	14
Figure 2.4	Diboranes VIII and IX bind the cyanide anions to afford the corresponding chelating complexes [51].	14
Figure 2.5	Examples of anthracene based diboranes (X and XI) and target compounds in this work (1 and 2).....	15
Figure 2.6	Synthetic overview of the mono- and bis-functionalized anthracene derivatives 1 and 2	16
Figure 2.7	1H NMR (400 MHz, $CDCl_3$, 298 K) spectrum of 1	17
Figure 2.8	^{13}C NMR (101 MHz, $CDCl_3$, 298 K) spectrum of 1	18
Figure 2.9	^{11}B NMR (128 MHz, $CDCl_3$, 298 K) spectrum of 1	18
Figure 2.10	HRMS (APCI $^+$) of $[1+H]^+$ observed (a) and calculated (b).....	19
Figure 2.11	1H NMR (400 MHz, $CDCl_3$, 298 K) spectrum of 2	19

Figure 2.12	^{13}C NMR (101 MHz, CDCl_3 , 298 K) spectrum of 2	20
Figure 2.13	^{11}B NMR (128 MHz, CDCl_3 , 298 K) spectrum of 2	20
Figure 2.14	HRMS (APCI $^+$) of $[\mathbf{2}+\text{H}]^+$ observed (a) and calculated (b).....	21
Figure 2.15	Solid-state structures of 1 (top) and 2 (bottom). Hydrogen atoms omitted for clarity. Thermal ellipsoids drawn at 50%.....	22
Figure 2.16	UV-vis spectra of pure anthracene (left), 1 (middle), and 2 (right).....	26
Figure 2.17	Depiction of LUMO, HOMO and HOMO-1 of 1 (left) and 2 (right). Isosurface value = 0.03.	27
Figure 2.18	Cyclic voltammograms of 1 (left) and 2 (right) in THF with 0.1 M TBAPF $_6$ as electrolyte, scan rate 200 mV/s and potential referenced to Fc/Fc $^+$	28
Figure 2.19	Quantum yield gradient plot of 1 (left) and 2 (right).	29
Figure 2.20	(a) Changes in UV-vis absorption spectra of 1 (6.0×10^{-5} M in THF) upon titration with TBAF. (b) Experimental and calculated 1:1 binding isotherm for the addition of F $^-$ to 1 , based on the absorbance measured at 388 nm.	30
Figure 2.21	^{11}B NMR spectra of 1 in CD_2Cl_2 solutions upon the addition of TBAF.	31
Figure 2.22	HRMS (ESI $^-$) of $[\mathbf{1}-\text{F}]^-$ observed (a) and calculated (b).....	31
Figure 2.23	(a) Changes in UV-vis absorption spectra of 2 (6.0×10^{-5} M in THF) upon titration with TBAF. (b) Experimental and calculated 1:1 binding isotherm for the addition of F $^-$ to 2 , based on the absorbance measured at 398 nm.	32
Figure 2.24	HRMS (ESI $^-$) of $[\mathbf{2}-\text{F}]^-$ observed (a) and calculated (b).....	32
Figure 2.25	Depiction of frontier molecular orbitals of $[\mathbf{1}-\text{F}]^-$ (left) and $[\mathbf{2}-\text{F}]^-$ (right). Isosurface value = 0.03.	33
Figure 2.26	Fluorescence emission spectra of 1 (a) and 2 (b) upon fluoride binding and their respective color changes when irradiated with UV light.	34
Figure 2.27	(a) Changes in UV-vis absorption spectra of 1 (6.0×10^{-5} M in THF) upon titration with TBACN. (b) Experimental and calculated 1:1 binding isotherm for the addition of CN $^-$ to 1 , based on the absorbance measured at 388 nm.....	35
Figure 2.28	(a) Changes in UV-vis absorption spectra of 2 (6.0×10^{-5} M in THF) upon titration with TBACN. (b) Experimental and calculated 1:1 binding isotherm for the addition of CN $^-$ to 2 , based on the absorbance measured at 398 nm.....	35
Figure 2.29	HRMS (ESI $^-$) of $[\mathbf{1}-\text{CN}]^-$ observed (a) and calculated (b).	36
Figure 2.30	HRMS (ESI $^-$) of $[\mathbf{2}-\text{CN}]^-$	37
Figure 2.31	Fluorescence emission spectra of 1 (a) and 2 (b) upon cyanide binding and their respective color changes when irradiated with UV light.	37
Figure 2.32	Diagrams showing the C-H unit at the 9 position of anthracene hindering the cyanide bridging mode.....	38
Figure 2.33	Two boranes bind the toxic fluoride and cyanide anions to afford the corresponding 1:1 complexes.	39

Chapter III

Figure 3.1	Anion recognition by a dinuclear metal coordination complex [66].	44
Figure 3.2	The chemical structure of dipicolylamine (DPA) ligand and Zn–DPA complex.	45
Figure 3.3	Examples of dinuclear Zn–DPA receptors employed in the IDA for the recognition of phosphorylated species.	46
Figure 3.4	Chemical structure of 2-[bis(2-pyridylmethyl)aminomethyl]aniline (left) and L1 (right).	47
Figure 3.5	Binding mechanism for cyanide of XVI in the presence of external indicators, Eosin Y and Fluorescein [28].	47
Figure 3.6	Chemical structure of a Cu ₂ L1 (left) and PGR indicator (right) denoted by L2 in this work.	48
Figure 3.7	The synthetic overview of Cu ₂ L1.	49
Figure 3.8	¹ H NMR (400 MHz, CDCl ₃) spectrum of ligand L1.	50
Figure 3.9	HRMS (ESI ⁺) of Cu ₂ L1.	50
Figure 3.10	(a) Changes in absorbance, and (b) Changes in color of PGR obtained by the titration of Cu ₂ L1 (400 μM) to a solution of PGR (20 μM).	51
Figure 3.11	(a) Changes in absorbance, and (b) Changes in color of the Cu ₂ L1–PGR ensemble (20 μM) in the presence of various anions (150 μM).	52
Figure 3.12	UV-vis spectra obtained for the addition of cyanide solution (1 mM) to a 1:1 ensemble solution of Cu ₂ L1–PGR (20 μM).	53
Figure 3.13	Calibration plot for detection of cyanide using Cu ₂ L1–PGR ensemble.	54
Figure 3.14	Sensing of cyanide in the presence of competitive anions (7.5 equivalents) in 20% (v/v) water-acetonitrile solution buffered at pH 7.4 with 10 mM HEPES; (1) = Cu ₂ L1–PGR ensemble + CN [−] , (2) = (1) + F [−] , (3) = (1) + Cl [−] , (4) = (1) + Br [−] , (5) = (1) + I [−] , (6) = (1) + AcO [−] , (7) = (1) + BzO [−] , (8) = (1) + ClO ₄ [−] , (9) = (1) + H ₂ PO ₄ [−] , (10) = (1) + OH [−] , (11) = (1) + NO ₃ [−] , (12) = (1) + SO ₄ ^{2−} , (13) = (1) + HPO ₄ ^{2−} , (14) = (1) + CO ₃ ^{2−} , (15) = (1) + SCN [−] and (16) = (1) + HCO ₃ [−] .	55
Figure 3.15	The CPCM/CAM-B3LYP/6-31G(d)-optimized structures of singlet-state complexes (a) [CuL1Cu/L2] ²⁺ and (b) [L2/CuL1Cu/L2] ⁰ .	57
Figure 3.16	The possible structures of [CuL1Cu/L2] ²⁺ and [L2/CuL1Cu/L2] ⁰ complexing with cyanide ion formed as (a) [CuL1Cu/L2/CN] ⁺ , (b) [L2/CuL1Cu/L2/CN] [−] and (c) [CN/L2/CuL1Cu/L2/CN] ^{2−} species, structure optimizations based on the CPCM/CAM-B3LYP/6-31G(d) computations.	59
Figure 3.17	(a) The measured UV-vis spectrum of PGR, matched with (b) the simulated UV-vis spectrum of the L2 ^{2−} species. The simulated UV-vis wavelength is scaled by 1.20 and its absorbance is scaled to the measurement.	60
Figure 3.18	The simulated UV-vis spectra [CuL1Cu] ⁴⁺ complex. The solid and dot lines are the UV-vis spectra of their singlet and triplet states, respectively.	61

- Figure 3.19** The simulated UV-vis spectra of (a) $[\text{CuL1Cu/L2}]^{2+}$ and (b) $[\text{L2/CuL1Cu/L2}]^0$ complexes. The solid and dot lines are the UV-vis spectra of their singlet and triplet states, respectively. 61
- Figure 3.20** The simulated UV-vis spectra of (a) $[\text{CuL1Cu/L2/CN}]^+$, (b) $[\text{L2/CuL1Cu/L2/CN}]^-$ and (c) $[\text{CN/L2/CuL1Cu/L2/CN}]^{2-}$ complex species in aqueous solution. The solid and dot lines are the UV-vis spectra of their singlet and triplet states, respectively. 61
- Figure 3.21** The details of titration model (a), and the simulated UV-vis spectrum (solid line) obtained by a mixture of $[\text{CuL1Cu}]^{4+}$, $[\text{CuL1Cu/L2}]^{2+}$ and $[\text{L2/CuL1Cu/L2}]^0$ where (b) K_1 and $K_2 = 1$, (c) $K_1 = 0.02$ and $K_2 = 0.1$. 63
- Figure 3.22** The details of titration model (a), and the simulated UV-vis spectrum (solid line) obtained by a mixture of $[\text{CuL1Cu}]^{4+}$, $[\text{CuL1Cu/L2}]^{2+}$, $[\text{L2/CuL1Cu/L2}]^0$, $[\text{CuL1Cu/L2/CN}]^+$, $[\text{L2/CuL1Cu/L2/CN}]^-$ and $[\text{CN/L2/CuL1Cu/L2/CN}]^{2-}$ where (b) K_1, K_2, K_3, K_4 and $K_5 = 1$, (c) $K_1 = 1 \times 10^{-3} \text{ M}^{-1}$, $K_2 = 1 \times 10^{-1} \text{ M}^{-1}$, $K_3 = 1 \times 10^{-1} \text{ M}^{-1}$, $K_4 = 1 \times 10^1 \text{ M}^{-1}$ and $K_5 = 1 \times 10^2 \text{ M}^{-1}$ 65
- Figure 3.23** The cyanide-bound dominant species in $\text{Cu}_2\text{L1-PGR}$ system depicted from the computational calculation results. 67

Chapter IV

- Figure 4.1** Equilibrium involved in the interaction between the boronic acid group and cyanide [109]. 72
- Figure 4.2** Cyanide addition to compound **XVII** and **XVIII** [110, 111]. 73
- Figure 4.3** The self-assembled chemosensor utilizing the building blocks (a catechol dye and **NPBA**) for the easy-to-prepare colorimetric assay. 74
- Figure 4.4** Chemical structure of **ARS**, and **ARS-PBA**. 74
- Figure 4.5** Dye displacement assay utilizing an **ARS**-bound hydrogel for fructose detection [132]. 75
- Figure 4.6** **ARS-PBA** ensemble for the detection of H_2O_2 in neutral aqueous buffer with added CTAB [129]. 75
- Figure 4.7** Proposed mechanism for detection of CN^- based on **ARS** and boronic acid derivatives in this work. 76
- Figure 4.8** (a) Absorption and (b) emission spectra ($\lambda_{\text{ex}} = 460 \text{ nm}$) of **ARS** ($5.0 \times 10^{-5} \text{ M}$) and **ARS-NPBA** (**ARS**, $5.0 \times 10^{-5} \text{ M}$; **NPBA**, $2.0 \times 10^{-4} \text{ M}$) in 0.01 M PBS buffer at pH 8.0. 77
- Figure 4.9** Chemical structure of phenylboronic acid derivatives employed in this study. 79
- Figure 4.10** (a) The effect of boronic acid types on the fluorescence intensity of **ARS-BAs** in the absence and in the presence of KCN in 0.01 M PBS buffer at pH 8.0. (b) Fluorescence quenching of **ARS-NPBA** by $2.44 \times 10^{-3} \text{ M}$ (**ARS**, $5.0 \times 10^{-5} \text{ M}$; **BAs**, $2.0 \times 10^{-4} \text{ M}$). 79
- Figure 4.11** Fluorescence intensity change at 590 nm as a function of **BAs** concentration in the range of 0 – 0.7 mM ($[\text{ARS}] = 5.0 \times 10^{-5} \text{ M}$). 80

- Figure 4.12** The effect of reaction time on the emission intensity at 590 nm of **ARS–NPBA** ensemble in the absence and in the presence of KCN in 0.01 M PBS buffer at pH 8.0 (**ARS**, 5.0×10^{-5} M; **NPBA**, 2.0×10^{-4} M).81
- Figure 4.13** (a) The effect of **NPBA** concentrations on the fluorescence intensity of **ARS** in the absence and in the presence of KCN in 0.01 M PBS buffer at pH 8.0. (b) Fluorescence quenching of **ARS–NPBA** by 2.44×10^{-3} M CN^- (**ARS**, 5.0×10^{-5} M).82
- Figure 4.14** The effect of pH on the fluorescence intensity of **ARS** in the absence and in the presence of 2.44×10^{-3} M CN^- (**ARS**, 5.0×10^{-5} M; **NPBA**, 2.0×10^{-4} M).83
- Figure 4.15** (a) The effect of PBS concentrations on the fluorescence intensity of **ARS** in the absence and in the presence of KCN at pH 8.0. (b) Fluorescence quenching of **ARS–NPBA** by 2.44×10^{-3} M CN^- (**ARS**, 5.0×10^{-5} M; **NPBA**, 2.0×10^{-4} M).83
- Figure 4.16** Changes in (a) absorption, (b) emission, and (c) color of **ARS–NPBA** (**ARS**, 5.0×10^{-5} M; **NPBA**, 2.0×10^{-4} M μM) upon addition of various anions (50 equiv.) in 0.01 M PBS buffer at pH 8.0.84
- Figure 4.17** ^{11}B NMR spectra of **NPBA** in the absence or presence of **ARS** upon addition of KCN in 0.01 M PBS buffer at pH 8.0.86
- Figure 4.18** Fluorescence spectral changes of **ARS–NPBA** (**ARS**, 5.0×10^{-5} M; **NPBA**, 2.0×10^{-4} M) in the presence of different concentrations of CN^- in 0.01 M PBS buffer at pH 8.0. (a) 0 mM (0 eq.), (b) 0.25 mM (5 eq.), (c) 0.50 mM (10 eq.), (d) 0.74 mM (15 eq.), (e) 0.99 mM (20 eq.), (f) 1.23 mM (25 eq.), (g) 1.48 mM (30 eq.), (h) 1.72 mM (35 eq.), (i) 1.96 mM (40 eq.), (j) 2.20 mM (45 eq.), (k) 2.44 mM (50 eq.).87
- Figure 4.19** Calibration curve for detection cyanide using **ARS–NPBA** ensemble. .87
- Figure 4.20** Competition experiments in the **ARS–NPBA–CN⁻** system with common foreign anions (**ARS**, 5.0×10^{-5} M; **NPBA**, 2.0×10^{-4} M; CN^- , 1.25 mM; X^- , 2.5 mM) in 0.01 M PBS buffer at pH 8.0 ; (1) = **ARS–NPBA**, (2) = **ARS–NPBA** + CN^- , (3) = (2) + F^- , (4) = (2) + Cl^- , (5) = (2) + Br^- , (6) = (2) + I^- , (7) = (2) + AcO^- , (8) = (2) + ClO_4^- , (9) = (2) + SO_4^{2-} , (10) = (2) + NO_3^- and (11) = (2) + SCN^-88
- Figure 4.21** Proposed **ARS–NPBA** formation and interaction with CN^-90
- Figure 4.22** The simulated UV-vis and fluorescence spectra of (a) **ARS–NPBA(OH⁻)**, (b) **ARS–NPBA(CN⁻)**. The UV-vis and fluorescence bands are located at the left (in blue) and right (in red), respectively.92

Appendix

- Figure S1** ^1H NMR (300 MHz, CDCl_3) spectrum of 1,8-dibromoanthraquinone (top) and 1,8-dibromoanthracene (down). 112
- Figure S2** The CPCM/CAM-B3LYP/6-31G(d)-optimized structures of (a) free L1 (anthracene based tripodal tetramine) and (b) $[\text{CuL1Cu}]^{4+}$ complex. Their top and side views are located at top and bottom, respectively. . 113
- Figure S3** The B3LYP/-31G(d,p)-optimized structures of (a) L2^0 , (b) L2^{2-} , (c) L2^{2-} and (d) L2^{3-} species in water. Their top and side views are located at top and bottom, respectively. 114
- Figure S4** The corresponding simulated UV-vis spectra of (a) L2^0 , (b) L2^- , (c) L2^{2-} and (d) L2^{3-} species in water which are scaled by 1.20..... 115
- Figure S5** The CPCM/CAM-B3LYP/6-31G(d)-optimized structure of **L2 (PGR)**, as L2^{2-} -species. 115
- Figure S6** MS data of **ARS-NPBA** before (a) and after (b) reacting with CN^- 116
- Figure S7** The CPCM/UFF/B3LYP/6-311+G(d,p)-optimized structures of (a) **ARS**, (b) **NPBA**, (c) **NPBA(CN) $_2$** , (d) **NPBA(CN) $_3^-$** , (e) **ARS-NPBA(OH $^-$)/H $_3$ O $^+$** , (f) **ARS-NPBA(OH $^-$)**, (g) **ARS-NPBA(CN $^-$)** and (h) **ARS/NPBA(CN) $_2$** 117
- Figure S8** The optimized excited-state structures of (a) **ARS-NPBA(OH $^-$)**, (b) **ARS-NPBA(CN $^-$)**. **Error! Bookmark not defined.**

LIST OF TABLES

Chapter II

Table 2.1	Crystal Data and Structure Refinement Details for 1	23
Table 2.2	Crystal data, data collection, and structure refinement for 2	24
Table 2.3	Computed UV-vis of 1 and 2 compared with experimental values.	27

Chapter III

Table 3.1	Comparison of some metal ensemble based chemosensors for cyanide detection.	55
Table 3.2	The determination of cyanide ions in real water samples using Cu₂L1-PGR ensemble.	56
Table 3.3	The reaction energies (ΔE_{react} in kcal/mol) of complex formation occurring within two sets of UV-vis titrations.	66

Chapter IV

Table 4.1	Binding constant of ARS with phenylboronic acid derivatives.	80
Table 4.2	The determination of cyanide ions in real water samples using ARS-NPBA sensor.	89
Table 4.3	Computed UV-vis of ARS , its dominant complexes and fluorescence spectra of ARS-NPBA(OH⁻) and ARS-NPBA(CN⁻) in water, compared with experimental values.	90

Appendix

Table S1	The reaction energies and thermodynamic quantities of ARS-NPBA formation and interaction with CN⁻ ion.	118
-----------------	--	-----

LIST OF ABBREVIATIONS

APCI	Atmospheric pressure chemical ionization
ARS	Alizarin Red S
br	Broad
°C	Degree Celsius
CD ₂ Cl ₂	Deuterated dichloromethane
CDCl ₃	Deuterated chloroform
cm ³	Cubic centimeter
cm ⁻¹	Wavenumbers
CTAB	Cetyl trimethylammonium bromide
δ	Chemical shift in parts per million
d	Doublet
dd	Doublet of doublets
DFT	Density functional theory
dm ³	Cubic decimeter
DMSO	Dimethyl sulfoxide
DPA	Dipicolylamine
ε	Molar absorptivity
equiv.	Equivalent
ESI ⁺	Positive phase electrospray ionization
ESI ⁻	Negative phase electrospray ionization
EtOH	Ethanol
E _{1/2}	Half wave potential
Fc/Fc ⁺	Ferrocene / ferrocenium couple
g	Gram
h	Hour(s)
HEPES	4-(2-hydroxyethyl)-1-piperazineethanesulfonic acid
HRMS	High resolution mass spectrometry
H ₂ O ₂	Hydrogen peroxide
HOMO	Highest occupied molecular orbital
IDA	Indicator displacement assay
I _f /I ₀	Relative fluorescence intensity
<i>J</i>	Coupling constant
<i>K</i> _A	Binding affinity
λ	Wavelength
L	Liter
LUMO	Lowest unoccupied molecular orbital
M	Molar (moles per cubic decimeter)
MeOH	Methanol
Mes	Mesityl group
μM	Micromolar
μL	Microliter
min	Minutes

mg	Milligram
MgSO ₄	Magnesium sulfate
MHz	Megahertz
mM	Millimolar
mmol	Millimole
mol	Mole
<i>m/z</i>	Mass-to-charge ratio
nm	Nanometer
NH ₄ Cl	Ammonium chloride
NMR	Nuclear magnetic resonance
ONOO ⁻	Peroxynitrite
PBA	Phenylboronic acid
PGR	Pyrogallol red
<i>pK_a</i>	-log <i>K_a</i>
ppm	Parts per million
ROS	Reactive oxygen species
RNS	Reactive nitrogen species
rt	Room temperature
s	Singlet / second
S ₀	Singlet electronic ground state
S ₁	First singlet electronic excited state
TBACN	Tetrabutylammonium cyanide
TBAF	Tetrabutylammonium fluoride
TBAPF ₆	Tetrabutylammonium hexafluorophosphate
TD-DFT	Time-dependent density functional theory
THF	Tetrahydrofuran
TMEDA	Tetramethylethylenediamine
UV-vis	Ultra-violet
V	Volt

CHAPTER I

INTRODUCTION

1.1 Significance of anions

Currently, the recognition and detection of anions is an area that has received considerable attention due to the importance of these species in biological, environmental, and chemical processes. Physiologically relevant anions that are widely present in living organism as well as environmental systems can be either essential to sustain growth or act as severe environmental pollutants and demonstrate adverse health effects.

Among the commonly existing anions, fluoride (F^-) ion is attracting a great deal of interest for anion sensing because of the significance of this anion in the area of health and environmental issues. Drinking water and toothpaste are often supplemented with fluoride to maintain dental care [1]. Additionally, fluoride has a potential use in pharmaceutical agents for the treatment of osteoporosis, a disease which reduces bone density and increase the risk of fractures [2]. It also plays a crucial role in military applications such as the refinement of uranium used in nuclear weapons manufacture [3]. However, fluoride may have a beneficial or harmful effect on human health depending on its concentration. Excessive consumption of fluoride has been associated with many diseases including acute gastric, kidney failure, and dental or even skeletal fluorosis because fluoride is easily absorbed by the body, but is excreted slowly [4, 5]. Because of these side effects, the maximum contaminant level for fluoride in drinking water has been set to 4 ppm by the Environmental Protection Agency (EPA) [6].

On the other hand, cyanide (CN^-) ion is known as one of the most toxic species and is extremely harmful to human body. The toxicity results from its binding to the active site of cytochrome c oxidase, interfering the mitochondrial electron-transport chain and inhibiting cellular respiration causing cytotoxic hypoxia [7, 8]. Cyanide could be absorbed through inhalation, ingestion and skin contact, and even as little as 0.5–3.5 mg of cyanide per kilogram of body weight is lethal to humans [9].

Thus, the permissible limit for cyanide in drinking water has been set to 1.9 mM by the World Health Organization (WHO) [10]. Nevertheless, the use of cyanide cannot be avoided because of its widespread applications in various fields of industry including electroplating, metallurgy, gold mining, and plastic production, which raises the risk for accidental and intentional release of cyanide as environmental contaminant [11-13].

Therefore, for detailed studies of the toxicological effects and beneficial parts of the fluoride and cyanide anions, discovering methods for the recognition of these anions has become a topical research objective.

1.2 Chemosensor

Molecular recognition and sensor have a strong relationship that involves the selective interaction between a host and a guest. When molecular recognition becomes molecular sensing, it often results in a chemosensor (chemical sensor).

Chemosensors are defined as chemical systems that transform stimuli into some forms of response, such as a fluorescent or color change or an electronic signal [14]. The difference between a receptor and a sensor is the communication event. The sensor must include a mechanism that can report the binding event to the signal. Generally, design of chemosensors consists of two parts as depicted in Figure 1.1. One is a binding unit, and the other is a signaling unit (chromophore or fluorophore) which turns binding-induced changes into detectable signals. The signal unit and binding site are connected through the covalent bond. When the analyte interacts with the binding site, the color or emission changes will be observed based on different mechanisms (electron transfer, proton transfer, and energy transfer).

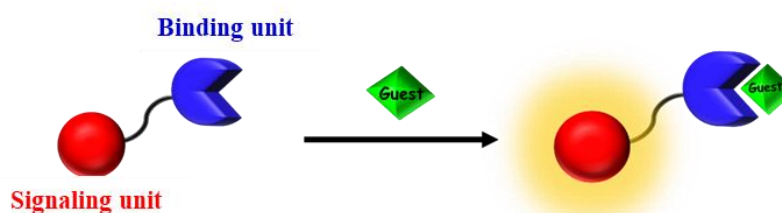


Figure 1.1 Schematic diagram showing binding of a guest by a chemosensor.

1.3 Chemosensing ensemble

In the last two decades, there is the use of chemosensing ensemble as an alternative sensing approach. This approach, pioneered by Eric Anslyn [15], relies on the binding between an indicator and a receptor via noncovalent interactions such as hydrogen bonding, electrostatic, donor-acceptor, π - π stacking, van der Waals force, and hydrophilic and hydrophobic interactions. The interaction between the ensemble and target analytes changes the molecular conformation and charge density leading to the change in optical properties of the indicator. Utilizing chemosensing ensemble approach is advantageous because unlike the traditional sensing methods, the system does not require the covalent connection between the indicator and receptor. Moreover, the different detection wavelengths can be used by selecting an appropriate indicator. Several indicators with one receptor can be employed as a sensing array for efficient analysis in practical applications. Another factor to consider is that the resulting ensemble can be obtained *in situ* and used in aqueous solutions. These make the ensemble assay easy to apply with different receptors and indicators for real-time analysis of complicated samples [16].

There is no systematic classification for chemosensing ensemble approach. However, the ensemble system can be categorized into two concepts including displacement and complexation, depending on whether or not the indicator is released from the ensemble as shown in Figure 1.2. This changes the environment around the indicator resulting in perturbations to its optical properties following the analytes to be detected.

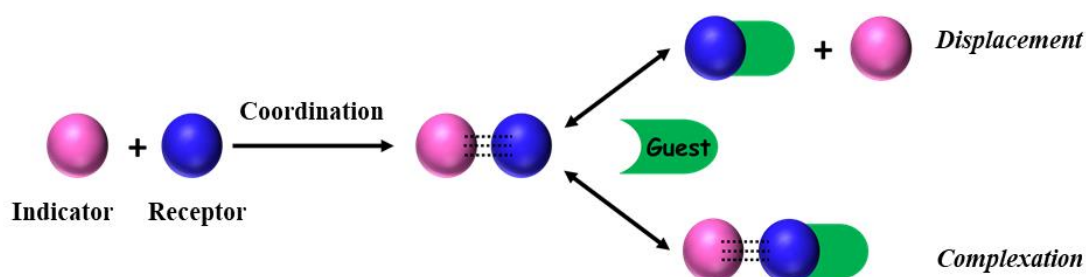


Figure 1.2 Schematic diagram of two ensemble concepts (displacement and complexation).

In an indicator displacement assay (IDA), the receptor binds reversibly to a colorimetric or fluorescent indicator in solution. There are two main requirements for this assay: the interaction between the receptor and the indicator must not be too strong and the indicator must display a significant change in optical properties when bound to the receptor and when dispersed in solution [17]. Then, the indicator is displaced from the host cavity and released to the solution upon the addition of competitive analyte, which in turn modulates an optical feature.

1.4 Anion recognition

The recognition of anions is particularly challenging compared to cations. This may be attributed to two reasons. Firstly, anions have lower charge to radius ratio (smaller, softer, more diffuse). The more diffuse nature means the less effective electrostatic binding interaction in comparison with cations. Secondly, anions have a wide variety in geometries and thus a high degree of design is required to make receptors that are selective for a particular anion [18]. For the design of anion receptors, the important factors to consider are how to achieve the specific recognition of a certain anion and how to convert the recognition event into a signal. Among synthetic anion receptors developed to date, receptors containing metal ions or Lewis acids, such as neutral boranes and boronic acids, have received increasing attention. They show strong affinity toward nucleophilic anions, such as fluoride and cyanide ions, through Lewis acid–base interaction.

1.4.1 Anion recognition by bifunctional boron Lewis acid

Lewis acidic receptors based on main group elements such as boron have been proven to the recognition of small nucleophilic anions. Among them, boron-containing π -electron systems is of intense current interest to chemist. In such derivatives, three π -conjugated groups on a boron atom have a unique lowest unoccupied molecular orbital (LUMO) in which the π -conjugation is extended through the vacant p-orbital of the boron atom (Figure 1.3). The anion complexation of these boranes leads to a perturbation of the frontier orbitals thereby altering the photophysical properties of the receptor [19]. For instance, the formation of a stable

fluoroborate complex of tris(9-anthryl)borane in tetrahydrofuran (THF) leads to a color change of the system (Figure 1.4) as a result of the interruption of the π -conjugation [20]. Additionally, the steric and electronic properties of the aryl substituents incorporated into the boron center are also suggested to influence the anion affinity of triarylboranes.

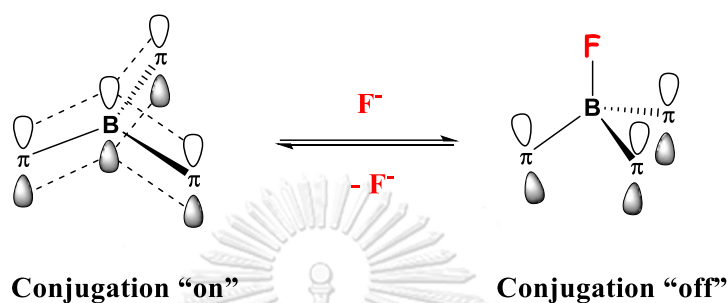


Figure 1.3 Schematic representation of the switching of π -conjugation in the LUMO of boron-based π -electron systems.



Figure 1.4 Colorimetric change of tris(9-anthryl)borane upon addition of F^- in THF.

In addition to monofunctional boranes, important advances have also been realized with bifunctional boranes to increase the anion affinity via chelation. In this domain, two boron Lewis acidic sites are interconnected by an organic skeleton such as 1,8-naphthalenediyl [21] and ortho-phenylene [22] as shown in Figure 1.5. The high anion affinity of these diboranes results from cooperative effects involving the neighboring Lewis acidic centers which interact with the anion to form a chelate complex.

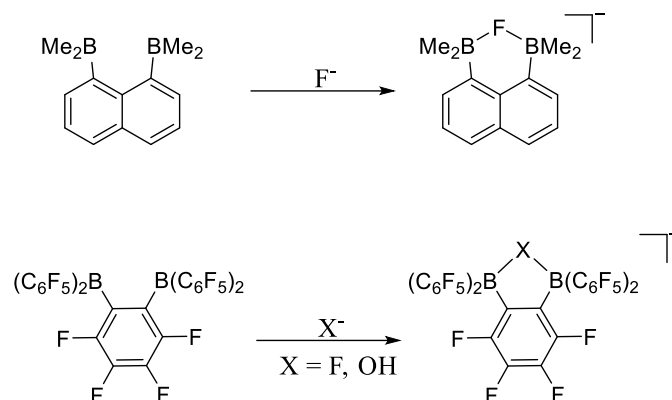


Figure 1.5 Reaction of bifunctional boranes based 1,8-naphthalenediyl, and ortho-phenylene backbone with small nucleophilic anions.

Bearing in mind that the size of the binding pocket that matches between the host and the guest impacts the selectivity of these diboranes, the scope of backbones supporting bifunctional Lewis acids is not limited to ortho-phenylene and naphthalene. Other platforms with different separation of the two boron centers have also been developed.

1.4.2 Anion recognition by metal complexes

Metal complexes with vacant coordination sites have been widely used as receptors for anion recognition. They serve as recognition sites to bind anions through metal–ligand interactions and can exhibit some geometrical preferences, thus imparting selective binding tendencies towards anions of a given shape [23]. Such complexes have been shown to bind a wide variety of anions including halides [24], phosphates [25], dicarboxylates [26], and oxalates [27]. Furthermore, metal complexes in conjunction with indicator displacement assay (M-IDA) highly interest researchers because the sensing assays can be easily carried out in aqueous media. The M-IDA strategy is based on the displacement of the indicator attached onto the metal complex by a noncovalent model of the analytes. Examples of metal complexes and common complexometric indicators in M-IDA are illustrated in Figure 1.6 and Figure 1.7, respectively. To achieve the desired sensitivity and selectivity of this system, the interaction between metal complexes, indicators and the target analytes must be carefully tuned.

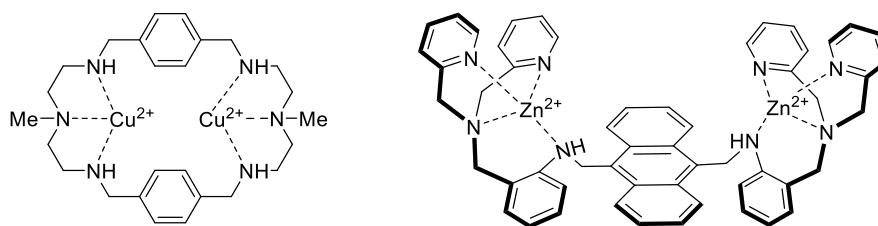


Figure 1.6 Examples of dinuclear copper [28] and zinc [29] complexes in M-IDA.

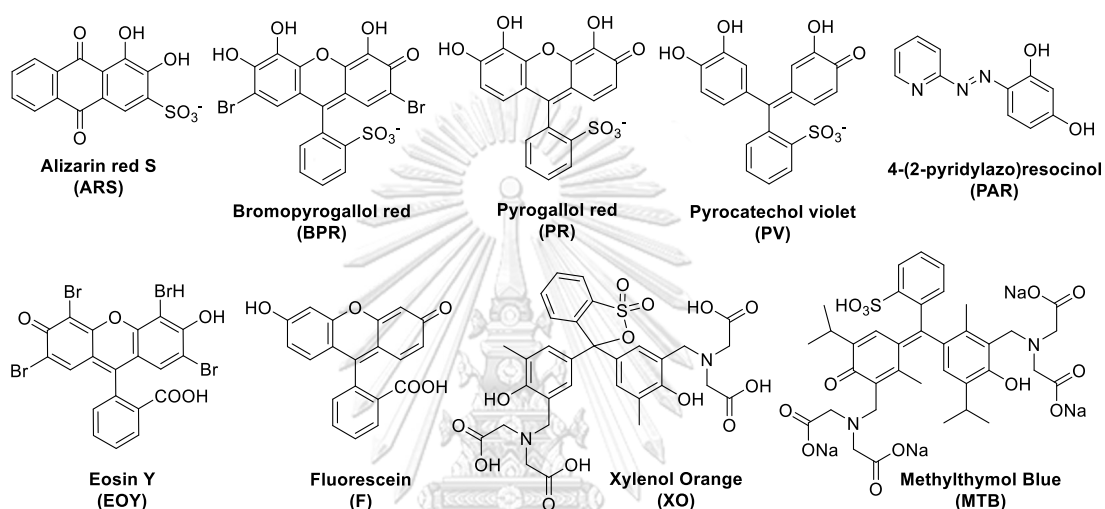


Figure 1.7 Various complexometric indicators commonly used in IDA.

1.4.3 Anion recognition by boronic acid

Boronic acid receptors have become popular chemosensors for the detection of various analytes. For instance, boronic acids are able to form boronate esters with saccharides including 1,2- and 1,3-diol-containing structures through reversible covalent linkages. In addition, they are oxidized by reactive oxygen and reactive nitrogen species (ROS/RNS i.e. H_2O_2 , ONOO^-) generated in biological and cellular systems to give hydroxy compounds as shown in Figure 1.8. More interestingly, boron in trisubstituted boron compounds serves as Lewis acid metal center having an sp^2 trigonal planar geometry with an empty p orbital perpendicular to the plane of the molecule. Based on the Lewis acid–base interaction between boron and anions, the electron-poor boron sites are able to interact with anionic bases, such as fluoride and cyanide ions, results in a change in hybridization to an sp^3 tetrahedral geometry (Figure 1.9) [30].

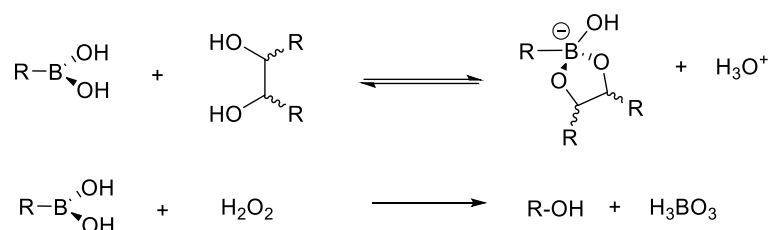


Figure 1.8 The reversible formation of a cyclic boronate ester and oxidative removal of the boronic acid.

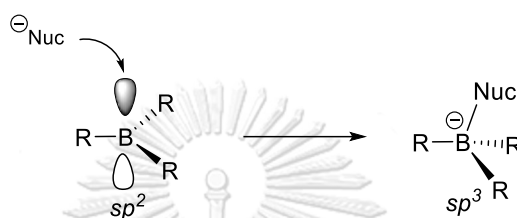


Figure 1.9 Diagram illustrating the change in geometry at the boron center on interaction with nucleophiles.

There is another powerful and simple way towards boronic acid-based sensors, obtained by linking receptor and reporter through reversible interactions. This system refers to the indicator displacement assay (IDA) in which the receptor is boronic acids and the reporter is catechol indicators. The receptor–reporter ensemble is then selectively separated in a competitive assay upon the addition of appropriate analytes. The change of the output signal can be used to detect the target analytes (Figure 1.10) [31].

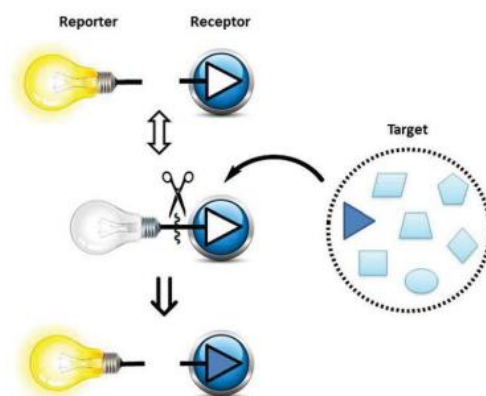


Figure 1.10 Schematic illustration of the receptor-reporter ensemble system [31].

1.5 Project objectives

Project I – Anion binding properties of 1-(dimesitylboryl)anthracene and 1,8-bis(dimesitylboryl)anthracene

In the chemistry of bifunctional boron Lewis acids, the backbones used to support the Lewis acidic units play an important role in determining the anion binding properties of the receptors. We have become interested in backbones which afford an increased separation between the two boron centers compared to common backbones, such as naphthalene and ortho-phenylene. Among various backbones, anthracene came to our attention because of its good photophysical properties and large separation between the substituents on its C1 and C8 carbons of the anthracene backbone. This may facilitate the selective complexation of diatomic molecules such as cyanide ions. Therefore, the work presented herein is focused on the synthesis and photophysical characterization of (1) mono- and (2) bifunctional boron Lewis acids with anthracene backbones (Figure 1.11). We have also investigated how the nature of the anthracene affects the fluoride and cyanide binding properties of these new derivatives.

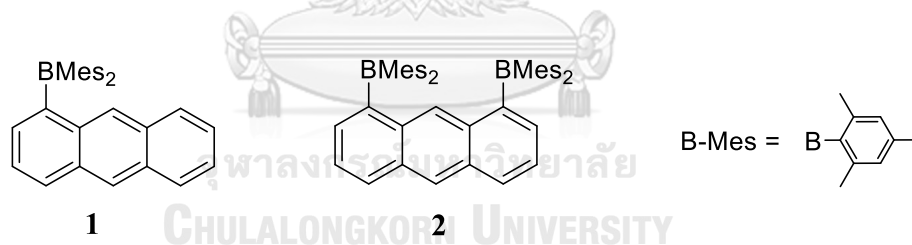


Figure 1.11 Chemical structures of 1 and 2.

Project II – Detection of cyanide ions using dinuclear copper(II) complex of anthracene based tripodal tetramine under indicator displacement assay

It has been reported that dinuclear copper(II) complex-based IDA are able to detect cyanide ions in water [28] and previous work of our group has demonstrated that dinuclear zinc(II) complex of anthracene based tripodal tetramine (Zn_2L1) can be used to discriminate pyrophosphate from other phosphate containing anions under the IDA approach [29]. Thus, we have chosen the dinuclear copper(II) complex of anthracene based tripodal tetramine (Cu_2L1 , Figure 1.12) as receptors in this work. We expected that, in view of the suitable cavity and the coordinative unsaturation of the two copper centers, the Cu_2L1 could be a reasonably good candidate for behaving as a colorimetric cyanide sensing. The overall objective has been to test this possibility by investigating the synthesis and properties of the Cu_2L1 . We have also chosen an appropriate colorimetric indicator to be coupled to the Cu_2L1 . Based on IDA approach, the colorimetric detection of cyanide using the ensemble between Cu_2L1 and indicator has been demonstrated.

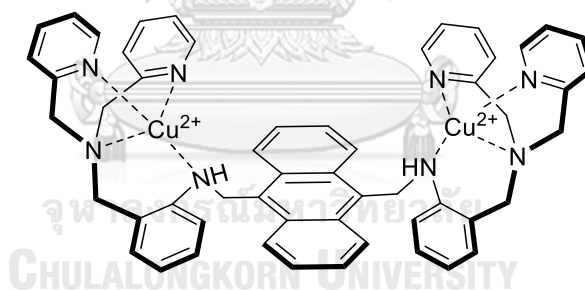


Figure 1.12 Chemical structures of Cu_2L1 .

Project III – Alizarin Red S conjugated boronic acid ensembles for the selective detection of cyanide under indicator displacement assay

The objective of this project has been to develop the cyanide sensing systems that are simple, rapid, selective and cost-effective. We decided to evaluate the sensing systems, which was formed by mixing common phenyl boronic acid derivatives and catechol indicators like Alizarin Red S (**ARS**). By taking advantage of cyanide–boron interaction based on IDA approach, we expected that **ARS** molecules are displaced by the formation of tricyano borate (Figure 1.13). We have also studied the effect of substituents of phenyl boronic acids on the stability of the ensembles. Furthermore, the optimization of the appropriate conditions for use in this sensing ensemble has been investigated.

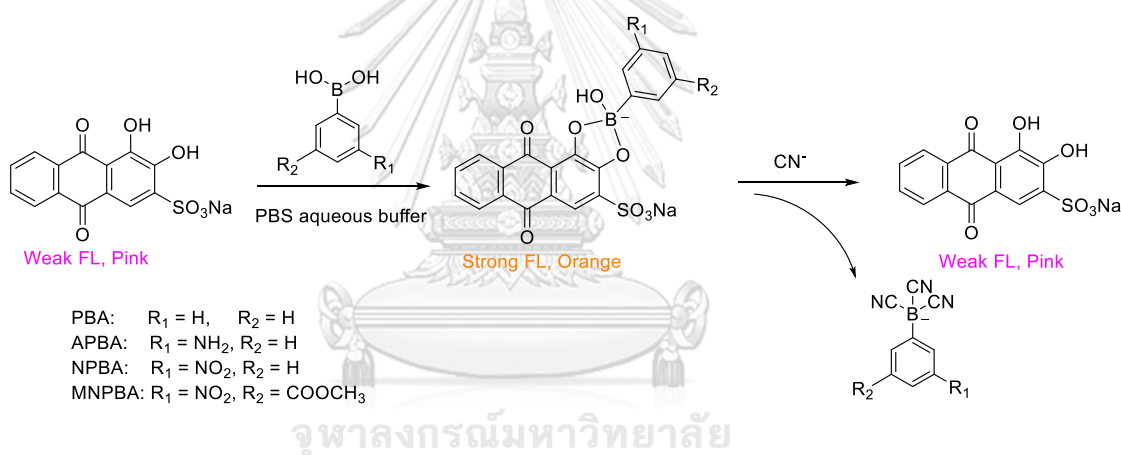


Figure 1.13 Proposed mechanism for detection of CN^- based on **ARS** and boronic acid derivatives.

CHAPTER II

ANION BINDING PROPERTIES OF 1-(DIMESITYLBORYL) ANTHRACENE AND 1,8-BIS(DIMESITYLBORYL)ANTHRACENE

2.1 Introduction

The chemistry of main group-based Lewis acidic compounds has gained substantial research attention over the past few decades owing to a wide variety of applications in anion transport [32, 33], small molecule activation [34-38], catalysis [39-42] as well as anion sensing [19, 21, 43-47]. A prototypical example of such main group-based Lewis acids is the extensively studied organoboranes in which the vacant p orbital of the electron-deficient boron atom can accept an electron pair from nucleophiles. This intrinsic Lewis acidity has made organoboranes a powerful anion receptor for nucleophilic anions such as fluoride ions.

Common triarylborane has been shown to bind fluoride to form the corresponding fluoroborate adducts. This reaction is driven by the donation of electron pairs of the anions into the unoccupied p_z orbital of the boron center inducing a change in geometry from trigonal planar to tetrahedral (Figure 2.1). Furthermore, the anion affinity of the triarylborane is governed by the steric and electronic properties of the aryl substituents incorporated in the boron center.

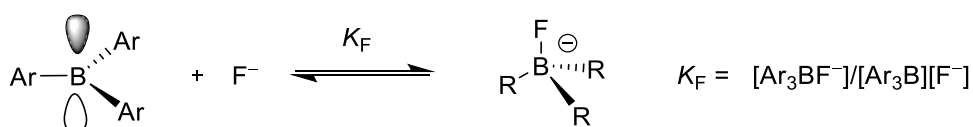


Figure 2.1 Fluoride binding of triarylboranes.

Several groups have studied the complexation of fluoride by monofunctional triarylboranes such as phenyldimesitylborane (**I**), trimesitylborane (**II**), and tris(9-anthryl)borane (**III**) (Figure 2.2) [19, 20, 48]. The binding constant has been estimated as 5×10^6 for **I**, $3.3 \times 10^6 \text{ M}^{-1}$ for **II**, and $2.8 \times 10^5 \text{ M}^{-1}$ for **III** in THF solutions. The lower binding constants of **II** and **III** can be assigned to the steric protection provided by the three mesityl and anthryl substituents to the boron center of these derivatives. Furthermore, these boranes show a high selectivity for fluoride anions as a result of the steric protection of the boron atom provided by at least two mesityl or anthryl groups that prevents coordination of larger anions.

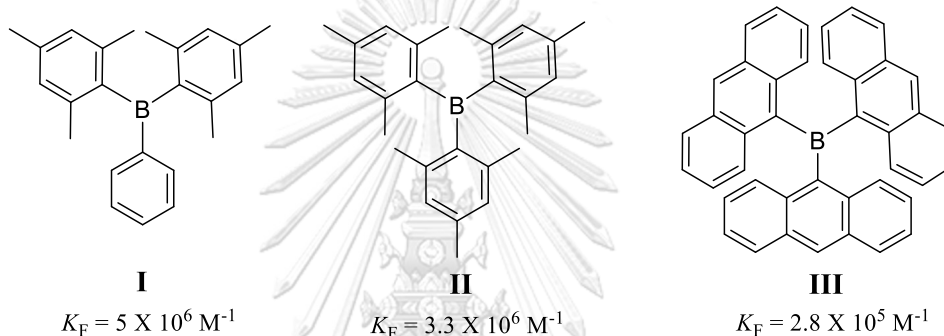


Figure 2.2 Examples of some common monofunctional boranes **I**, **II** and **III**.

One of the successful strategies to increase the anion affinity of triarylboranes is utilizing bifunctional diboranes. The additional receptor sites of the diborane can promote the chelation of guest anions. As a result, the bidentate systems display higher anion affinity than the monofunctional boranes. Examples of such systems include diboranes in which the two boron centers are connected by 1,8-naphthalenediyl such as **IV**, **V**, **VI** and **VII** (Figure 2.3) [19, 45, 49, 50]. Structural analysis of these compounds indicates that the boron centers are separated by only 3.2-3.4 Å. Owing to the short spacing of the two boron centers, these diboranes are well suited for the chelation of monoatomic fluoride anions.

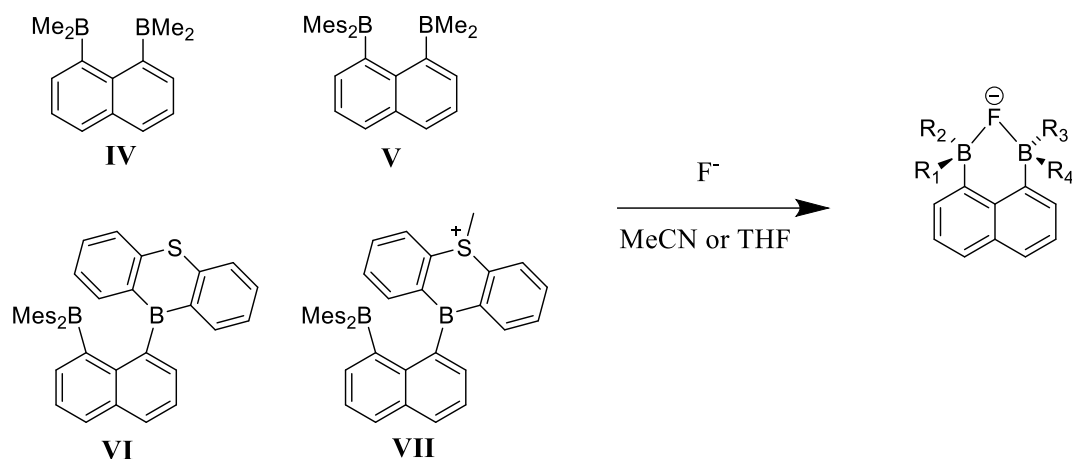


Figure 2.3 Diboranes **IV**, **V**, **VI** and **VII** bind the fluoride anions to afford the corresponding chelating complexes.

Realizing that the separation between the two boron centers influences the chelating properties of these systems, the synthesis of diboranes featuring a larger separation has attracted renewed interest in the past few years. Gabbaï group has extensively studied bidentate diboranes with other backbones such as 1,8-biphenylenediyl (**VIII**) and 1,8-triptycenediyl (**IX**) (Figure 2.4) [51]. The separation between the two boron centers of these systems is more than 4.5 Å. It occurs that the increased separation allows for the selective complexation of diatomic molecules such as cyanide ions in a μ -1,2 fashion.

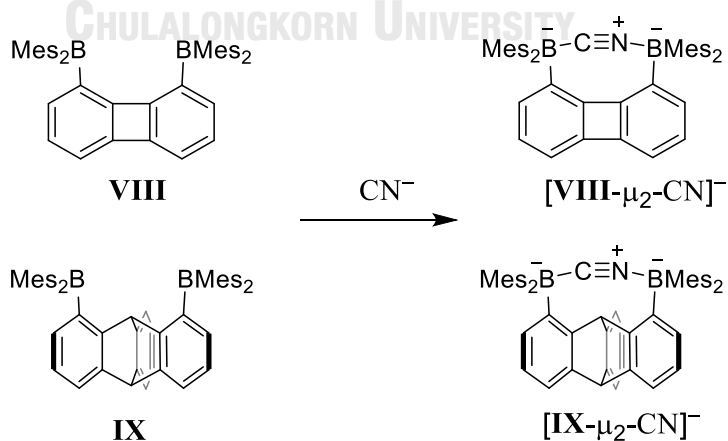


Figure 2.4 Diboranes **VIII** and **IX** bind the cyanide anions to afford the corresponding chelating complexes [51].

Anthracene is known to be a highly efficient fluorescent emitter in solution. Owing to its large electron rich conjugated π system, decoration of anthracene with diboryl groups may lead to interesting properties. These considerations have led us to consider the use of the anthracene backbone which has received a great deal of attention from several groups. In past decades, Katz investigated the synthesis of 1,8-anthracenediethynyl-bis(catechol boronate) (**X** in Figure 2.5) as a bidentate Lewis acid for the chelation of pyrimidines [52]. The Mitzel group recently described an analog of Katz's compound (**XI** in Figure 2.5) in which the two boronate units are replaced by diphenylboryl moieties. This simple permutation affords more Lewis acidic boron moieties as demonstrated by the formation of isolable complexes with tetramethylethylene diamine and pyrimidine [53].

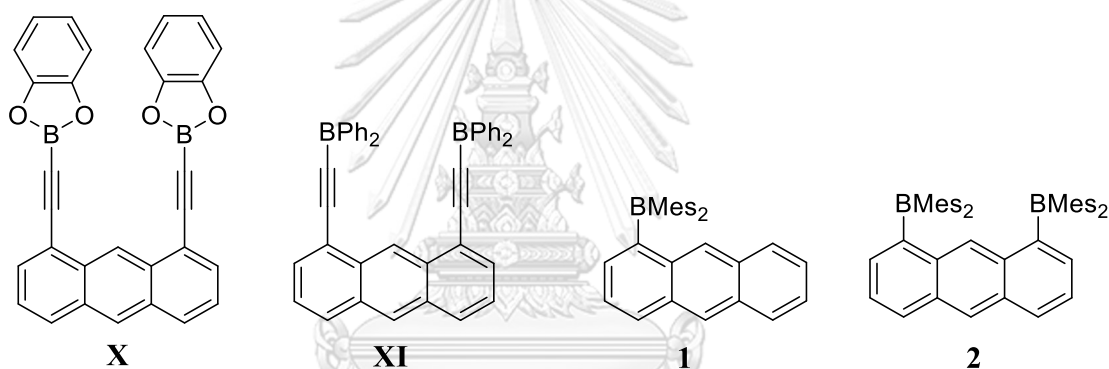


Figure 2.5 Examples of anthracene based diboranes (**X** and **XI**) and target compounds in this work (**1** and **2**).

It occurred to us that the related diborane based on the 1,8-anthracenediyl scaffold bearing mesityl substituents had not been considered [54, 55]. In this work, we fill this knowledge gap by describing the synthesis and properties of the mono- and bifunctional boranes 1-(dimesitylboryl)anthracene (**1** in Figure 2.5) and 1,8-bis(dimesitylboryl)anthracene (**2** in Figure 2.5). Effects of fluoride and cyanide complexation on the electronic and photophysical properties of these boranes have also been investigated.

2.2 Results and discussion

2.2.1 Synthesis and characterization of 1-(dimesitylboryl)anthracene (**1**) and 1,8-bis(dimesitylboryl)anthracene (**2**)

The synthesis of mono- and bis-functionalized anthracene derivatives **1** and **2** was carried out by an adaption of previously published methods [56]. To access both compounds, 1,8-dibromoanthracene was first synthesized by two-step synthesis using 1,8-dichloroanthraquinone as starting materials (Figure 2.6). ^1H NMR spectra of 1,8-dibromoanthraquinone and 1,8-dibromoanthracene are illustrated in Appendix 1. Functionalization of one or both sites of 1,8-dibromoanthracene was further achieved by lithiation followed by quenching with dimesitylboron fluoride (Mes_2B). Both compounds were isolated as air-stable yellow solid in moderate yields and characterized by standard analytical methods including multinuclear NMR spectroscopy (^1H NMR, ^{13}C NMR and ^{11}B NMR), mass spectrometry, and X-ray diffraction analysis.

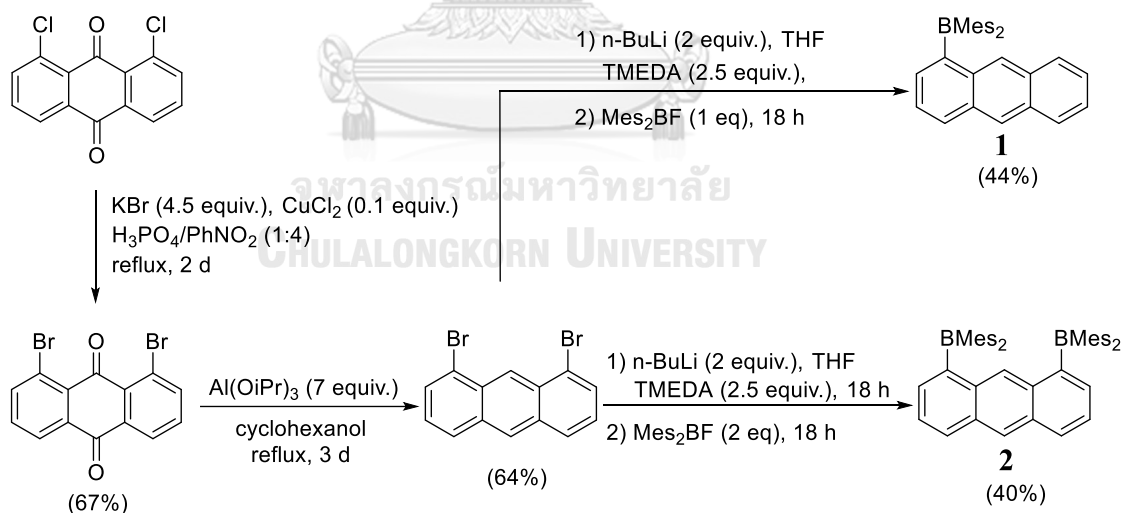


Figure 2.6 Synthetic overview of the mono- and bis-functionalized anthracene derivatives **1** and **2**.

Compound **1** showed ^1H NMR resonances (Figure 2.7) at $\delta = 2.00$ (12H) and 2.31 (6H) ppm for the methyl groups of the mesityl moiety, and 6.80 (4H) ppm for the aryl mesityl protons. Similar shifts are observed for **2** ($\delta = 1.83$ (24H), 2.27 (12H) and 6.70 (8H) ppm in Figure 2.11). However, the ortho-Me and meta-H groups show extensive line broadening, as a result of restricted rotation about the juxtaposed boranes. ^{13}C NMR spectra as shown in Figure 2.8 and Figure 2.12 also support the structure of **1** and **2**, where related resonances are present in their expected position. Additionally, ^{11}B NMR resonances of both compounds were observed as a broad singlet peak at $\delta \approx 75$ ppm as usually observed for such triarylboranes (Figure 2.9 and Figure 2.13) [51, 57-59].

Mass spectrometric analysis also revealed the dominance of the molecular ion peak, $m/z = 447.2586$ (calc. = 427.2592) for $[\mathbf{1}+\text{H}]^+$ and $m/z = 675.4333$ (calc. = 675.4328) for $[\mathbf{2}+\text{H}]^+$, indicating the successful conversion into the target compounds **1** and **2** (Figure 2.10 and Figure 2.14).

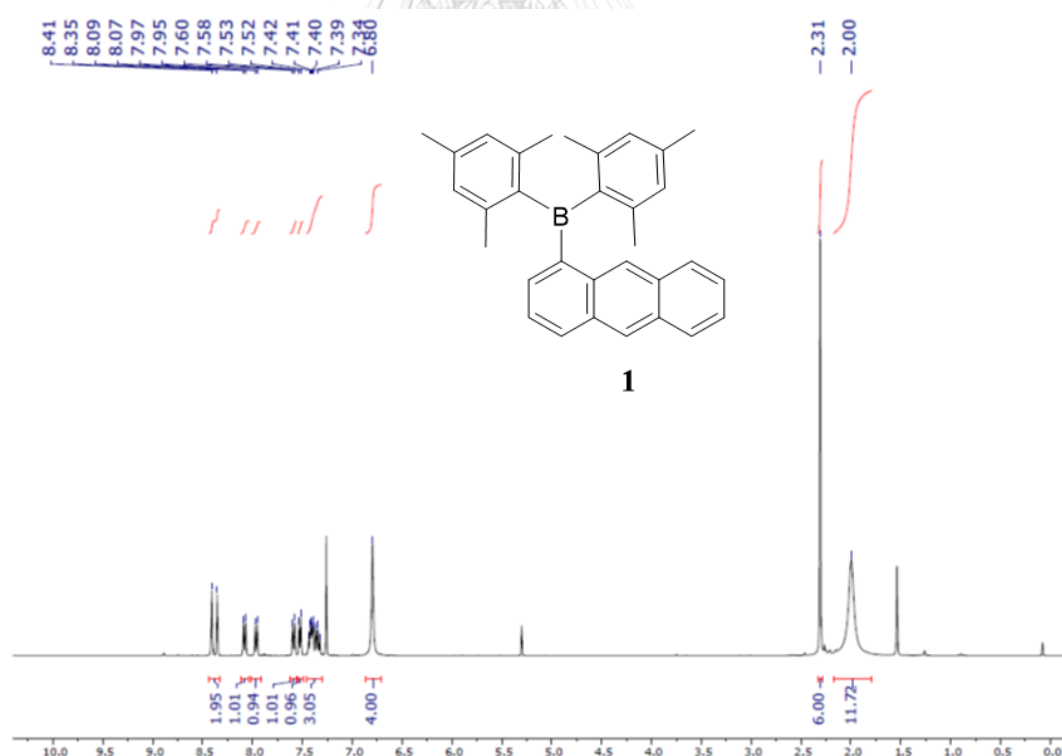


Figure 2.7 ^1H NMR (400 MHz, CDCl_3 , 298 K) spectrum of **1**.

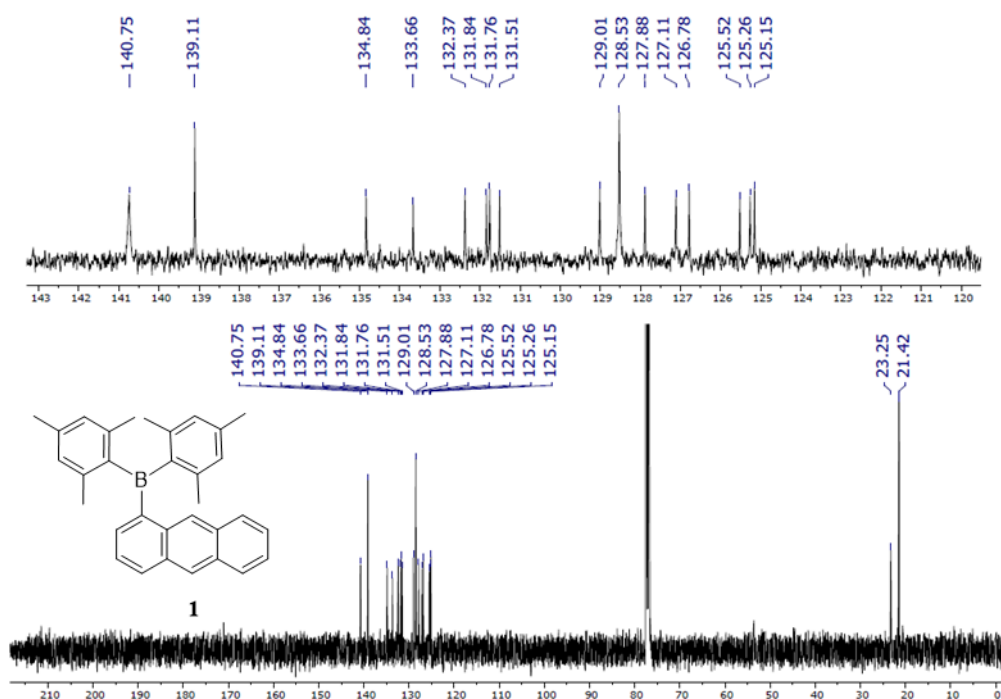


Figure 2.8 ^{13}C NMR (101 MHz, CDCl_3 , 298 K) spectrum of **1**.

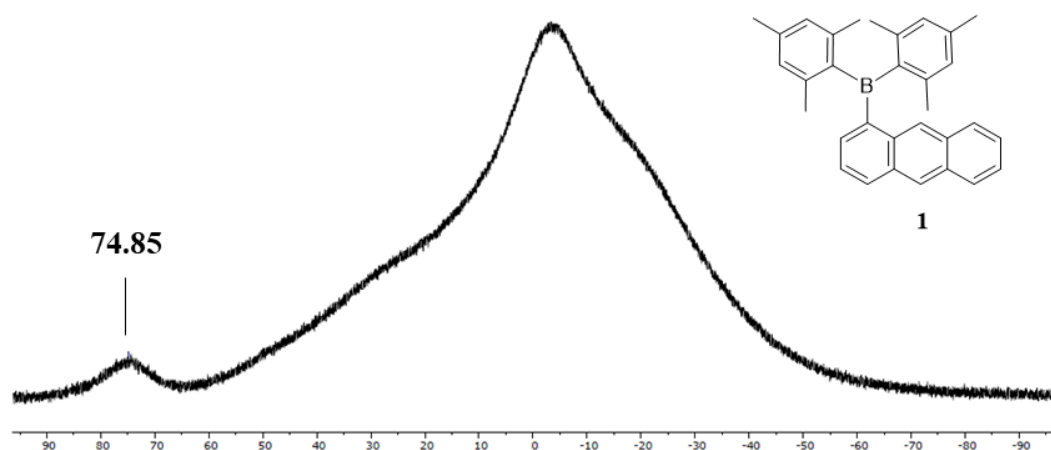


Figure 2.9 ^{11}B NMR (128 MHz, CDCl_3 , 298 K) spectrum of **1**.

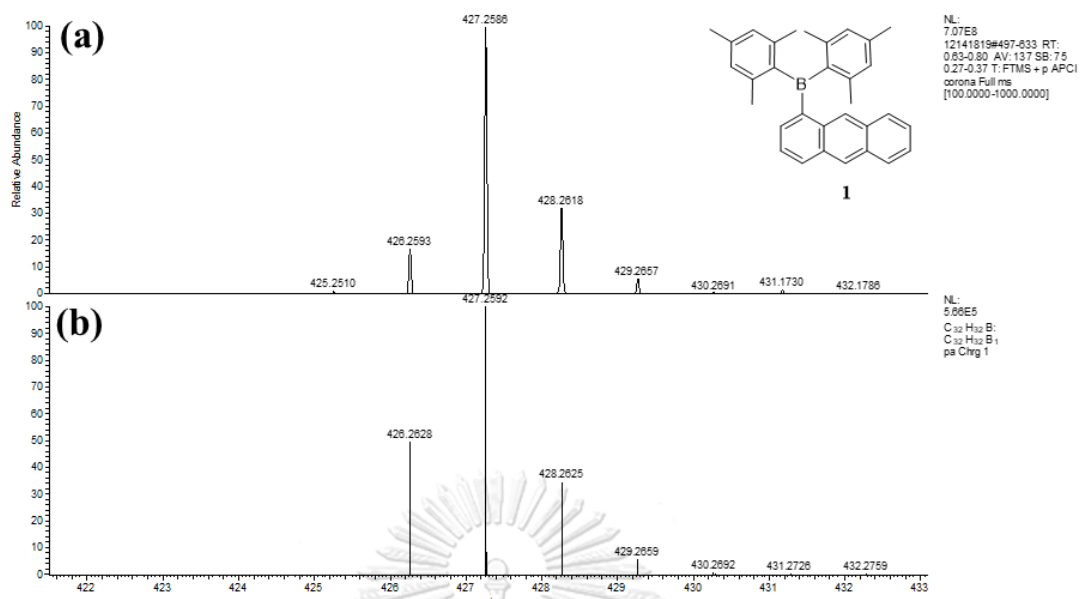


Figure 2.10 HRMS (APCI⁺) of [1+H]⁺ observed (a) and calculated (b).

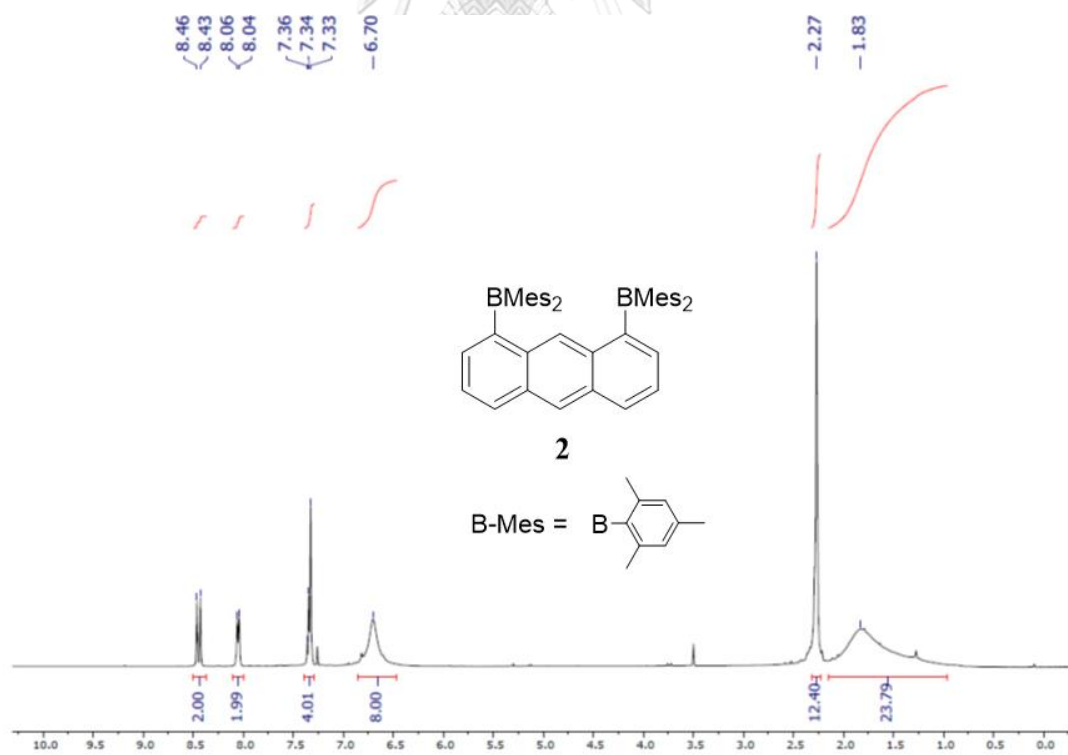


Figure 2.11 ¹H NMR (400 MHz, CDCl₃, 298 K) spectrum of **2**.

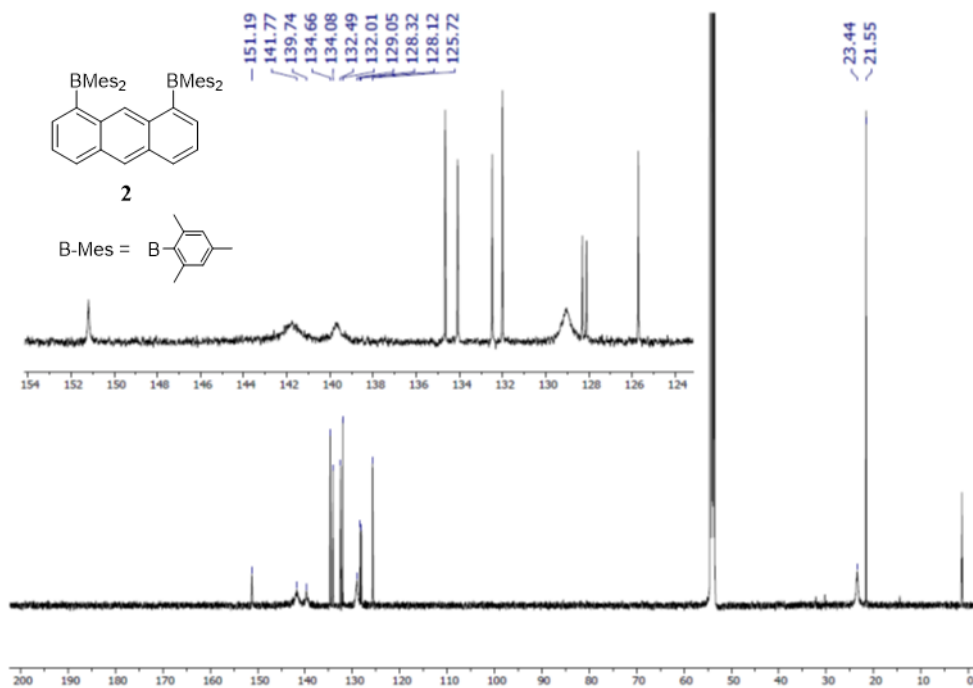


Figure 2.12 ^{13}C NMR (101 MHz, CDCl_3 , 298 K) spectrum of **2**.

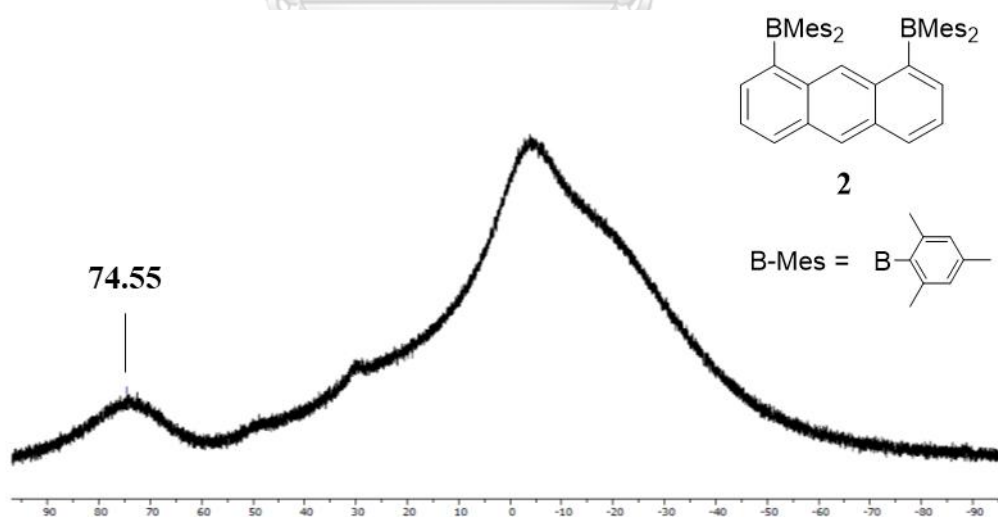


Figure 2.13 ^{11}B NMR (128 MHz, CDCl_3 , 298 K) spectrum of **2**.

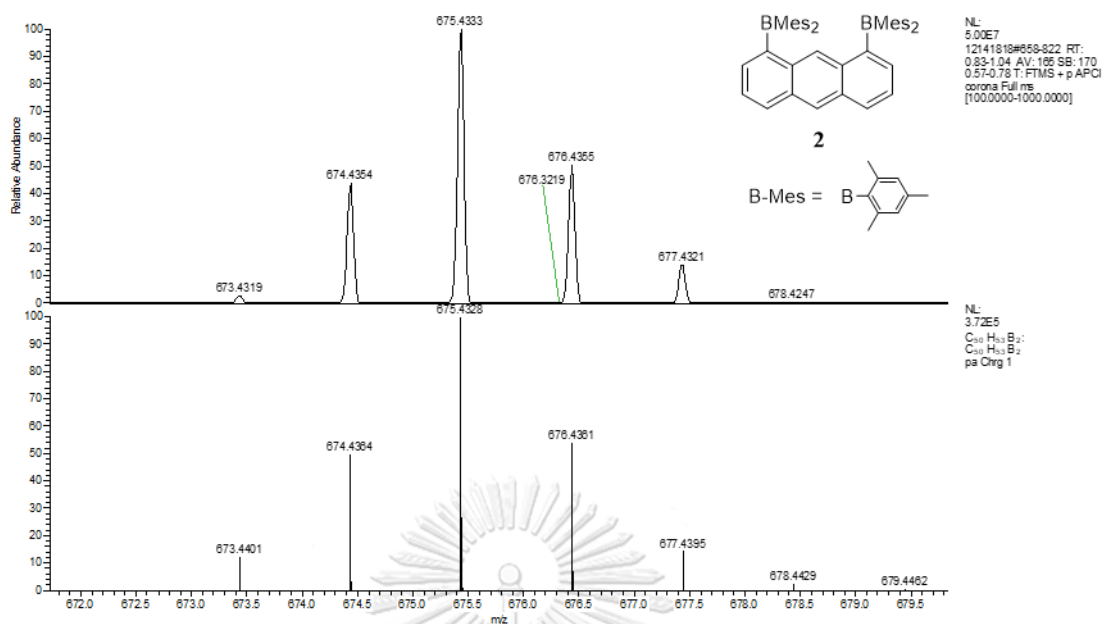


Figure 2.14 HRMS (APCI⁺) of [2+H]⁺ observed (a) and calculated (b).

Crystals of **1** and **2** suitable for X-ray diffraction analysis were obtained by layering a solution of **1** and **2** in CH₂Cl₂ with methanol. The solid-state structures of **1** and **2** are shown in Figure 2.15 and the crystallographic parameters are presented in Table 2.1 and Table 2.2. Compound **1** crystallizes in the C2/c space group and reveals a propeller arrangement as expected with angles about the central boron atom measuring between 116.1(3) and 122.5(3)° in a trigonal planar geometry. The structure of **2** also crystallizes in the C2/c space group with half of the molecule in the asymmetric unit. There is slightly more variation in the bond angles about the boron center, between 114.8(2) and 123.9(2)°. As a result of the steric crowding, the two boron centers are separated by 5.576(4) Å.

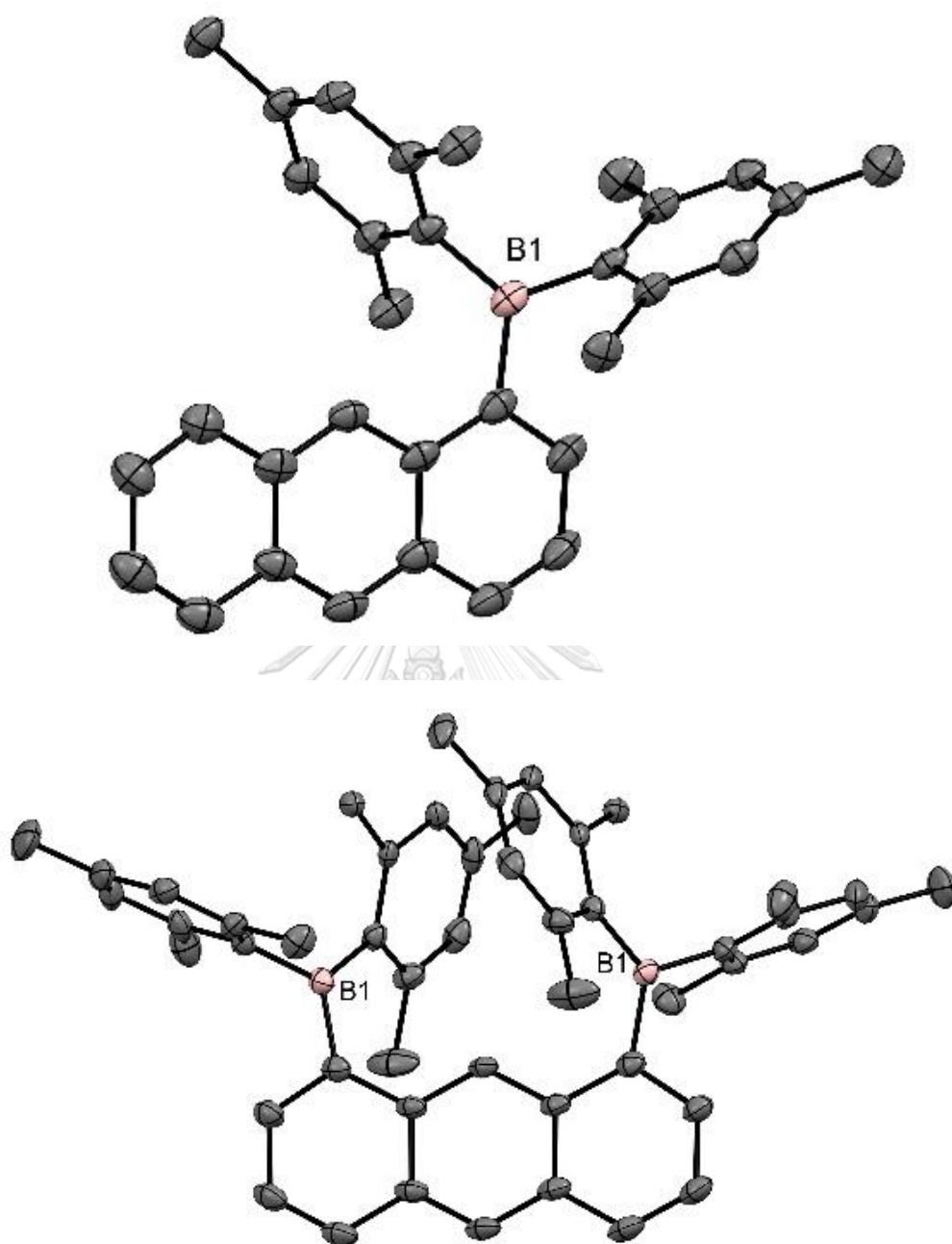


Figure 2.15 Solid-state structures of **1** (top) and **2** (bottom). Hydrogen atoms omitted for clarity. Thermal ellipsoids drawn at 50%.

Table 2.1 Crystal Data and Structure Refinement Details for **1**.

Empirical formula	C ₃₂ H ₃₁ B
Formula weight	426.38
Temperature	109.99 K
Wavelength	0.71073 Å
Crystal system	Monoclinic
Space group	C2/c
Unit cell dimensions	a = 40.663(5) Å b = 8.0101(9) Å c = 15.645(2) Å α = 90°. β = 93.812(4)°. γ = 90°.
Volume	5084.5(11) Å ³
Z	8
Density (calculated)	1.114 Mg/m ³
Absorption coefficient	0.062 mm ⁻¹
F(000)	1824.0
Crystal size	0.344 x 0.172 x 0.05 mm ³
2θ range for data collection	5.22 to 54.97°.
Index ranges	-52 ≤ h ≤ 52, -10 ≤ k ≤ 10, -20 ≤ l ≤ 20
Reflections collected	28292
Independent reflections	5825 [R _{int} = 0.0636, R _{sigma} = 0.0594]
Completeness to theta = 25.242°	100.00%
Absorption correction	Semi-empirical from equivalents
Data / restraints / parameters	5825 / 0 / 304
Goodness-of-fit on F ²	1.214
Final R indices [I ≥ 2σ (I)]	R ₁ = 0.0959, wR ₂ = 0.2189
R indices (all data)	R ₁ = 0.1254, wR ₂ = 0.2330
Largest diff. peak and hole	1.15 and -0.37 e.Å ⁻³
CCDC deposition number	1946228

Table 2.2 Crystal data, data collection, and structure refinement for **2**.

Empirical formula	C ₅₀ H ₅₂ B ₂
Formula weight	674.53
Temperature	110(2) K
Wavelength	0.71073 Å
Crystal system	Monoclinic
Space group	C2/c
Unit cell dimensions	a = 15.5053(18) Å b = 19.059(2) Å c = 15.890(3) Å α = 90° β = 113.204(3)° γ = 90°
Volume	4316.0(11) Å ³
Z	4
Density (calculated)	1.038 Mg/m ³
Absorption coefficient	0.058 mm ⁻¹
F(000)	1448.0
Crystal size	0.675 x 0.346 x 0.312 mm ³
2θ range for data collection	5.104 to 60.064°
Index ranges	-21 ≤ h ≤ 21, -26 ≤ k ≤ 26, -22 ≤ l ≤ 22
Reflections collected	27732
Independent reflections	6307 [R _{int} = 0.0654, R _{sigma} = 0.0624]
Completeness to theta = 25.242°	100.00%
Absorption correction	Semi-empirical from equivalents
Data / restraints / parameters	6307 / 0 / 241
Goodness-of-fit on F ²	1.055
Final R indices [I ≥ 2σ (I)]	R ₁ = 0.0834, wR ₂ = 0.1990
R indices (all data)	R ₁ = 0.1248, wR ₂ = 0.2239
Largest diff. peak and hole	0.39 and -0.44 e.Å ⁻³
CCDC deposition number	1946229

2.2.2 Photophysical properties

UV-vis spectra of **1** and **2** were investigated and compared to that of unfunctionalized anthracene (Figure 2.16). The unfunctionalized anthracene has absorption bands around 300-390 nm attributed to the π - π^* transitions of the anthryl chromophore. In the case of **1**, the absorption spectrum displays two major low energy bands centered at 325 nm and 406 nm, respectively. The first one is reminiscent of that observed for simple triaryl boranes such as trimesityl borane [48] and can be assigned to the boron centered chromophore, with the main transition having ligand-to-element charge-transfer character. The second band shows three vibronic features that closely resemble the 0-0, 0-1 and 0-2 vibronic bands of anthracene. On this basis, this band is assigned to the $S_0 \rightarrow S_1$ transition of the anthryl chromophore which has π -to- π^* character. For comparison, the energy of this band is redshifted with respect to that of the unfunctionalized anthracene (406 nm (**1**) vs. 378 nm (anthracene)). This redshift is due to the extension of the conjugation of the π^* of the anthryl group to the empty p-orbital of the boron atom that lowers its energy gap.

In the case of **2**, the spectrum again features a low energy band whose vibronic features are less distinct but suggests an assignment to the $S_0 \rightarrow S_1$ transition of the anthryl chromophore. This band is further redshifted with respect to that of the unfunctionalized anthracene (419 nm (**2**) vs. 378 nm (anthracene)) as the number of boryl groups increases, suggesting that π -conjugation is extended by the presence of the additional p- π^* conjugation. The features observed at higher energy, past 370 nm, are less readily assignable than in the case of **1** but probably involve the boron-centered chromophores.

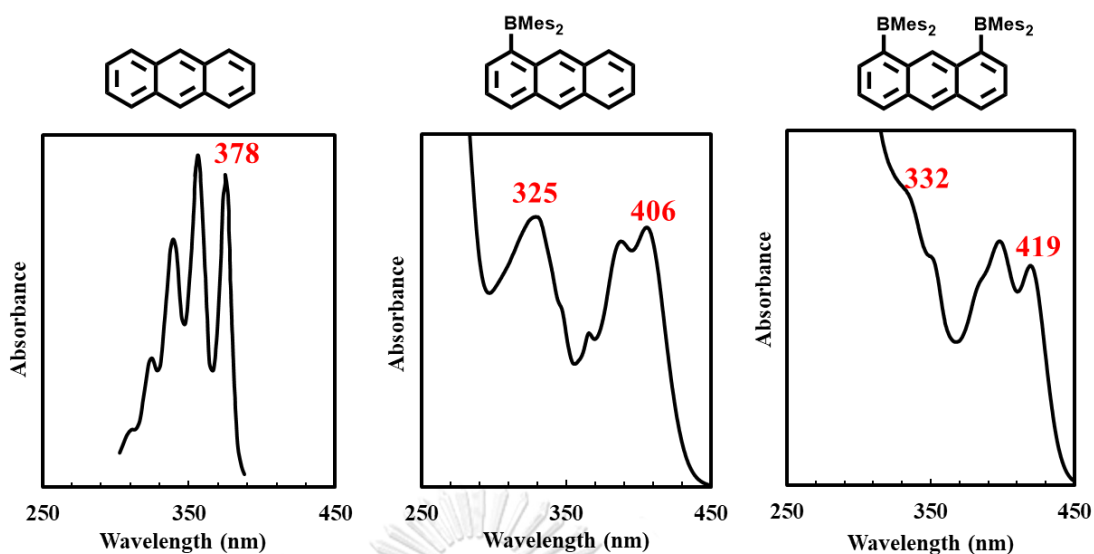


Figure 2.16 UV-vis spectra of pure anthracene (left), **1** (middle), and **2** (right).

To obtain deeper insights into the electronic structures of **1** and **2**, molecular orbital calculations were performed. The results reveal that the LUMO is perturbed by the appended boron atoms, as seen by the mixing of the vacant p-orbital on boron and the anthracene π -system (Figure 2.17). Furthermore, as indicated by time dependent density functional theory (TD-DFT) calculations, electronic excitations from the HOMO and HOMO-1 to the LUMO are the major contributors to the bands outlined above. The calculated bands for the transition are close to those observed experimentally, the data being included in Table 2.3. These calculations also reinforce the assignment of the low energy band as the π -to- π^* (HOMO \rightarrow LUMO) transition, and the higher energy bands as the charge-transfer from the mesityl groups to the borylated anthracene moiety (HOMO-1 \rightarrow LUMO).

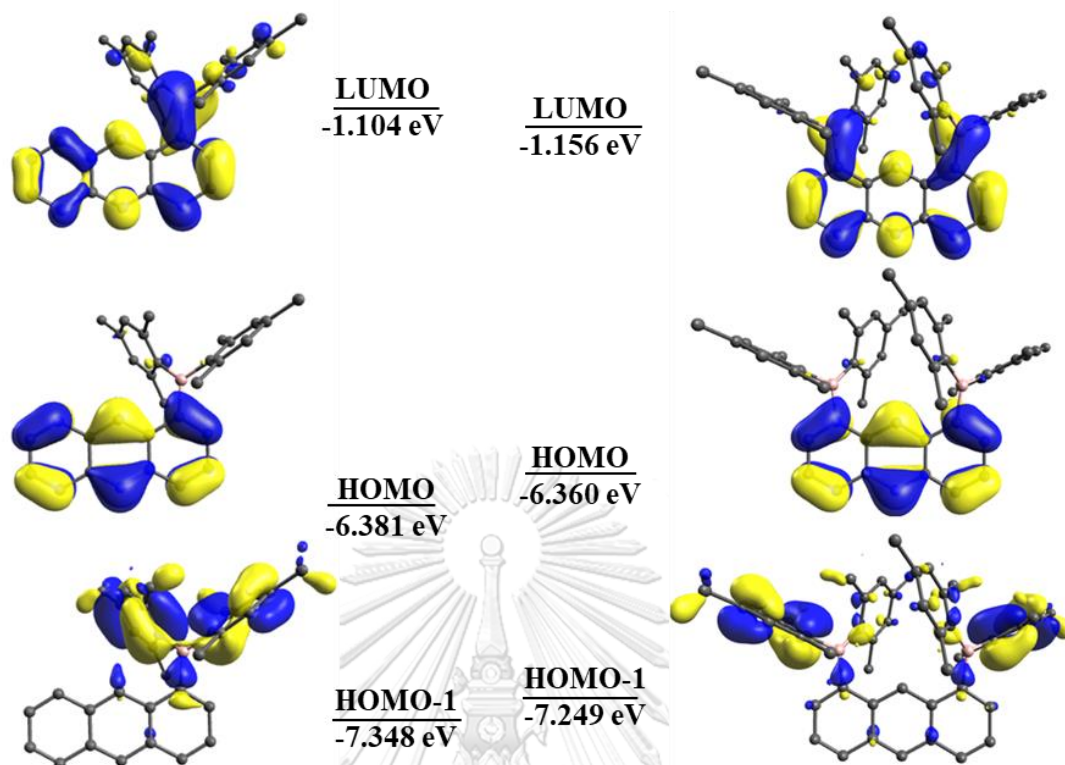


Figure 2.17 Depiction of LUMO, HOMO and HOMO–1 of **1** (left) and **2** (right). Isosurface value = 0.03.

Table 2.3 Computed UV-vis of **1** and **2** compared with experimental values.

Compound	λ_{max}^{UV-Vis} (HOMO→LUMO)		λ_{max}^{UV-Vis} (HOMO–1→LUMO)	
	Exp.	Comp.	Exp.	Comp.
1	406	416	325	344
2	419	421	332	351

2.2.3 Electrochemical properties

The electrochemistry of **1** and **2** was investigated using cyclic voltammetry. Most triarylboranes are electroactive and undergo a one electron reduction corresponding to the formation of a boron centered radical [60]. An example of such a behavior is displayed by Mes_3B which is reduced at -2.73 V vs. Fc/Fc^+ in THF [61]. As shown in Figure 2.18, the cyclic voltammograms of **1** and **2** in THF display a much more complicated behavior. The potential for the first reduction of **1** and **2** appears at $E_{1/2}$ -2.23 V and -2.31 V, respectively. It is interesting to note that the potential measured for both compounds is close to one another. This result is consistent with the calculated LUMO energies that are also virtually identical, differing by only 0.05 eV. Both compounds show a quasi-reversible reduction wave which is anodically shifted from those of triaryl boranes and close to the redox potential of simple anthracene derivatives [62, 63]. Thus, we can assign this first reduction to an anthracene-dominated process. This assignment is consistent with the LUMO of these derivatives which shows extensive participation of the backbone, with a contribution from the boron atoms.

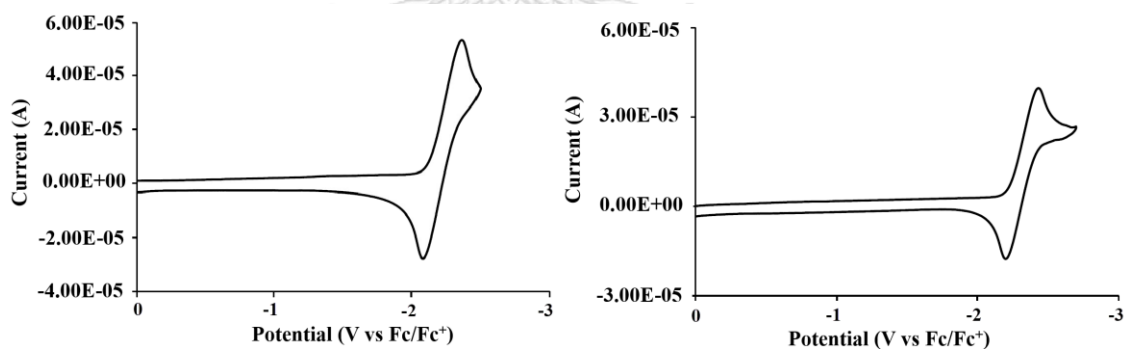


Figure 2.18 Cyclic voltammograms of **1** (left) and **2** (right) in THF with 0.1 M TBAPF_6 as electrolyte, scan rate 200 mV/s and potential referenced to Fc/Fc^+ .

2.2.4 Quantum yields

Fluorescence quantum yields (QY) were calculated based on gradients of integrated emission (IE) versus absorbance at excitation wavelength (Abs) for a series of measurements on the sample or fluorescence standard, according to the following equation [64].

$$\begin{aligned}\Phi_{sample} &= \Phi_{std} \times \frac{IE_{sample}}{IE_{std}} \times \frac{Abs_{std}}{Abs_{sample}} \times \left(\frac{\eta_{sample}}{\eta_{std}}\right)^2 \\ &= \Phi_{std} \times \frac{Grad_{sample}}{Grad_{std}} \times \left(\frac{\eta_{sample}}{\eta_{std}}\right)^2\end{aligned}$$

where η is refractive index of solvent. The resulting gradient plots obtained for **1** and **2** are shown in Figure 2.19. Both **1** and **2** are fluorescent and display QY of 0.41 and 0.23, respectively determined using anthracene as the standard and $\eta = 1.43$ for cyclohexane solutions.

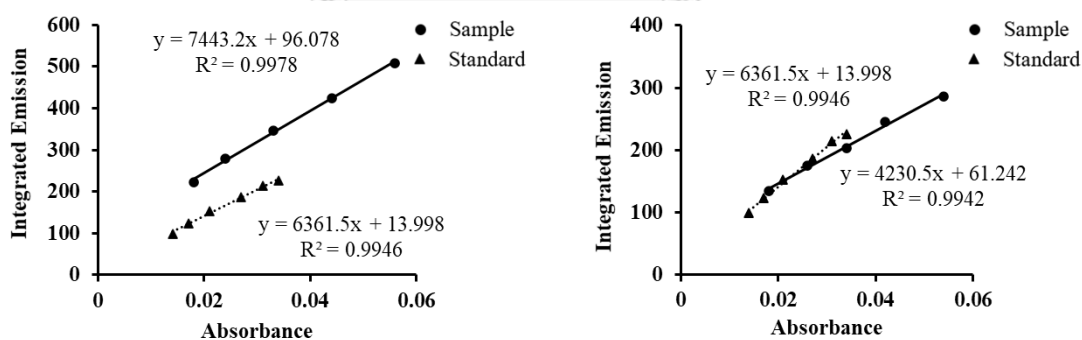


Figure 2.19 Quantum yield gradient plot of **1** (left) and **2** (right).

2.2.5 Fluoride binding properties

The photophysical responses of **1** and **2** to fluoride were investigated via UV-vis titration studies. As shown in Figure 2.20, the UV-vis spectrum of **1** in THF displays two main absorption bands at 325 nm and 406 nm. Incremental addition of TBAF to a solution of **1** led to a linear decrease of the absorbance, accompanied by a conversion to a new absorbance spectrum that matches to the bands of the pure anthracene. Fitting of these spectral data on the basis of a 1 : 1 binding isotherm using a method reported previously [65] affords a fluoride binding constant $K(\text{F}^-) = 7 \times 10^6$ M.

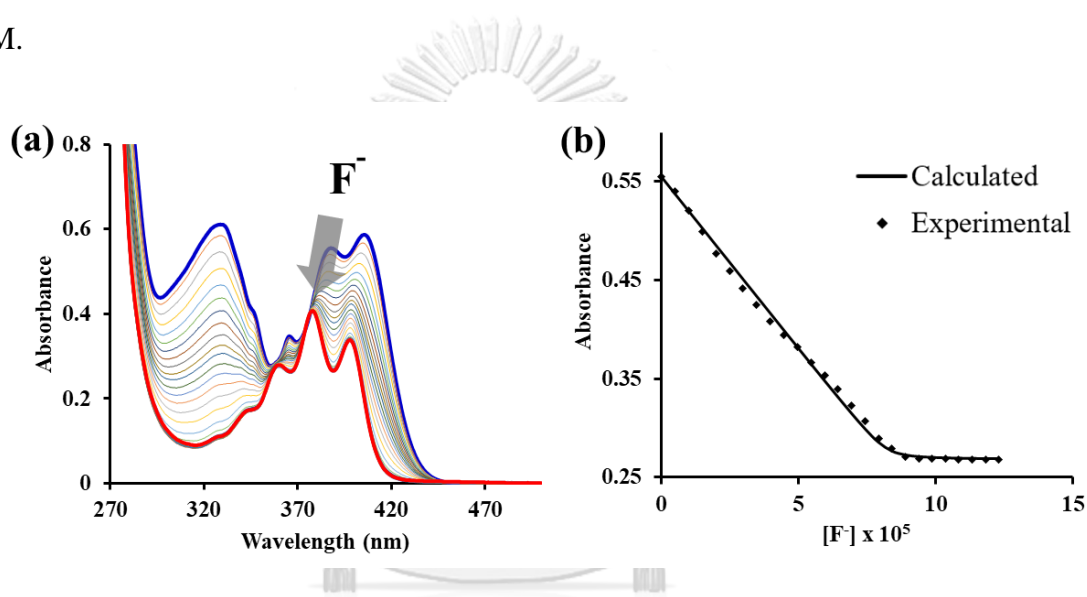


Figure 2.20 (a) Changes in UV-vis absorption spectra of **1** (6.0×10^{-5} M in THF) upon titration with TBAF. (b) Experimental and calculated 1:1 binding isotherm for the addition of F^- to **1**, based on the absorbance measured at 388 nm.

To collect additional evidences for the binding of fluoride to **1**, we also studied the binding of fluoride by ^{11}B NMR titration experiments in CD_2Cl_2 (Figure 2.21). The results show the complete disappearance of the resonance of the free borane upon the addition of one equivalent of TBAF and the new resonance is observed at about 6 ppm. This high field region is expected for four-coordinate boron centers that can be assigned to the anionic chelate complex $[\mathbf{1}-\text{F}]^-$. Furthermore, this binding mode was further verified via mass spectrometry whereby a signal was detected at $m/z = 445.2503$ (calc. = 445.2497) for the parent ion of $[\mathbf{1}-\text{F}]^-$ (Figure 2.22).

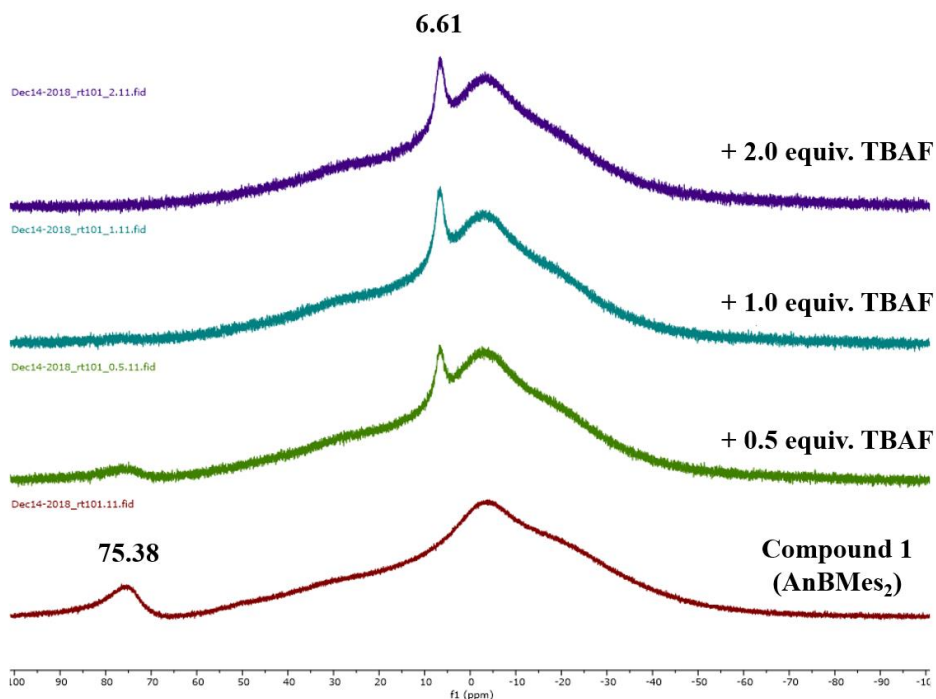


Figure 2.21 ¹¹B NMR spectra of **1** in CD₂Cl₂ solutions upon the addition of TBAF.

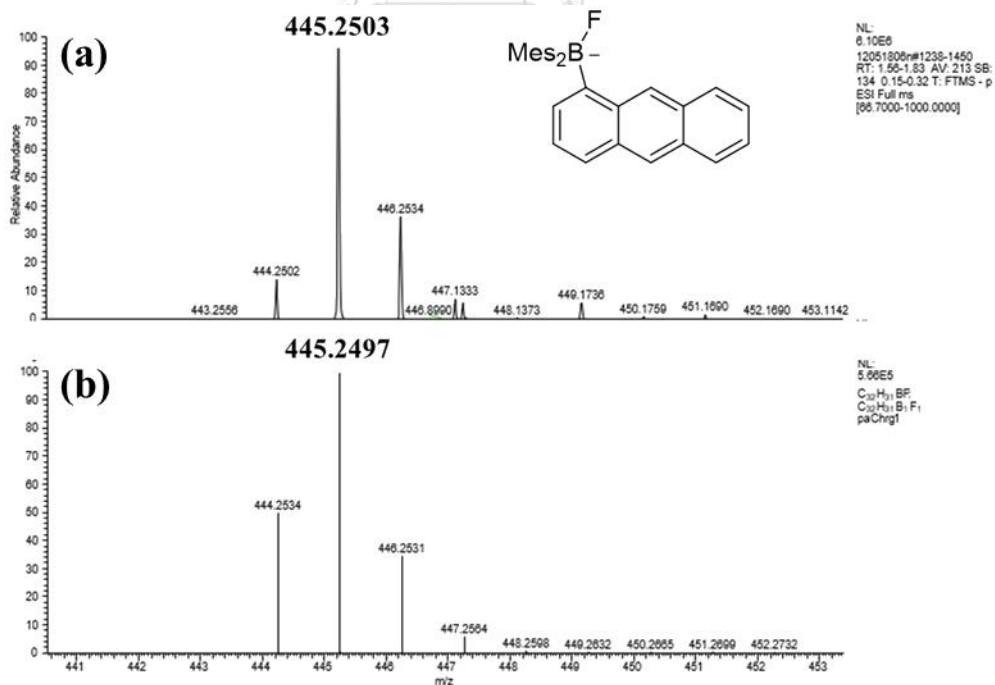


Figure 2.22 HRMS (ESI⁻) of [1-F]⁻ observed (a) and calculated (b).

In a similar process, addition of TBAF to a solution of **2** in THF resulted in a new absorbance profile in the UV-vis spectrum for the posited complex $[\mathbf{2}-\text{F}]^-$ (Figure 2.23). The absorption data was modeled on the basis of a 1:1 binding isotherm affording fluoride binding constants $K(\text{F}^-) = 4 \times 10^6 \text{ M}$. This value is quite close with the same order of magnitude to that measured for **1**. Mass spectrometry also supports the formation of $[\mathbf{2}-\text{F}]^-$ with a signal detected at $m/z = 693.4249$ (calc. = 693.4234) as show in Figure 2.24. It is interesting to note that the corresponding molecular ion for the bis-functionalized $[\mathbf{2}-\text{F}_2]^{2-}$ is not being detected.

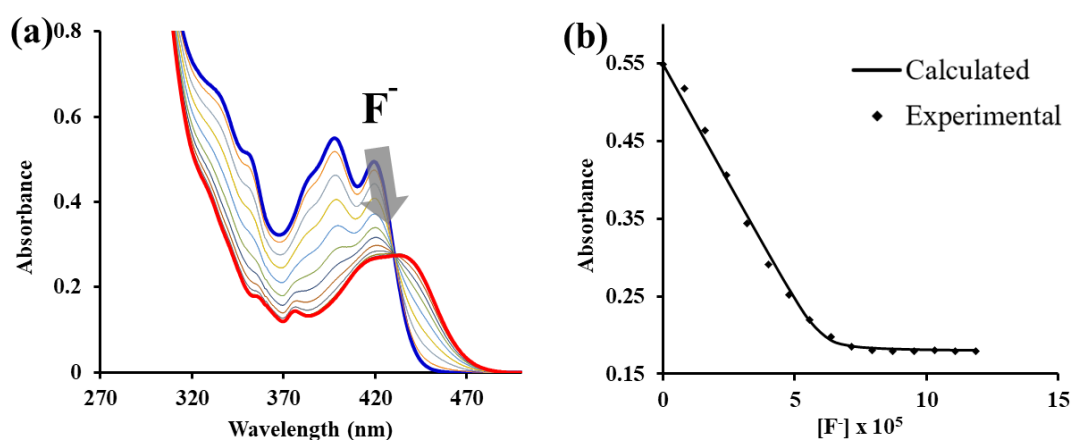


Figure 2.23 (a) Changes in UV-vis absorption spectra of **2** ($6.0 \times 10^{-5} \text{ M}$ in THF) upon titration with TBAF. (b) Experimental and calculated 1:1 binding isotherm for the addition of F^- to **2**, based on the absorbance measured at 398 nm.

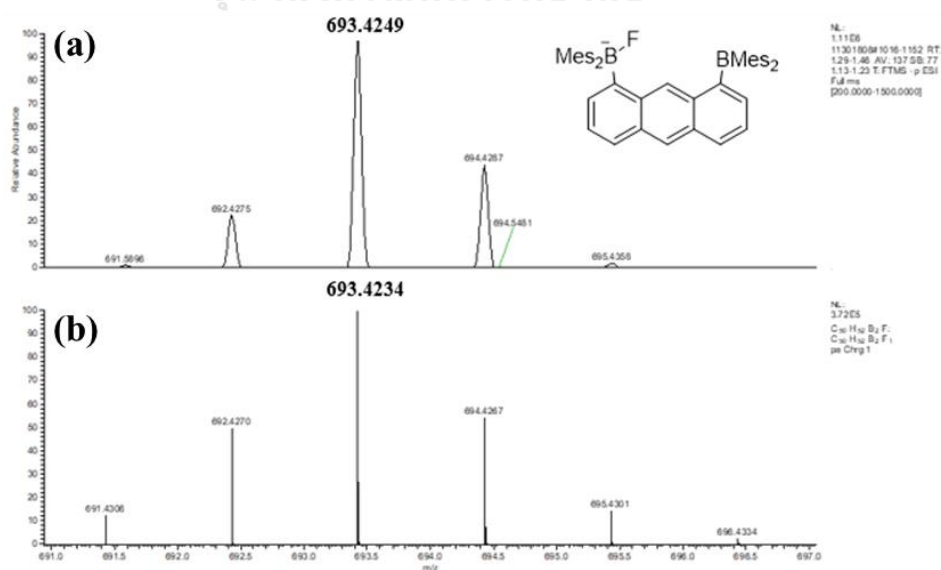


Figure 2.24 HRMS (ESI⁻) of $[\mathbf{2}-\text{F}]^-$ observed (a) and calculated (b).

To understand the UV-vis response of compound **1** and **2** toward fluoride ion, theoretical calculations on their fluoride adducts were performed. Diagrams showing the HOMO and LUMO orbitals of the fluoride complexes ($[1-F]^-$ and $[2-F]^-$) are presented in Figure 2.25. It is also noteworthy that upon fluoride binding to the monoborane **1**, the resulting UV-vis spectra closely resemble to that of the unfunctionalized anthracene backbone. This effect is also readily detectable with the naked eye, with a distinct blue shift of the color from deep yellow to light yellow upon conversion from **1** to $[1-F]^-$. Theoretical studies show that the addition of fluoride to **1** removes the borane from the conjugated system producing essentially idealized frontier molecular orbitals on pure anthracene. The calculations are in agreement with the experimental results confirming that the incoming fluoride ions donate an electron pair to boron centers, thus inhibiting the conjugation between the vacant p-orbital on boron and anthracene π -system.

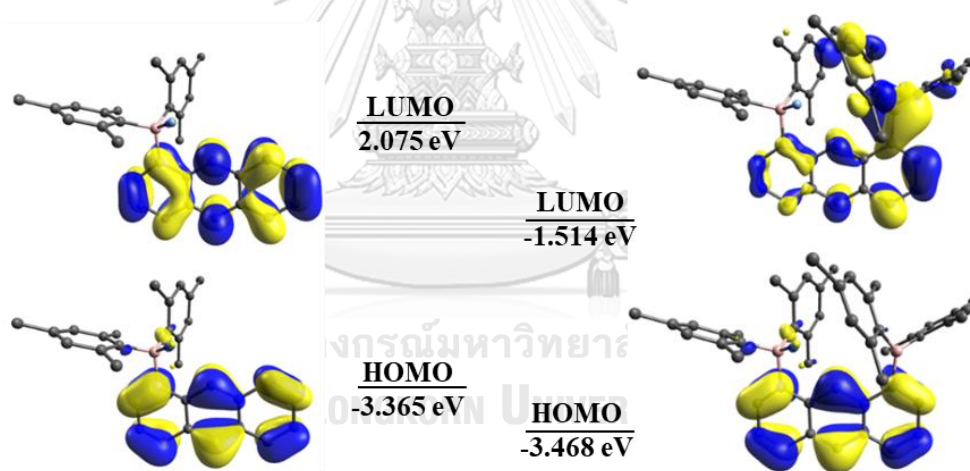


Figure 2.25 Depiction of frontier molecular orbitals of $[1-F]^-$ (left) and $[2-F]^-$ (right). Isosurface value = 0.03.

By contrast, conversion of **2** into $[2-F]^-$ leads to the appearance of a red-shifted absorption band. This band is assigned to an anthracene π -to-borane charge transfer band, as supported by the fact that the HOMO of the anionic complex has dominant anthracene character while the LUMO shows high boron p-orbital character.

TD-DFT studies also corroborate these findings with a dominant vertical excitation being noted at 383 nm for $[1-F]^-$ which is in approximate agreement with the 0-0, π -to- π^* transition observed experimentally at 399 nm. Similarly, $[2-F]^-$ shows a theoretical excitation from TD-DFT calculations at 446 nm for the anthracene π -to-borane charge transfer band with the experimental data giving a broad absorbance band centered at 435 nm.

Further, the response of the boranes toward fluoride ions was examined in emission mode. As shown in Figure 2.26, the addition of fluoride to **1** causes a blue shift of emission spectra and the emission color changes from sky blue to dark blue. The emission profile become almost identical to those of unfunctionalized anthracene as expected by removal of the conjugation with the boryl group. Interestingly, a red shift is observed in the case of **2** and the color of the emission changes from green to blue. The red shift of this emission is consistent with the red shift observed in the UV-vis spectrum of **2** upon anion binding. Accordingly, this emission can be assigned to an intramolecular electron-rich anthracene to borane charge transfer.

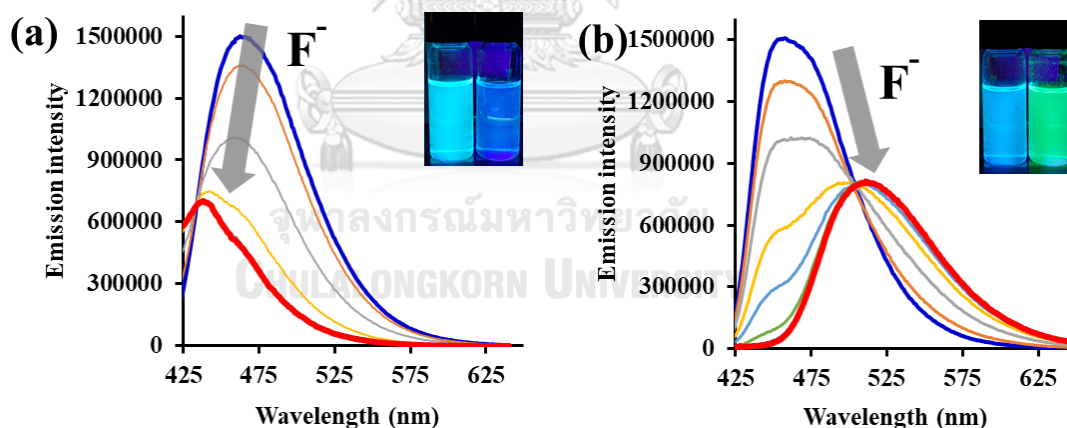


Figure 2.26 Fluorescence emission spectra of **1** (a) and **2** (b) upon fluoride binding and their respective color changes when irradiated with UV light.

2.2.6 Cyanide binding properties

Next, we turned our attention to the cyanide anion to determine if diatomic molecules could also be captured by these systems. To this end, both boranes were subjected to cyanide titration experiments monitored by UV-vis spectroscopy and the results are shown in Figure 2.27 and Figure 2.28 for **1** and **2**, respectively.

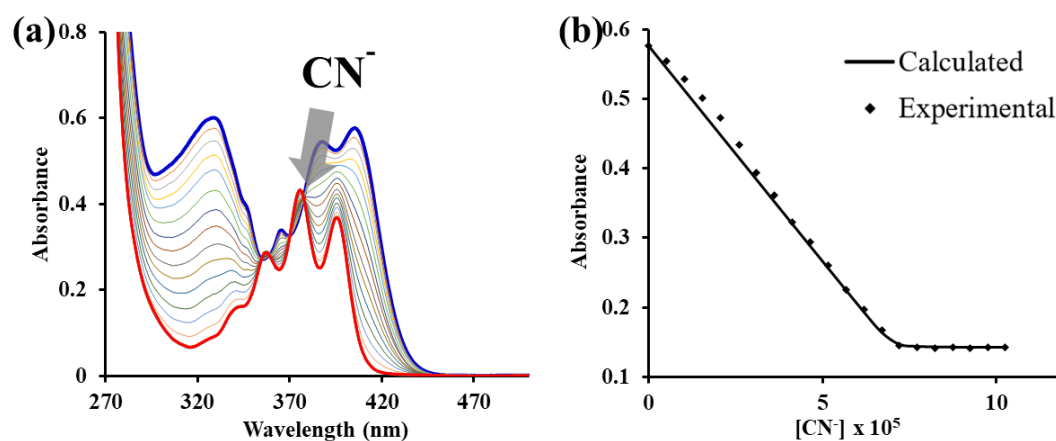


Figure 2.27 (a) Changes in UV-vis absorption spectra of **1** (6.0×10^{-5} M in THF) upon titration with TBACN. (b) Experimental and calculated 1:1 binding isotherm for the addition of CN⁻ to **1**, based on the absorbance measured at 388 nm.

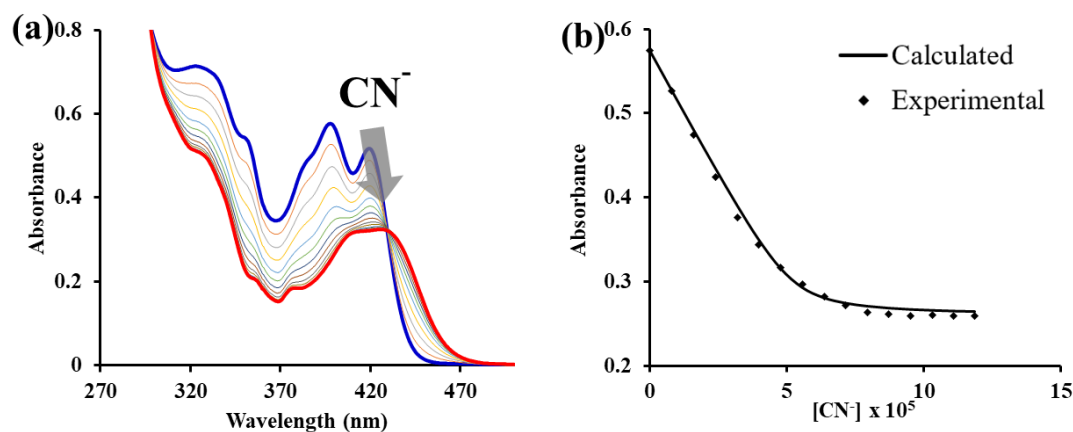


Figure 2.28 (a) Changes in UV-vis absorption spectra of **2** (6.0×10^{-5} M in THF) upon titration with TBACN. (b) Experimental and calculated 1:1 binding isotherm for the addition of CN⁻ to **2**, based on the absorbance measured at 398 nm.

The incremental addition of TBACN to a solution of **1** and **2** in THF induced notable changes of the UV-vis spectra. This spectral change is appeared to be the same as those of the titration of fluoride. The titration data could be fitted to a 1 : 1 binding isotherm in both cases. Extracting binding constants from these data established that **1** is particularly potent in cyanide binding with $K(\text{CN}^-) = 3 \times 10^7 \text{ M}^{-1}$.¹ Interestingly, the diborane **2** with the binding constant $K(\text{CN}^-)$ of $9 \times 10^5 \text{ M}^{-1}$ is over an order of magnitude less effective than those of the monoborane **1**. This may be the result of steric crowding around the boron center precluding effective binding of larger diatomic molecules. In addition, as shown in Figure 2.29 and Figure 2.30, mass spectrometry also supports a similar 1 : 1 binding mode with the parent ion being detected at $m/z = 452.2550$ (calc. = 452.2544) for $[\mathbf{1}-\text{CN}]^-$ and $m/z = 700.4300$ (calc. = 700.4291) for $[\mathbf{2}-\text{CN}]^-$.

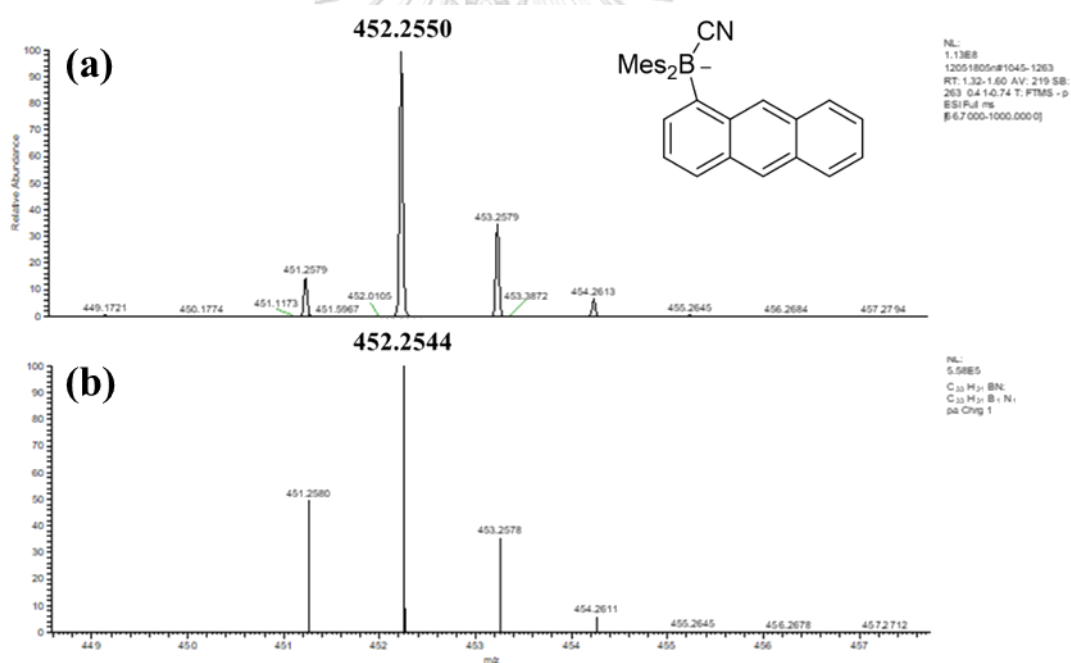


Figure 2.29 HRMS (ESI⁻) of $[\mathbf{1}-\text{CN}]^-$ observed (a) and calculated (b).

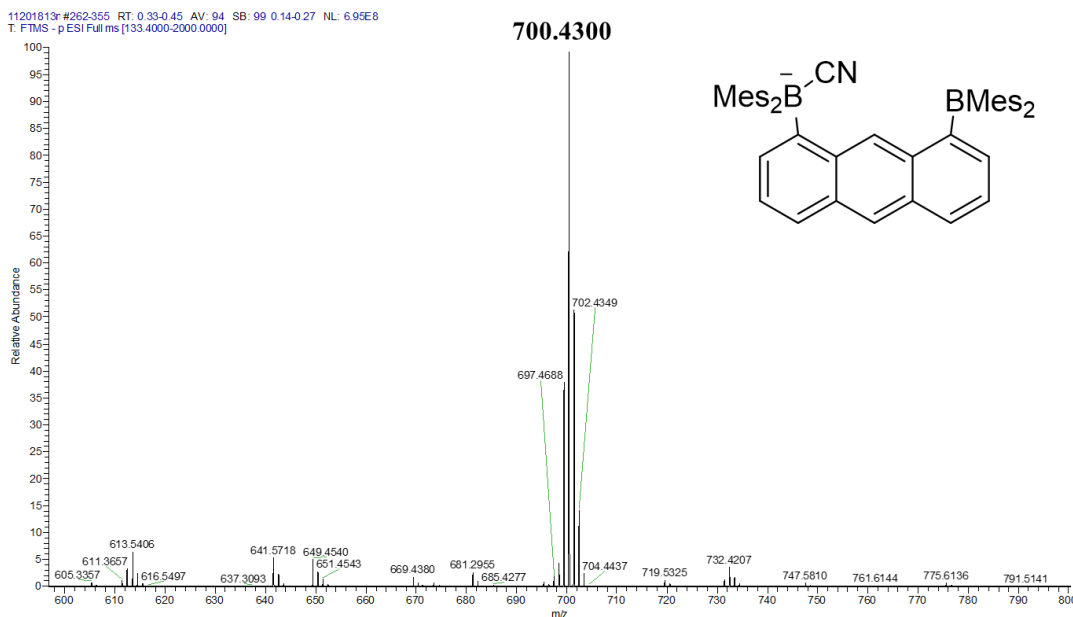


Figure 2.30 HRMS (ESI⁻) of [2-CN]⁻.

Emission profiles of **1** and **2** obtained from cyanide titration experiments are shown in Figure 2.31. The spectral changes are similar to those observed in fluoride titration. Upon incremental addition of cyanide ions, the emission bands gradually decrease in intensity and exhibit a blue shift in the case of **1** and a red shift in the case of **2** resulting in emission color changes (Figure 2.31, inset).

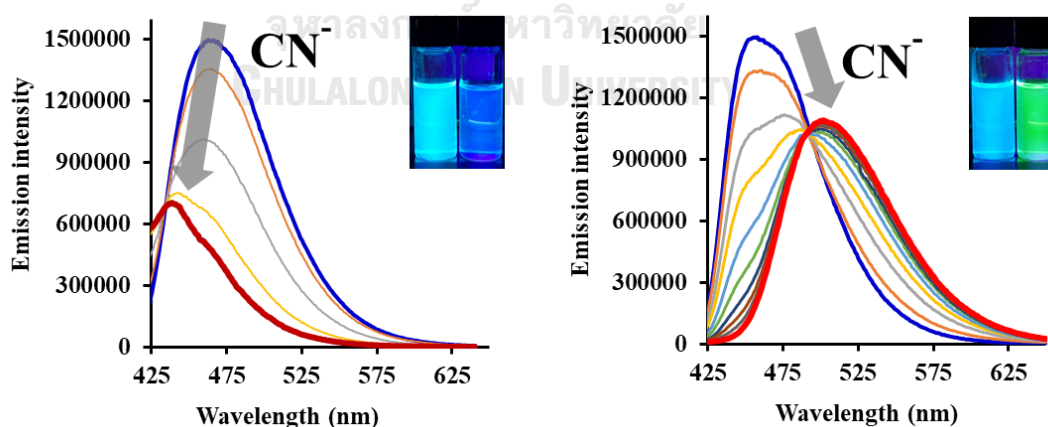


Figure 2.31 Fluorescence emission spectra of **1** (a) and **2** (b) upon cyanide binding and their respective color changes when irradiated with UV light.

Considering the binding mode of cyanide to diborane **2**, the spectra obtained with cyanide binding are similar to those of the fluoride binding indicating that the cyanide anion in $[2-CN]^-$ is not bridging the two boron centers. We propose that C–H unit at the 9 position of the anthracenediyl backbone of **2** hinders the bridging mode.

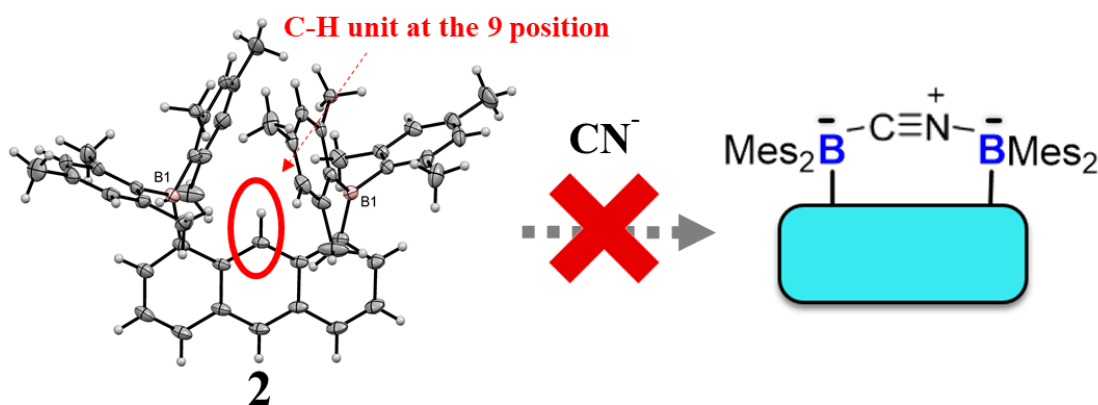


Figure 2.32 Diagrams showing the C–H unit at the 9 position of anthracene hindering the cyanide bridging mode.

2.3 Conclusions

The mono- and bis-functionalized anthracene derivatives **1** and **2** have been synthesized. UV-vis studies of these compounds reveal how progressive depletion of electron density of the anthracene backbone results in a red-shift of the $\pi-\pi^*$ transition. This is achieved by virtue of increasing $p-\pi^*$ conjugation through the addition of one or two boryl units. These findings are supported by theoretical calculations which confirm the HOMO–LUMO character of the transition and the perturbation imparted by the boron atoms. Anion responses of **1** and **2** show the affinity of the monofunctionalized species toward both fluoride and cyanide anions. Interestingly, steric crowding in **2** results in lower affinity for the diatomic cyanide anion. Subsequent fluorescence studies outline some notable differences in the emission profiles of **1** and **2**. Whereas a blue-shift in the emission spectrum of **1** is observed upon fluoride association, that of **2** displays an unexpected red-shift resulting from an electron-rich anthracene π -to-borane charge transfer (Figure 2.33).

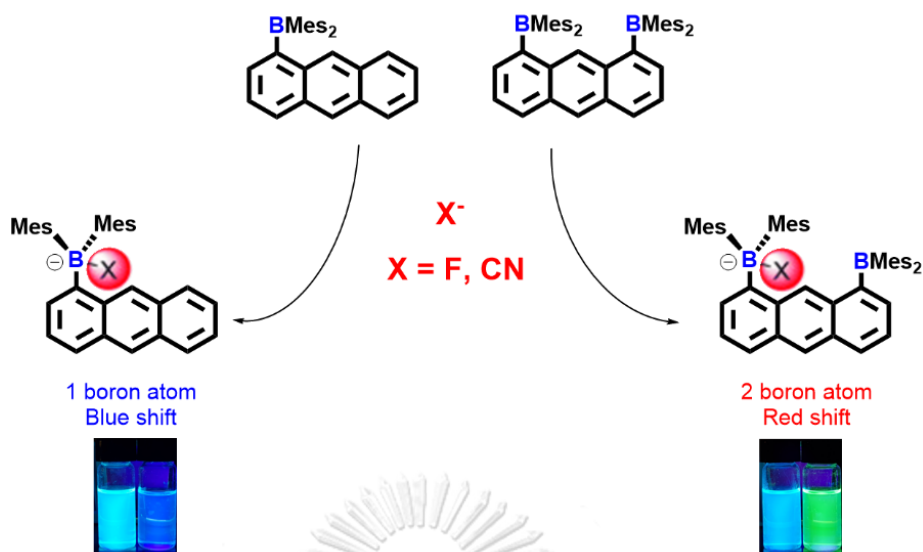


Figure 2.33 Two boranes bind the toxic fluoride and cyanide anions to afford the corresponding 1:1 complexes.

2.4 Experimental section

2.4.1 Synthesis of 1-dimesitylborylanthracene (1)

n-BuLi (2.5 M in hexanes, 0.77 mL, 1.79 mmol, 2 equiv.) was added to a solution of 1,8-dibromoanthracene (0.3 g, 0.89 mmol, 1 equiv.) and TMEDA (0.34 mL, 2.23 mmol, 2.5 equiv.) in THF (5 mL) at -78 °C. After stirring for 1 hour at this temperature, the resulting mixture was treated with Mes₂BF (0.27 g, 1.02 mmol, 1 equiv.) and left to stir at room temperature for 18 h. At this time, a saturated NH₄Cl solution was added to quench the reaction and the aqueous phase was washed with CH₂Cl₂ (2 × 5 mL). The organic phases were combined, dried over anhydrous MgSO₄ and concentrated to a yellow/orange oil. Washing this oil with MeOH (2 × 2 mL) afforded a yellow powder which was crystallized by layering a saturated CH₂Cl₂ solution with MeOH. Yield: 169 mg, 0.39 mmol, 44%.

¹H NMR (400 MHz, CDCl₃, 298 K) δ /ppm: 8.38 (d, $J_{\text{HH}} = 21.1$ Hz, 2H, anth-H), 8.08 (d, $J_{\text{HH}} = 8.4$ Hz, 1H, anth-H), 7.96 (d, $J_{\text{HH}} = 8.4$ Hz, 1H, anth-H), 7.59 (d, $J_{\text{HH}} = 8.4$ Hz, 1H, anth-H), 7.52 (d, $J_{\text{HH}} = 6.4$ Hz, 1H, anth-H), 7.30–7.46 (m, 3H, anth-H), 6.80 (s, 4H, Mes-H), 2.31 (s, 6H, p-Me), 2.00 (s, 12H, o-Me).

^{13}C NMR (101 MHz, CDCl_3 , 298 K) δ /ppm 140.8 (s), 139.1 (s), 134.8 (s), 133.7 (s), 132.4 (s), 131.8 (s), 131.8 (s), 131.5 (s), 129.0 (s), 128.5 (s), 127.9 (s), 127.1 (s), 126.8 (s), 125.5 (s), 125.3 (s), 125.2 (s), 23.3 (s), 21.4 (s). Resonances for carbons bound to boron are not observed.

^{11}B NMR (128 MHz, CDCl_3 , 298 K) δ /ppm: 74.9 (br. s).

HRMS (APCI $^+$) m/z calculated for $[\text{C}_{32}\text{H}_{32}\text{B}]^+$: 427.2592, found: 427.2588.

2.4.2 Synthesis of 1,8-bis(dimesitylboryl)anthracene (2)

n-BuLi (2.5 M in hexanes, 0.77 mL, 1.79 mmol, 2 equiv.) was added to a solution of 1,8-dibromoanthracene (0.3 g, 0.89 mmol, 1 equiv.) and TMEDA (0.34 mL, 2.23 mmol, 2.5 equiv.) in THF (5 mL) at $-78\text{ }^\circ\text{C}$. After stirring for 1 hour at this temperature, the resulting mixture was treated with Mes_2BF (0.55 g, 2.05 mmol, 2 equiv.) and left to stir at room temperature for 18 h. At this time, a saturated NH_4Cl solution was added to quench the reaction and the aqueous phase was washed with CH_2Cl_2 (2×5 mL). The organic phases were combined, dried over anhydrous MgSO_4 and concentrated to a yellow/orange oil. Washing this oil with MeOH (2×2 mL) afforded a yellow powder which was crystallized by layering a saturated CH_2Cl_2 solution with MeOH. Yield: 244 mg, 0.36 mmol, 40%.

^1H NMR (400 MHz, CDCl_3 , 298 K) δ /ppm: 8.45 (d, $J_{\text{HH}} = 14.6$ Hz, 2H, anth-H), 8.05 (d, $J_{\text{HH}} = 7.4$ Hz, 2H, anth-H), 7.30–7.38 (m, 4H, anth-H), 6.70 (s, 8H, Mes-H), 2.27 (s, 12H, *p*-Me), 1.83 (s, 24H, *o*-Me).

^{13}C NMR (101 MHz, CD_2Cl_2 , 298 K) δ /ppm: 151.2 (s), 141.8 (s), 139.7 (s), 134.7 (s), 134.1 (s), 132.5 (s), 132.0 (s), 129.1 (s), 128.3 (s), 128.1 (s), 125.7 (s), 23.4 (s), 21.6 (s).

^{11}B NMR (128 MHz, CDCl_3 , 298 K) δ /ppm: 74.6 (br. s).

HRMS (APCI $^+$) m/z calculated for $[\text{C}_{50}\text{H}_{53}\text{B}_2]^+$: 675.4328, found: 675.4333.

2.4.3 X-ray crystallography

The crystallographic measurements were performed at 110(2) K using a Bruker APEX-II CCD area detector diffractometer (Mo-K α radiation, $\lambda = 0.71069$ Å). For both **1** and **2**, a specimen of suitable size and quality was selected and mounted onto a nylon loop. Semi-empirical absorption corrections were applied. The structures were solved by direct methods, which successfully located most of the non-hydrogen atoms. Subsequent refinement using a difference map on F^2 using the SHELXTL/PC package (version 6.1) allowed location of the remaining nonhydrogen atoms which were refined anisotropically.

2.4.4 Cyclic voltammetry

Electrochemical experiments were performed with an electrochemical analyzer from CH Instruments (model 610A) with a glassy-carbon working electrode and a platinum auxiliary electrode. The reference electrode was built from a silver wire inserted into a small glass tube fitted with a porous Vycor frit at the tip and filled with a THF solution containing tetrabutylammonium hexafluorophosphate (TBAPF₆, 0.1 M) and AgNO₃ (5 mM). All three electrodes were immersed in a deoxygenated THF solution (5 mL) containing TBAPF₆ (0.1 M) as a support electrolyte and the compound to be analyzed. Ferrocene was used as an internal standard and all potentials are reported with respect to $E_{1/2}$ of the Fc/Fc⁺ redox couple. All voltammograms were recorded at a scan rate of 200 mV s⁻¹.

2.4.5 Spectroscopy

UV-vis spectra were recorded at ambient temperature using an UV-2501PC spectrometer from Shimadzu Corporation. Emission spectra were taken on samples in capped quartz cuvettes under air on a PTI QuantaMaster fluorescence spectrofluorometer with entrance and exit slit widths of 2 nm and an integration time of 0.5 s.

Titration of 1 with fluoride in THF. A solution of **1** (3.0 mL, 6.0×10^{-5} M, THF) was titrated with 2 μ L aliquots of tetrabutylammonium fluoride trihydrate solution (TBAF, 9.0×10^{-3} M, THF). The changes in the absorption spectra based on the absorbance at 388 nm were fitted to a 1:1 binding isotherm. The fluoride binding constant was calculated to be 7×10^6 M⁻¹ using ϵ (**1**) = 6768 M⁻¹ cm⁻¹ and ϵ ([**1**-F]⁻) = 3268 M⁻¹ cm⁻¹.

Titration of 2 with fluoride in THF. A solution of **2** (3.0 mL, 6.0×10^{-5} M, THF) was titrated with 2 μ L aliquots of tetrabutylammonium fluoride trihydrate solution (TBAF, 9.0×10^{-3} M, THF). The changes in the absorption spectra based on the absorbance at 398 nm were fitted to a 1:1 binding isotherm. The fluoride binding constant was calculated to be 4×10^6 M⁻¹ using ϵ (**2**) = 9133 M⁻¹ cm⁻¹ and ϵ ([**2**-F]⁻) = 2983 M⁻¹ cm⁻¹.

Titration of 1 with cyanide in THF. A solution of **1** (3.0 mL, 6.0×10^{-5} M, THF) was titrated with 2 μ L aliquots of tetrabutylammonium cyanide solution (TBACN, 9.0×10^{-3} M, THF). The changes in the absorption spectra based on the absorbance at 388 nm were fitted to a 1:1 binding isotherm. The cyanide binding constant was calculated to be 3×10^7 M⁻¹ using ϵ (**1**) = 8242 M⁻¹ cm⁻¹ and ϵ ([**1**-CN]⁻) = 2028 M⁻¹ cm⁻¹.

Titration of 2 with cyanide in THF. A solution of **2** (3.0 mL, 6.0×10^{-5} M, THF) was titrated with 2 μ L aliquots of tetrabutylammonium cyanide solution (TBACN, 9.0×10^{-3} M, THF). The changes in the absorption spectra based on the absorbance at 398 nm were fitted to a 1:1 binding isotherm. The cyanide binding constant was calculated to be 9×10^5 M⁻¹ using ϵ (**2**) = 11038 M⁻¹ cm⁻¹ and ϵ ([**2**-CN]⁻) = 4980 M⁻¹ cm⁻¹.

2.4.6 Theoretical

Using the X-ray solid-state structures of complexes 1 and 2, optimizations of 1, 2, [1-F]⁻ and [2-F]⁻ using DFT methods were implemented in Gaussian 09 using the M06-2X functional and mixed basis set F/B: 6-31+G(d'), C/H: 6-31G(d'). Frequency calculations performed using the same level of theory on the optimized geometries found no imaginary frequencies. Time-dependent DFT (TD-DFT) calculations were conducted on the geometry optimized structures using MPW1PW91 functional and same basis sets as before using a polarizable continuum model with tetrahydrofuran as the solvent.



CHAPTER III
CYANIDE DETECTION USING DINUCLEAR COPPER(II) COMPLEX OF
ANTHRACENE BASED TRIPODAL TETRAMINE UNDER INDICATOR
DISPLACEMENT ASSAY

3.1 Introduction

Metal coordination complexes have been widely used in anion recognition. They act as recognition sites to bind various anions through Lewis acid–base interactions. Furthermore, incorporating multiple metal-binding centers into the complex is of current interest for the design of receptors. One such example is dinuclear metal coordination complexes. As shown in Figure 3.1, an organic scaffold holds two metal-binding centers at a specific distance, so they can be bridged by the target anions [66]. This chelating approach has been proved to be one of the most successful strategies to improve anion binding efficiency.

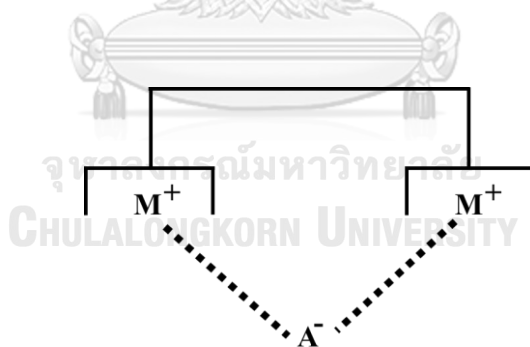


Figure 3.1 Anion recognition by a dinuclear metal coordination complex [66].

Recently, considerable efforts have been focused on the colorimetric chemosensing of anions based on metal coordination complexes in conjunction with indicator displacement assays (IDAs). This system has become particularly attractive due to its advantage of convenient use in aqueous media as well as without the complicated synthetic process [67]. The IDA strategy relies upon the competition between the indicator and the analyte in the host cavity. The indicator, which is initially bound to the receptor, is displaced by the target analyte, and finally obtains a change in the optical signals such as colorimetric and fluorescent readout. Based on this principal, the affinity between indicator–receptor is lower than that of the analyte–receptor [68].

The design of metal complex receptors in IDAs can be inspired by the active site of enzymes in biological processes. It is known that zinc(II) is present in many metalloenzymes such as dizinc phosphohydrolase which can bind inorganic phosphate and phosphorylated biomolecules [69]. Consequently, early IDAs were developed using multipodal zinc complexes as receptors to recognize phosphates. Most of these zinc complexes employ a dipicolylamine (DPA) moiety as the scaffold to hold the metal center. As shown in Figure 3.2, the DPA structure is a tridentate ligand with three nitrogen donors and can form stable complexes with divalent metals especially zinc(II). The Zn–DPA receptors provide vacant coordination sites that facilitates the binding of complexometric indicators resulting in a dramatic color change in solution. Thus, Zn–DPA receptors are popular for IDAs and many of them have been reported so far [68, 70, 71].

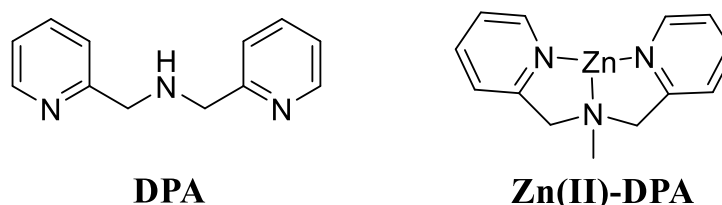


Figure 3.2 The chemical structure of dipicolylamine (DPA) ligand and Zn–DPA complex.

Examples of dinuclear zinc(II) complexes with two **DPA** units (receptor **XII** - **XV**) are illustrated in Figure 3.3. The first one is receptor **XII**, reported by Hamachi [72], having two Zn–**DPA** units separated by an anthracene spacer. This compound is an effective fluorescent sensor of dianionic phosphate derivatives. Another example is receptor **XIII** designed by Kim [23]. Based on IDAs, the colorimetric detection of phosphate has been achieved using **XIII** together with pyrocatechol violet as the indicator. Smith and coworkers [69] have employed thereceptor **XIV** and **XV** for fluorescent sensing of pyrophosphate. It occurs that the size of the spacer (the distance between the two Zn centers) impacts the degree of selectivity.

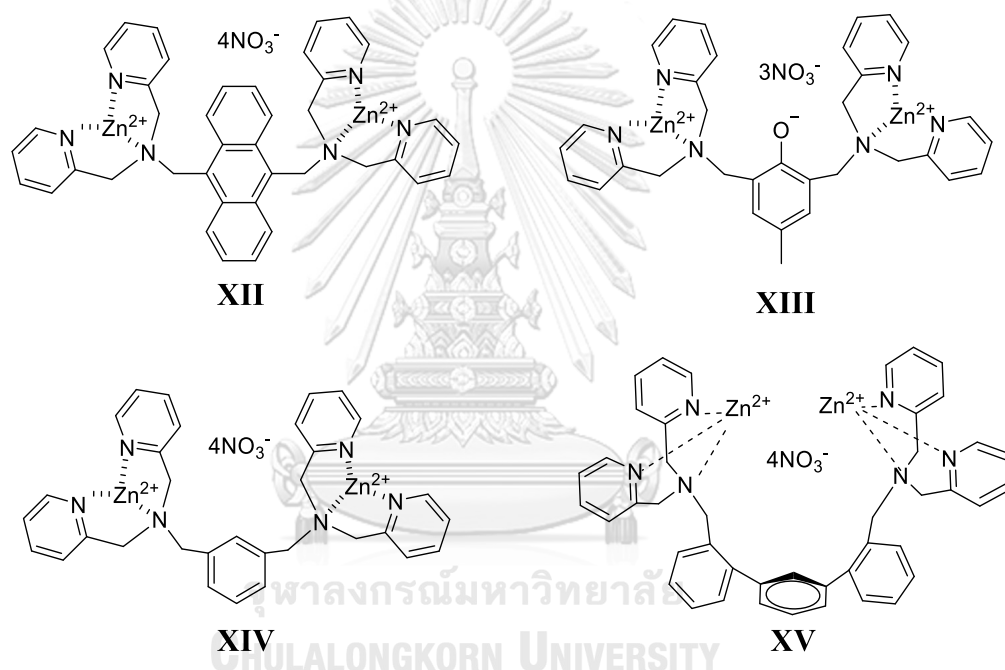


Figure 3.3 Examples of dinuclear Zn–**DPA** receptors employed in the IDA for the recognition of phosphorylated species.

Previous work on IDAs of our group included a study of the pyrophosphate discrimination using the dinuclear zinc(II) complex of a new ligand (**L1**) containing two tripodal tetramine units linked to the anthracene scaffold [29]. The tripodal tetramine unit refers to 2-[bis(2-pyridylmethyl)aminomethyl]aniline as shown in Figure 3.4. This tripodal tetradentate ligand, consists of a tertiary N atom bonded to three arms with a pyridine donor unit on two arms and an aniline donor unit on the other. The four N-donor atoms of the ligand can coordinate strongly to a first low transition metal or lanthanide ion [73, 74].

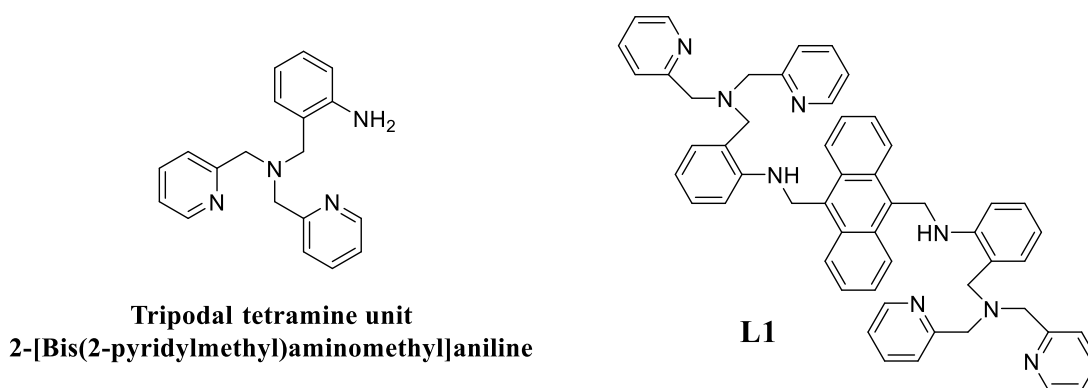


Figure 3.4 Chemical structure of 2-[bis(2-pyridylmethyl)aminomethyl]aniline (left) and **L1** (right).

Although zinc(II) complexes are most commonly employed in IDAs, the related dinuclear Cu, Ni, Rh and Fe complexes have also been reported [75-85]. In particular, copper(II) complexes have become attractive to researchers for cyanide recognition due to the high copper–cyanide affinity. For instance, Rhaman and co-workers [28] reported a macrocycle-based dinuclear copper(II) complex (**XVI**) for the determination of cyanide anions based on IDAs in the presence of external indicators. DFT calculations indicated that the cyanide anion is bridged between two copper ions of the host through strong electrostatic interactions as depicted in Figure 3.5.

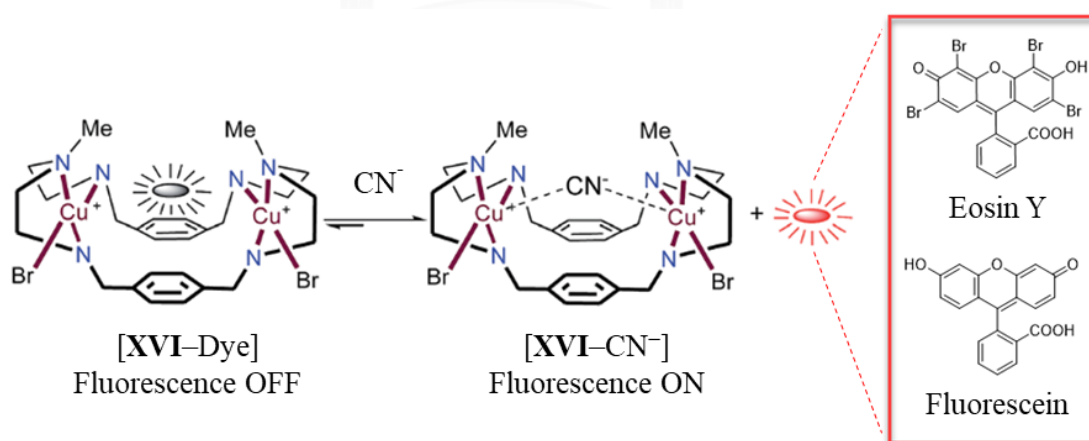


Figure 3.5 Binding mechanism for cyanide of **XVI** in the presence of external indicators, Eosin Y and Fluorescein [28].

As mentioned, numerous papers have reported various metal complexes, especially dinuclear zinc(II) complexes for determination of phosphorylated species based on IDAs. However, only a few complexes have been published for cyanide sensing. Inspired by those developments and the fact of good binding affinity of copper(II) and cyanide ions, we herein present an IDA-based colorimetric cyanide sensor using a dinuclear copper(II) complex of the ligand **L1** (the same ligand as our previous work). Among various complexometric indicators, we have focused on a pyrogallol red (**PGR**) which is known as metal sensitive indicator due to the chelation of various metal ions [86]. Moreover, previous results showed that the ensemble between this dye and $\text{Cu}_2\text{L1}$ exhibited a remarkable color change with the desired selectivity of the cyanide target. The sensing performance and the analytical application in real water samples were demonstrated in detail. Furthermore, the formation mechanism of the $\text{Cu}_2\text{L1}$ -**PGR** ensemble with cyanide were analyzed by density functional theory (DFT) calculations.

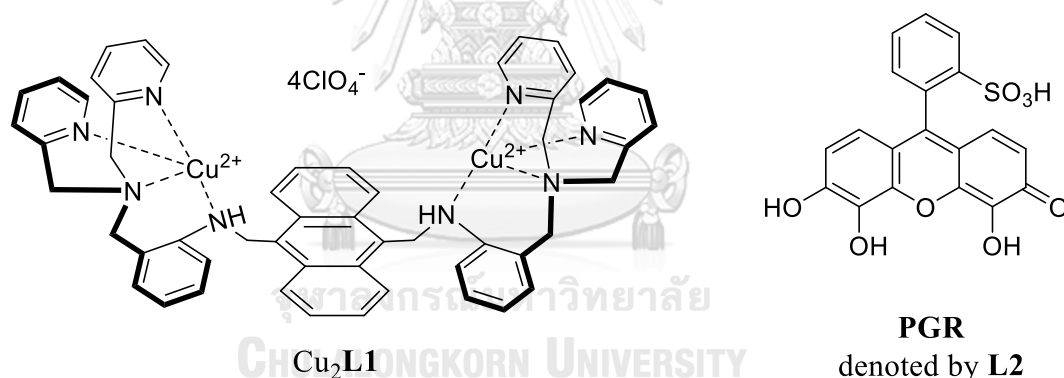


Figure 3.6 Chemical structure of a $\text{Cu}_2\text{L1}$ (left) and **PGR** indicator (right) denoted by **L2** in this work.

3.2 Results and discussion

3.2.1 Synthesis and characterization of dinuclear Cu(II) complex of anthracene based tripodal tetramine ($\text{Cu}_2\text{L1}$)

The synthetic overview of $\text{Cu}_2\text{L1}$ is illustrated in Figure 3.7. Ligand **L1** was first synthesized by minor modification of previous published procedures [29] which involved Schiff base condensation and reductive amination as main reactions. ^1H NMR resonances (Figure 3.8) confirmed the formation of the ligand, where related resonances are all present in their expected integral ratios.

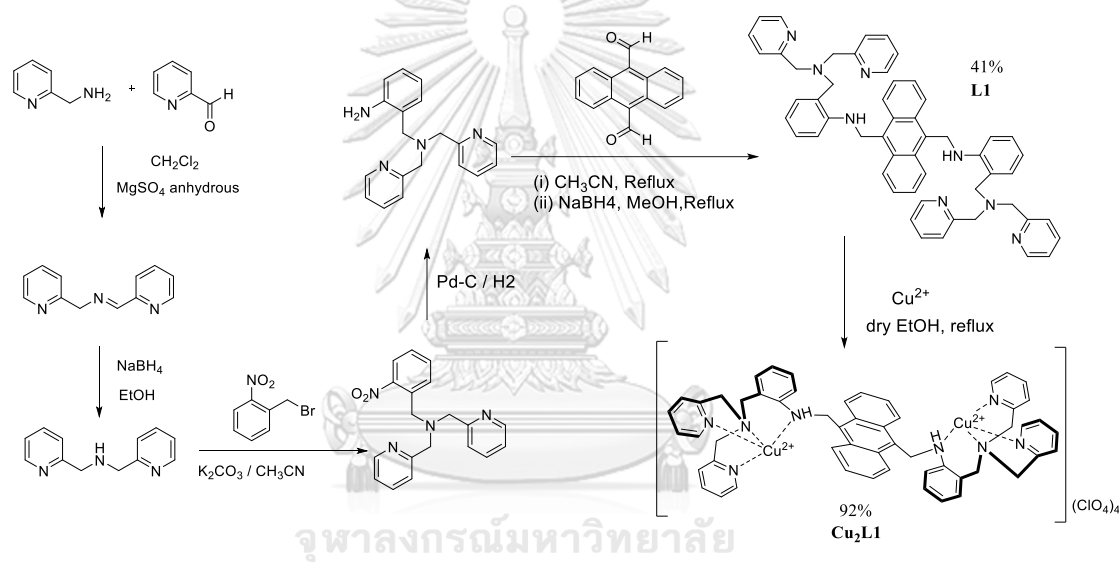


Figure 3.7 The synthetic overview of $\text{Cu}_2\text{L1}$.

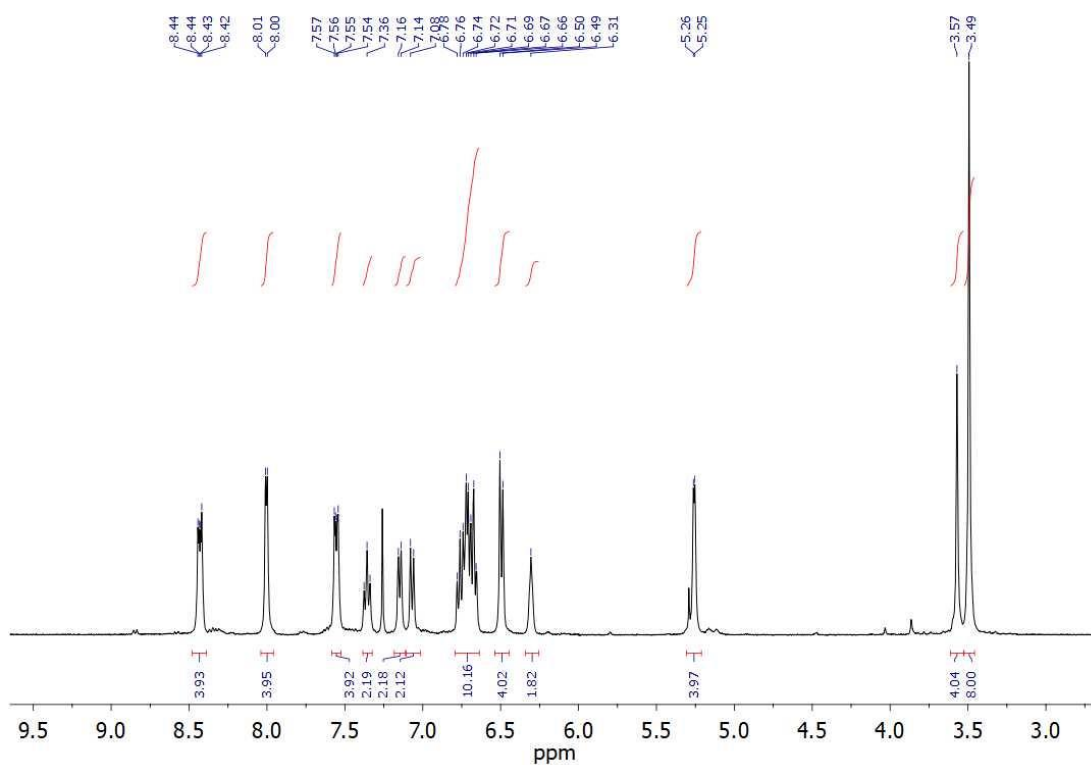


Figure 3.8 ^1H NMR (400 MHz, CDCl_3) spectrum of ligand **L1**.

The $\text{Cu}_2\text{L1}$ was further synthesized by the dropwise addition of the ethanolic solution of $\text{Cu}(\text{ClO}_4)_2$ into a solution **L1** in CH_2Cl_2 and the resulting green solid was isolated by filtration. Mass spectrometry (ESI^+) revealed the molecular ion peak, $m/z = 1235.0554$ for $[\text{Cu}_2\text{L1}+3\text{ClO}_4]^+$ as depicted in Figure 3.9. Moreover, elemental analysis also agrees well with the proposed structure.

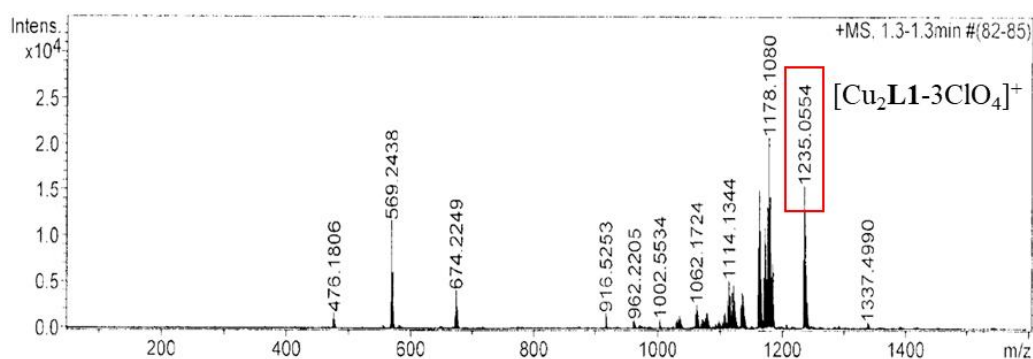


Figure 3.9 HRMS (ESI^+) of $\text{Cu}_2\text{L1}$.

3.2.2 UV-vis experiments

3.2.2.1 Studies of Cu₂L1-PGR ensembles

The UV-vis absorption is one of the most interesting output signals not only because the instrumentation is extensively available, but also because it is able to detect the target analyte with the naked eye. Initially, the absorption spectral changes of **PGR** towards Cu₂L1 were investigated through UV-vis titration experiments in 20% (v/v) water-acetonitrile solution buffered at pH 7.4 with 10 mM HEPES. As illustrated in Figure 3.10, **PGR** showed an absorption band at 420 nm and a strong broad peak at about 550 nm. Upon the addition of Cu₂L1 resulted in a bathochromic shift of the absorption at 550 nm to 573 nm and an increase in the absorption band at 380 nm. Moreover, the color changes from pink to blue were clearly observed by the naked eye when Cu₂L1 was added to the **PGR** solution. Since the addition of one equivalent of Cu₂L1 to **PGR** gave a complete changing in absorption, the Cu₂L1 and **PGR** in a 1 : 1 molar ratio were used to form the ensemble in further experiments.

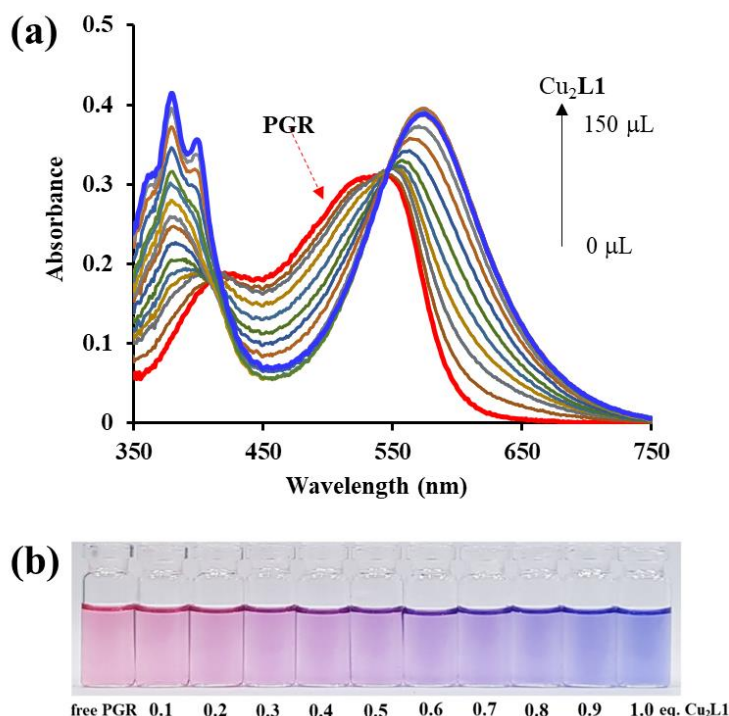


Figure 3.10 (a) Changes in absorbance, and (b) Changes in color of **PGR** obtained by the titration of Cu₂L1 (400 μM) to a solution of **PGR** (20 μM).

3.2.2.2 Studies of selectivity and cyanide sensing under IDA approach

Selectivity is an important parameter in evaluating the quality of sensors. Consequently, the selectivity ability of the $\text{Cu}_2\text{L1-PGR}$ ensemble toward various anions including F^- , Cl^- , Br^- , I^- , AcO^- , BzO^- , ClO_4^- , H_2PO_4^- , OH^- , NO_3^- , SO_4^{2-} , HPO_4^{2-} , CO_3^{2-} , SCN^- and HCO_3^- was investigated. The absorption spectra of $\text{Cu}_2\text{L1-PGR}$ ensemble in the presence of different anions are illustrated in Figure 3.11a. Addition of 7.5 equiv. of CN^- caused a dramatic decrease in absorption, whereas almost no changes could be monitored by adding of other anions. Moreover, the blue color of the ensemble solution also turned to almost colorless when cyanide was added, while a variety of other anions failed to produce a color change (Figure 3.11b). These results suggested that the $\text{Cu}_2\text{L1-PGR}$ ensemble has good selectivity for CN^- detection which can be attributed to the strong nucleophilic properties of cyanide over other ions.

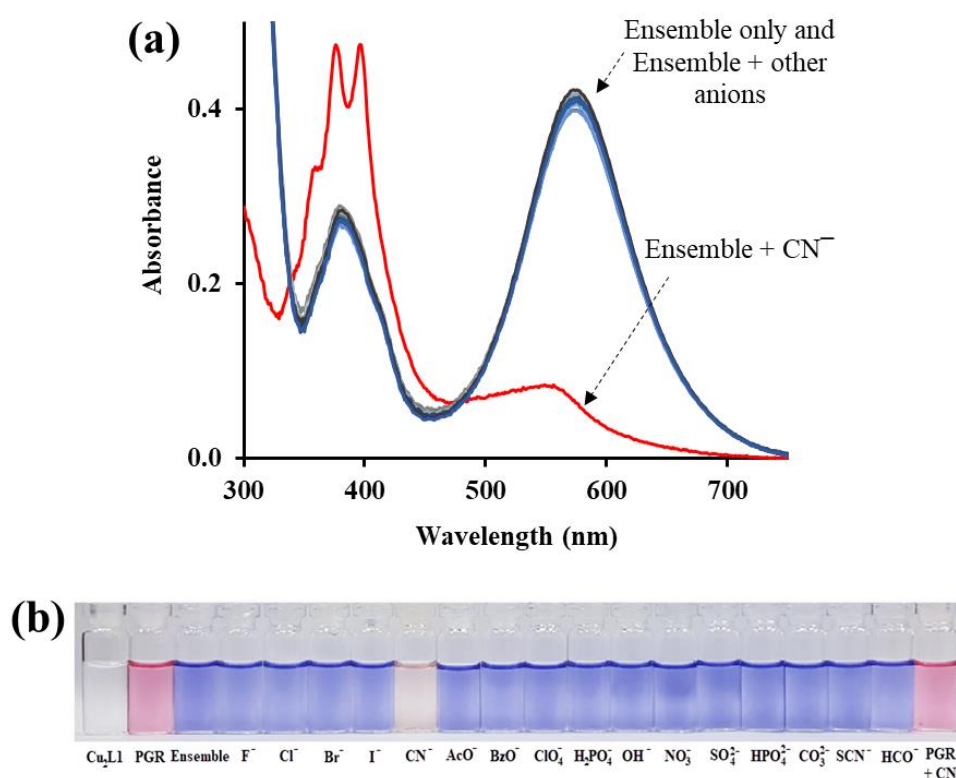


Figure 3.11 (a) Changes in absorbance, and (b) Changes in color of the $\text{Cu}_2\text{L1-PGR}$ ensemble (20 μM) in the presence of various anions (150 μM).

Next, the solution of **Cu₂L1-PGR** ensemble was titrated with various concentrations of cyanide and the results are shown in Figure 3.12. The solution of **Cu₂L1-PGR** displays an intense absorption band at 573 nm. Upon the titration of cyanide into the **Cu₂L1-PGR** solution, the absorption band of the ensemble at 573 nm decreased while the absorption band at 375 nm and 395 nm increased.

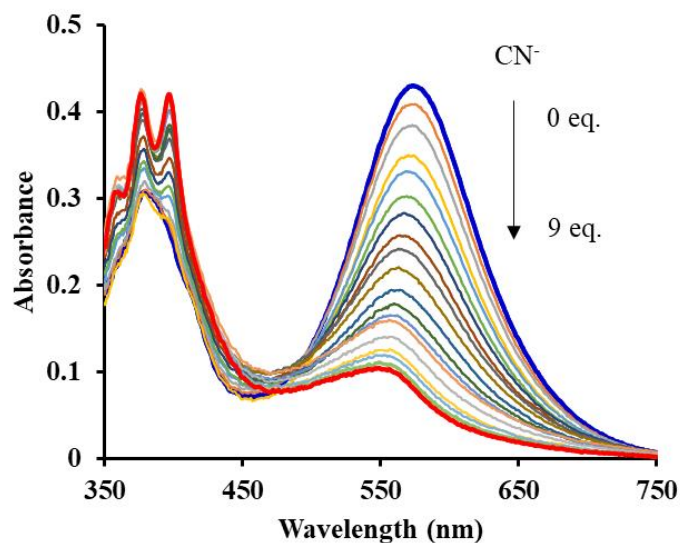


Figure 3.12 UV-vis spectra obtained for the addition of cyanide solution (1 mM) to a 1:1 ensemble solution of **Cu₂L1-PGR** (20 μ M).

Considering that, after the addition of CN^- , the color of the solution did not recover to the pink color of free **PGR**. This means that the sensing mechanism does not occur through IDAs. We envisaged that the ensemble between **Cu₂L1** and **PGR** has high stability, and therefore the added cyanide will react with **PGR** which formed ensemble with **Cu₂L1** rather than displacing it. However, the reaction of cyanide and free **PGR** did not occur supported by no observable color change of the solution upon the addition of cyanide to free **PGR** (Figure 3.11b). This implies that the formation of **Cu₂L1-PGR** ensemble will change the charge distribution of **PGR** structure, thus proving an opportunity for nucleophilic addition of cyanide to **PGR**. As a result, the conjugation in **PGR** molecule is broken, which affects the optical properties of the sensing system leading to the disappearance of the visible band of **PGR**. To corroborate this hypothesis, the theoretical calculations based on DFT were performed as described in the following computational section.

3.2.2.3 Studies of limit of detection and interferences

The analytical performance of the $\text{Cu}_2\text{L1-PGR}$ ensemble for the determination of cyanide was evaluated. Under similar conditions, a calibration curve was obtained from the plot between absorbance intensity and concentrations of cyanide anions as shown in Figure 3.13. It is noted that the $\text{Cu}_2\text{L1-PGR}$ ensemble system showed a good linear relationship in a range of 0-130 μM ($R^2 > 0.99$). The limit of detection (LOD) for this system was calculated to be 1.13 μM (0.029 ppm) according to $3\sigma/m$, where σ is standard deviation of the blank (SD, $n=10$) and m is the slope of the calibration curve. Furthermore, in comparison with some recently reported of cyanide detection, our system presented a high sensitivity and low detection limit as shown in Table 3.1.

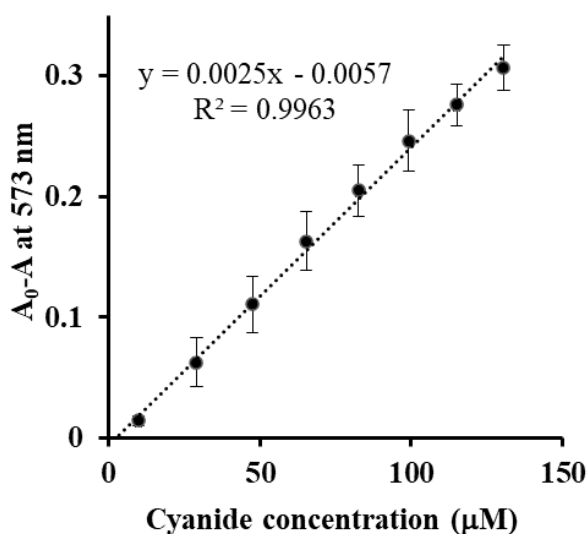


Figure 3.13 Calibration plot for detection of cyanide using $\text{Cu}_2\text{L1-PGR}$ ensemble.

Table 3.1 Comparison of some metal ensemble based chemosensors for cyanide detection.

Detection method	Probe	LOD (μM)	Linear range (μM)	Response time	Interference	Ref
Fluorometry	Pyrene based copper ensemble	1.2	0 – 20	Not reported	None	[87]
Fluorometry	Triazole based Hg^{2+} ensemble	1.25	Not reported	Few seconds	None	[88]
Fluorometry	Benzofuran-based Zn^{2+} ensemble	39	Not reported	Few seconds	H_2PO_4^-	[89]
Fluorometry	Coumarin based copper ensemble	5.77	0 – 350	Not reported	None	[90]
Fluorometry	Triphenylene based copper ensemble	5	Not reported	Not reported	None	[91]
UV-Vis	Phenanthroline-DPA based copper ensemble	3.8	Not reported	Not reported	None	[92]
UV-Vis	$\text{Cu}_2\text{L1-PGR}$ ensemble	1.13	0 – 130	Few seconds	None	This work

To further examine the practical applicability of the $\text{Cu}_2\text{L1-PGR}$ ensemble, the competitive experiments was also carried out in the presence of cyanide mixed with other anions. As depicted in Figure 3.14, the presence of an excess of other anions showed no obvious change in absorbance indicating that the $\text{Cu}_2\text{L1-PGR}$ ensemble exhibits an excellent selectivity for cyanide, and the competitive anions do not significantly interfere with cyanide sensing.

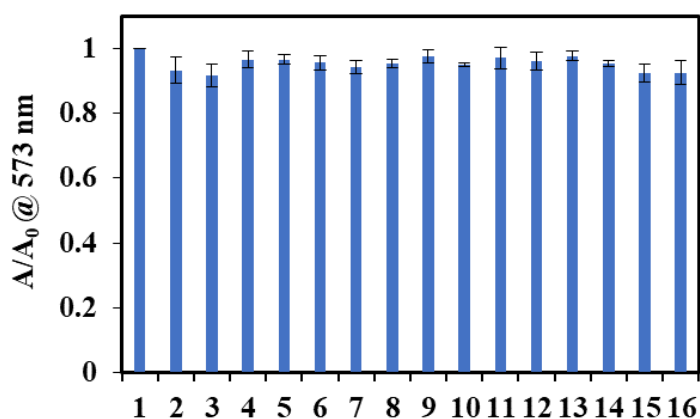


Figure 3.14 Sensing of cyanide in the presence of competitive anions (7.5 equivalents) in 20% (v/v) water-acetonitrile solution buffered at pH 7.4 with 10 mM HEPES; (1) = $\text{Cu}_2\text{L1-PGR}$ ensemble + CN^- , (2) = (1) + F^- , (3) = (1) + Cl^- , (4) = (1) + Br^- , (5) = (1) + I^- , (6) = (1) + AcO^- , (7) = (1) + BzO^- , (8) = (1) + ClO_4^- , (9) = (1) + H_2PO_4^- , (10) = (1) + OH^- , (11) = (1) + NO_3^- , (12) = (1) + SO_4^{2-} , (13) = (1) + HPO_4^{2-} , (14) = (1) + CO_3^{2-} , (15) = (1) + SCN^- and (16) = (1) + HCO_3^- .

3.2.2.4 Determination of cyanide in real water samples

Since cyanide is usually found in water or biocompatible solutions, we further studied the practical utility of our system in real water samples. We verified the sensing of cyanide in samples including drinking water, tap water, and pond water collected from Chulalongkorn university. The amount of cyanide detected was listed in Table 3.2. The assayed concentration of cyanide is in good agreement with added amount with a variation of recovery percentage in between 84 and 112. This suggested that the application of our system for quantitative analysis of cyanide levels in real water samples was quite feasible.

Table 3.2 The determination of cyanide ions in real water samples using Cu₂L1–PGR ensemble.

Sample	Added CN ⁻ (μM)	Found CN ⁻ (μM)	% Recovery	%RSD
Drinking water	0	0	-	-
	30	27.2	90.6	3.0
	50	48.2	96.3	2.3
	70	64.1	91.5	2.7
Tap water	0	0	-	-
	30	26.6	88.6	2.6
	50	45.1	90.1	1.4
	70	73.0	104.3	2.6
Pond water	0	0	-	-
	30	25.2	83.9	2.8
	50	55.9	111.8	2.7
	70	73.1	104.4	1.6

3.2.3 Theoretical calculations

To clearly demonstrate the cyanide sensing mechanisms of the Cu₂L1–PGR ensemble, theoretical calculations were performed. The feasible geometry optimizations were first carried out on free Cu₂L1, free PGR, Cu₂L1–PGR ensemble, and Cu₂L1–PGR ensemble with different cyanide binding motifs. We further investigated the absorption behavior of the Cu₂L1–PGR ensemble in sensing of cyanide *via* TD-DFT calculations. Two sets of the simulated UV-vis titration spectra were tuned based on the equilibrium at the end of the titration to obtain the existing species in the solutions. In addition, the reaction energies of all steps related with the two sets of the titration were calculated.

3.2.3.1 Geometry Optimizations

Optimized structures of Cu₂L1–PGR ensemble

The CPCM/CAM-B3LYP/6-31G(d) method was used to optimize the structures of all related compounds. The geometry optimizations of free ligand **L1**, Cu₂**L1**, and **PGR** are illustrated in Appendix 2. For Cu₂**L1**–**PGR** ensemble, there are two possible formation as follows:

(1) 1 : 1 stoichiometry between Cu₂**L1** and **PGR** in the form of

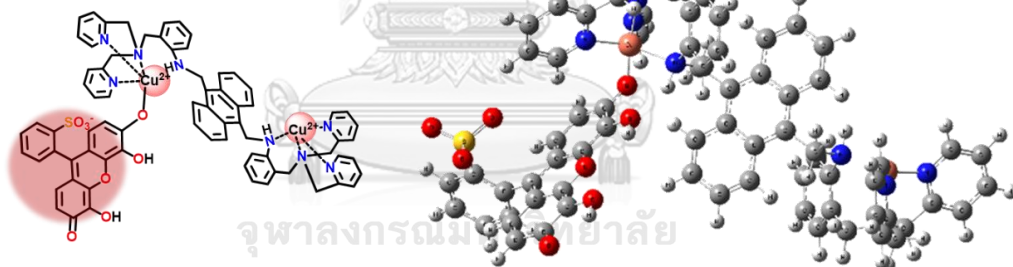


(2) 1 : 2 stoichiometry between Cu₂**L1** and **PGR** in the form of



The optimized structures of these two possible formation are presented in Figure 3.15.

(a) $[\text{CuL1Cu/L2}]^{2+}$



(b) $[\text{L2/CuL1Cu/L2}]^0$

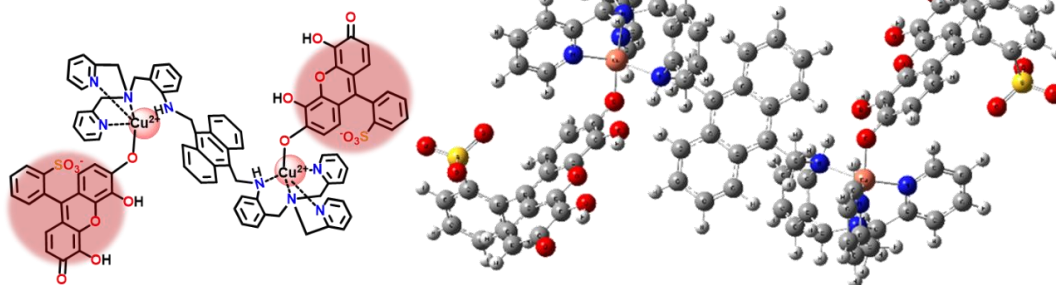


Figure 3.15 The CPCM/CAM-B3LYP/6-31G(d)-optimized structures of singlet-state complexes (a) $[\text{CuL1Cu/L2}]^{2+}$ and (b) $[\text{L2/CuL1Cu/L2}]^0$.

Optimized structures of cyanide-bound species.

For cyanide-bound species, we used both mentioned ensemble species above as initial geometries and then optimized them in the presence of cyanide. From experimental studies, the appearance of colorless solution after addition of cyanide indicated that the π -conjugation in **PGR** molecule is broken. This feature can be modulated by either the cyclization of **PGR** to form five-membered ring with two heteroatoms or the nucleophilic addition of cyanide to heterocycle of **PGR**. However, the first one does not favor in this case due to the weak nucleophilic properties of sulfonic unit and the strain geometry of the product. We therefore consider the nucleophilic addition of cyanide with three different binding modes as follows:

- (1) a single cyanide ion bound to a 1 : 1 complex ($[\text{CuL1Cu/L2/CN}]^+$)
- (2) a single cyanide ion bound to a 1 : 2 complex ($[\text{L2/CuL1Cu/L2/CN}]^-$)
- (3) two cyanide ions bound to a 1 : 2 complex ($[\text{CN/L2/CuL1Cu/L2/CN}]^{2-}$)

The optimized structures of several cyanide-bound species as mentioned are shown in Figure 3.16. The calculations revealed that the copper(II) coordinated with oxygen atom on **PGR** to form the ensemble. In the presence of cyanide, the carbon on the heterocycle of **PGR** participates in the binding.

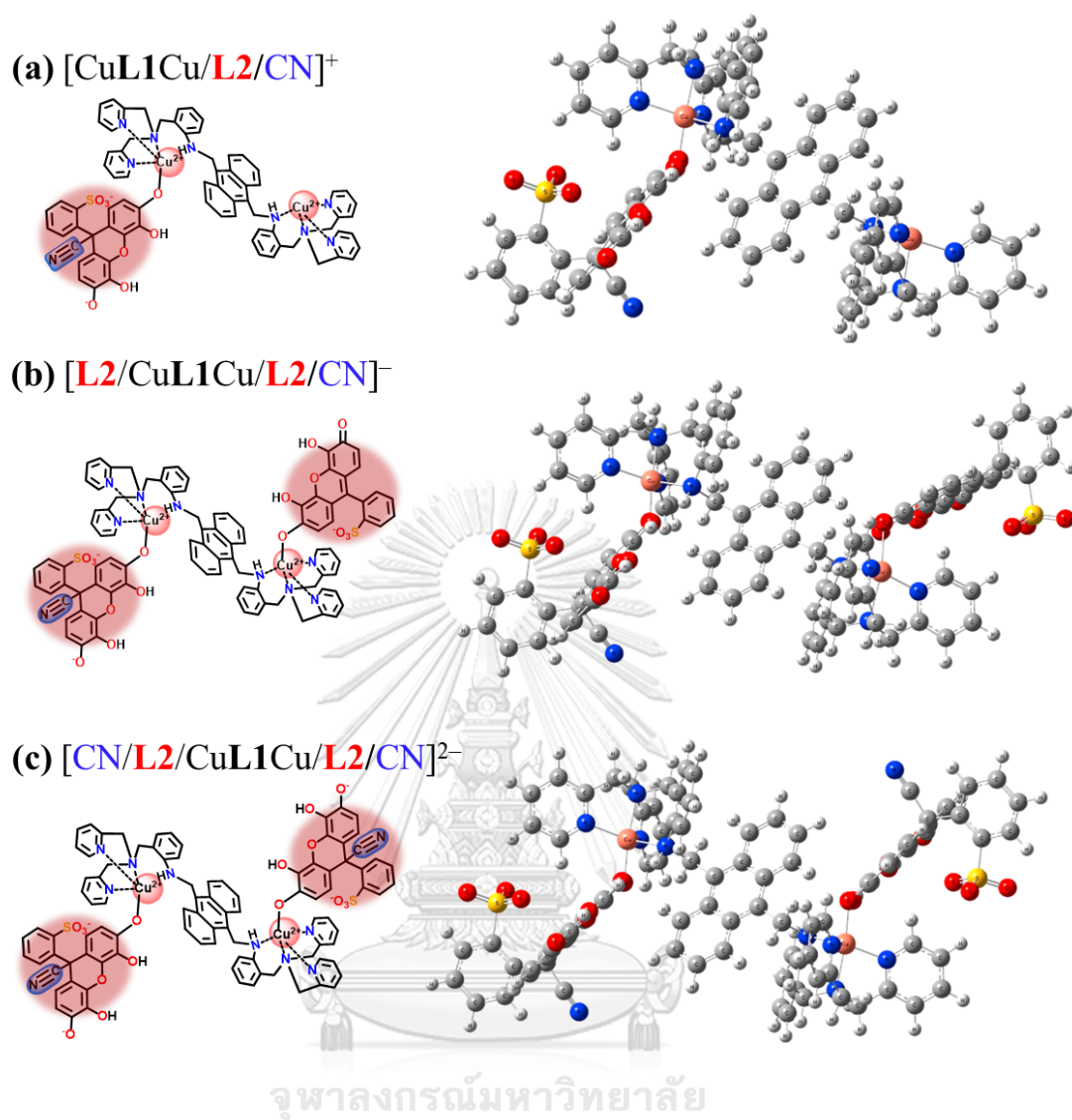


Figure 3.16 The possible structures of $[\text{CuL1Cu/L2}]^{2+}$ and $[\text{L2/CuL1Cu/L2}]^0$ complexing with cyanide ion formed as (a) $[\text{CuL1Cu/L2/CN}]^+$, (b) $[\text{L2/CuL1Cu/L2/CN}]^-$ and (c) $[\text{CN/L2/CuL1Cu/L2/CN}]^{2-}$ species, structure optimizations based on the CPCM/CAM-B3LYP/6-31G(d) computations.

3.2.3.2 UV-vis spectral analysis

The measured and simulated UV-vis spectra of all related structures

To provide a rationale for the experimentally observed spectrum behaviors, all related optimized species were performed using TD-DFT calculations. We initially investigated the absorption behavior of **PGR** in the form of $\mathbf{L2}^{2-}$ (see Appendix section for the details of different forms of **L2**). A comparison of the measured spectrum of **PGR** in 20% (v/v) water-acetonitrile as mixed solvent and the simulated $\mathbf{L2}^{2-}$ spectrum using water as solvent is presented in Figure 3.17. The simulated spectrum was obtained from the computed spectrum ($\lambda_{\max} = 458$ nm) adjusted by multiplication factor of 1.2 to easily compare between the measured and simulated spectra. The maximum absorption peak located at 550 nm matched well between the measured and simulated spectra. However, the difference of the maximum absorption peaks before adjustment was due to the solvent effects.

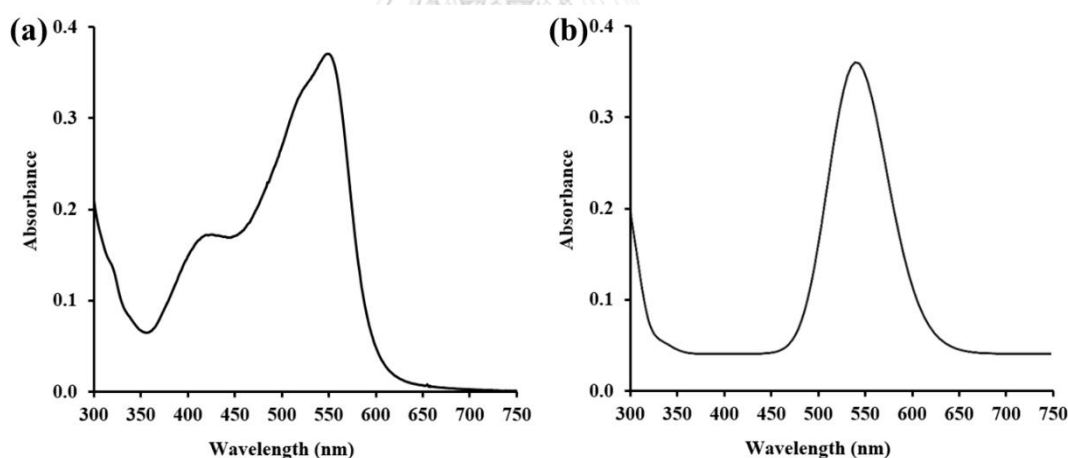


Figure 3.17 (a) The measured UV-vis spectrum of **PGR**, matched with (b) the simulated UV-vis spectrum of the $\mathbf{L2}^{2-}$ species. The simulated UV-vis wavelength is scaled by 1.20 and its absorbance is scaled to the measurement.

Further, all UV-vis spectra of related structures including $[\text{CuL1Cu}]^{4+}$, $[\text{CuL1Cu/L2}]^{2+}$, $[\text{L2/CuL1Cu/L2}]^0$, $[\text{CuL1Cu/L2/CN}]^+$, $[\text{L2/CuL1Cu/L2/CN}]^-$ and $[\text{CN/L2/CuL1Cu/L2/CN}]^{2-}$ were simulated and the results are shown in Figure 3.18 – Figure 3.20.

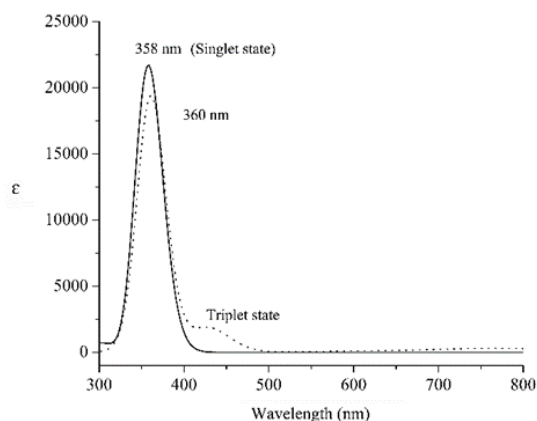


Figure 3.18 The simulated UV-vis spectra $[\text{CuL1Cu}]^{4+}$ complex. The solid and dot lines are the UV-vis spectra of their singlet and triplet states, respectively.

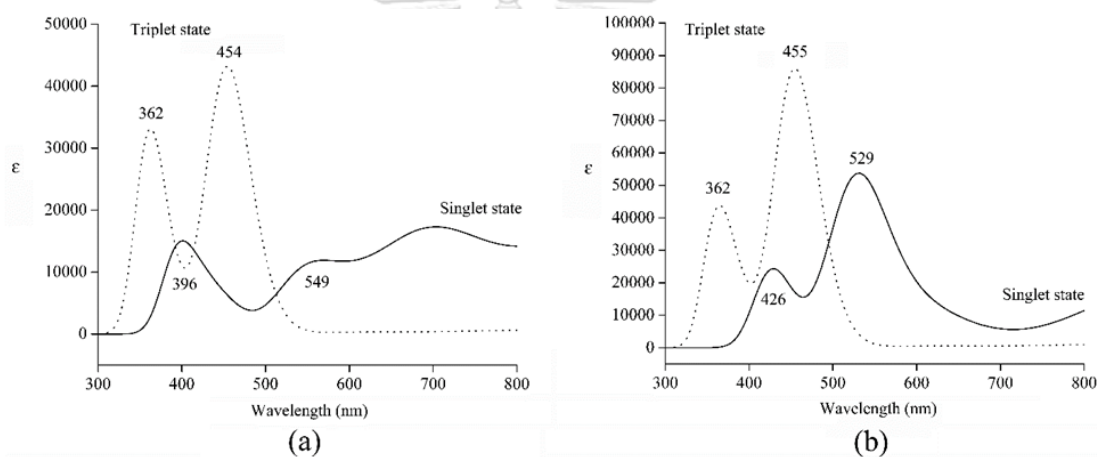


Figure 3.19 The simulated UV-vis spectra of (a) $[\text{CuL1Cu/L2}]^{2+}$ and (b) $[\text{L2/CuL1Cu/L2}]^0$ complexes. The solid and dot lines are the UV-vis spectra of their singlet and triplet states, respectively.

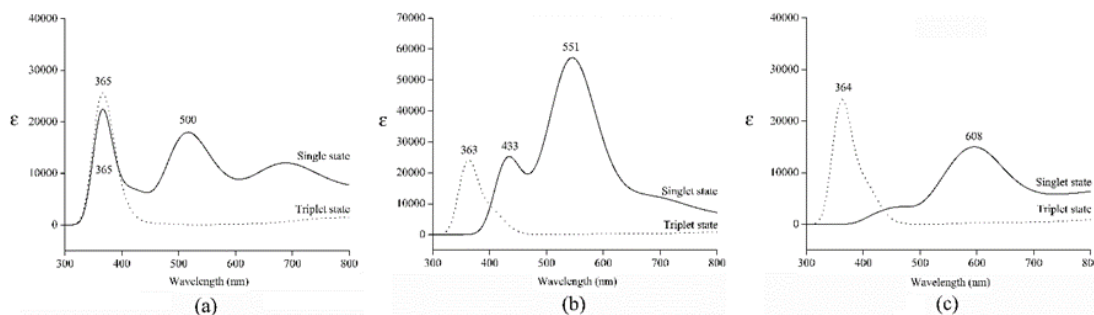
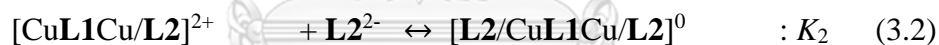


Figure 3.20 The simulated UV-vis spectra of (a) $[\text{CuL1Cu/L2/CN}]^+$, (b) $[\text{L2/CuL1Cu/L2/CN}]^-$ and (c) $[\text{CN/L2/CuL1Cu/L2/CN}]^{2-}$ complex species in aqueous solution. The solid and dot lines are the UV-vis spectra of their singlet and triplet states, respectively.

By comparing with the experimental spectra of $\text{Cu}_2\text{L1-PGR}$ ensemble (Figure 3.10) and $\text{Cu}_2\text{L1-PGR}$ ensemble in the presence of cyanide (Figure 3.11), the simulated spectra of each species did not match with the experimental spectra. It can be assigned that the experimental spectra in this case obtained from the considerable overlap of several species. Thus, the percentage of existing species involved in the equilibrium at the end of the titration was studied in the next sections.

The UV-vis titrations of L2^{2-} with CuL1Cu complex and their simulated UV-vis spectra: Set I

Considering the experimental titration of **PGR** with $\text{Cu}_2\text{L1}$ (Figure 3.10), we attempt to describe its spectrum behavior and determine the dominant species presenting in the equilibrium mixture. As previously mentioned, there are two possible formations between $\text{Cu}_2\text{L1}$ and **PGR**, 1 : 1 and 1 : 2 stoichiometry ($[\text{CuL1Cu/L2}]^{2+}$) and $[\text{L2/CuL1Cu/L2}]^0$, respectively). We conducted calculations based on the two following reversible reactions with $[\text{CuL1Cu}]^{4+} : \text{L2}^{2-}$ molar ratio of 1 : 1.



The total absorbance can be calculated according to the equation (3.3), where ϵ and C is the molar absorption coefficients and concentrations corresponding to each existing specie in solution, respectively and l is the optical path length.

$$A = (\epsilon_{[\text{CuL1Cu}]^{4+}} C_{[\text{CuL1Cu}]^{4+}} + \epsilon_{[\text{CuL1Cu/L2}]^{2+}} C_{[\text{CuL1Cu/L2}]^{2+}} + \epsilon_{[\text{L2/CuL1Cu/L2}]^0} C_{[\text{L2/CuL1Cu/L2}]^0}) l \quad (3.3)$$

Model spectrum containing overlapping spectral bands are simulated as the sum of spectra of the existing species generated from stoichiometric indices determined by equilibrium constants and concentrations of the species in the estimated model. The simulated spectrum based on the equilibrium at the end of titration of **Set I** was first examined with equilibrium constants of equation (3.1) and 3.2 (K_1 and K_2) pre-assigned to unity and the results are shown in Figure 3.21b.

Further, the pre-assigned K_1 and K_2 were adjusted to fit between the simulated and experimental data. Based on the equilibrium constants set ($K_1 = 0.02$, and $K_2 = 0.1$) as **Model I**, the simulated spectrum (Figure 3.21c) is in good agreement with the experimental spectrum (Figure 3.10), and the mixture of 52.78% $[\text{CuL1Cu}]^{4+}$, 23.61% $[\text{L2/CuL1Cu/L2}]^{2+}$ and 23.61% $[\text{L2/CuL1Cu/L2}]^0$ is supposed to be existing at the end of titration of **Set I**. The details of titration model and simulated spectra are summarized in Figure 3.21.

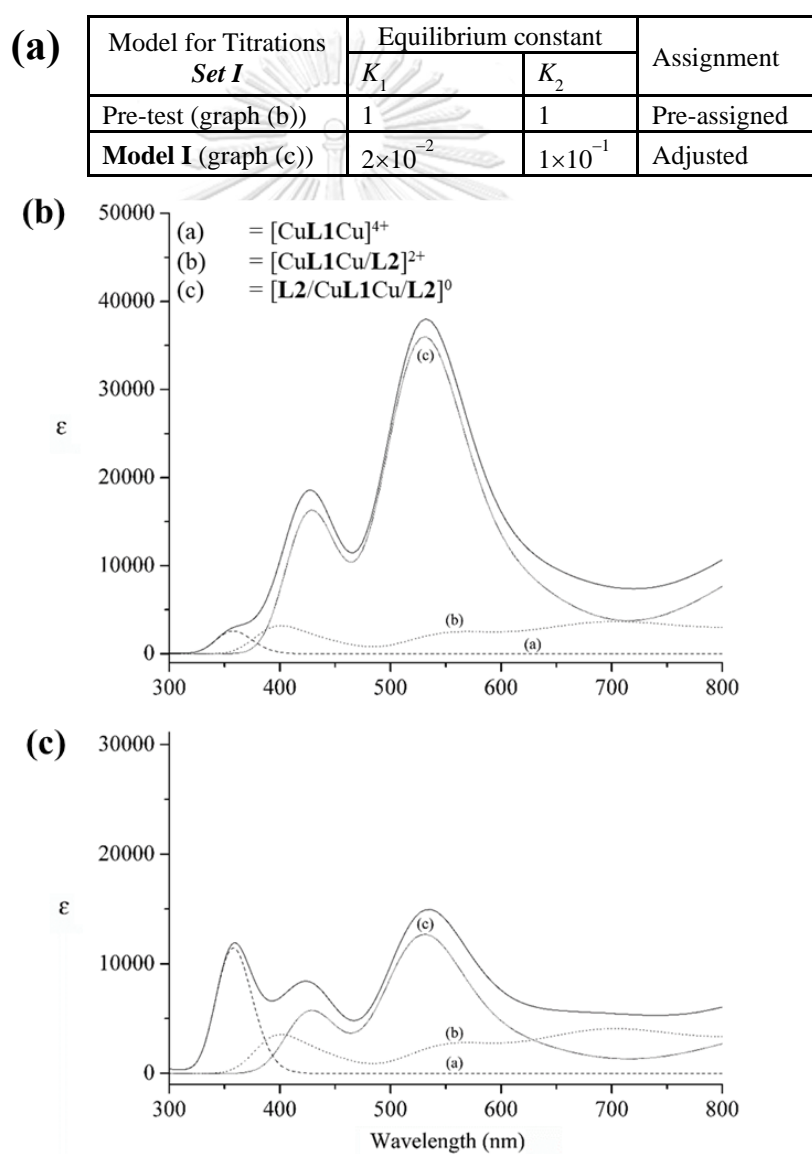


Figure 3.21 The details of titration model (a), and the simulated UV-vis spectrum (solid line) obtained by a mixture of $[\text{CuL1Cu}]^{4+}$, $[\text{CuL1Cu/L2}]^{2+}$ and $[\text{L2/CuL1Cu/L2}]^0$ where (b) K_1 and $K_2 = 1$, (c) $K_1 = 0.02$ and $K_2 = 0.1$.

Nevertheless, maximum absorption wavelengths obtained from the simulated results ($\lambda_{\max} = 360, 428$ and 532 nm) are slightly deviated from the experimental results ($\lambda_{\max} = 380, 403$ (weak absorption) and within 550 to 573). Moreover, the intensities of absorption peak at 380 nm increased when the mixture of $[\text{CuL1Cu/L2}]^{2+}$ and $[\text{L2/CuL1Cu/L2}]^0$ increased.

*The UV-vis titrations of L2^{2-} complexing with CuL1Cu by CN^- ion and their simulated UV-vis spectra: **Set II***

As mentioned before, the existing species in aqueous solution due to the L2^{2-} complexing with $[\text{CuL1Cu}]^{4+}$ are $[\text{CuL1Cu}]^{4+}$, $[\text{CuL1Cu/L2}]^{2+}$ and $[\text{L2/CuL1Cu/L2}]^0$ species. We assumed that the experimental titration curves (**Set II**) as shown in Figure 3.11 obtained from the mixed solution of $[\text{CuL1Cu}]^{4+}$, $[\text{CuL1Cu/L2}]^{2+}$ and $[\text{L2/CuL1Cu/L2}]^0$ species as the titration solution, titrated with CN^- solution. The related reversible reactions involved the existing species of the titration **Set II** depends on the following equations.



The simulated spectrum based on the equilibrium at the end of titration of **Set II** of which equilibrium constants of equation (3.4) to (3.6) (K_3 , K_4 and K_5) set was estimated by comparison with the experimental spectrum at the end of titration. All the equilibrium constants (K_1 , K_2 , K_3 , K_4 and K_5) were adjusted by tuning their order of magnitude to obtain the most matching to the experimental spectrum at the end of titration. The details of titration model and simulated spectra at the end of the titration **Set II** are summarized in Figure 3.22.

(a)

Model for Titrations <i>Set II</i>	Equilibrium constants					Assignment
	K_1	K_2	K_3	K_4	K_5	
Pre-test (graph (b))	1	1	1	1	1	Pre-assigned
Model II (graph (c))	1×10^{-3}	1×10^{-1}	1×10^{-1}	1×10^1	1×10^2	Adjusted

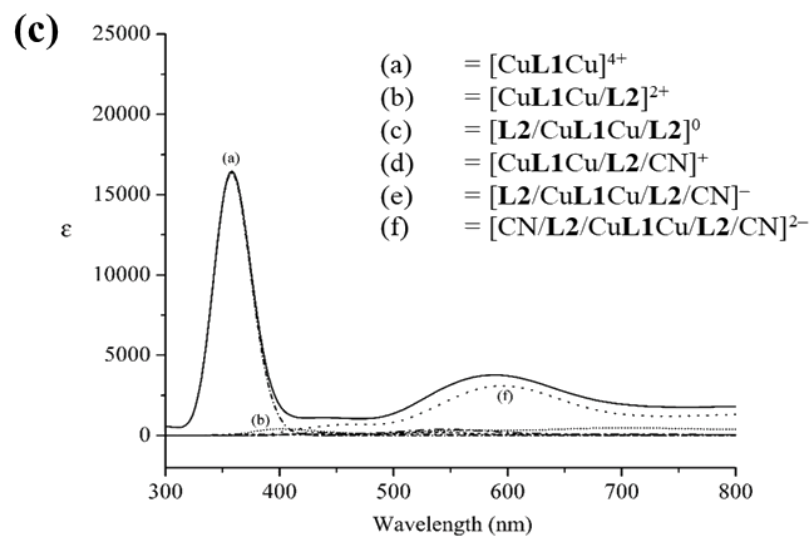
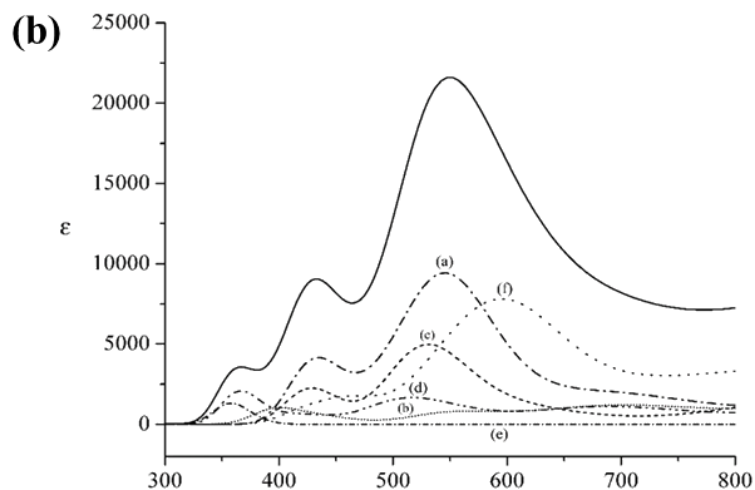


Figure 3.22 The details of titration model (a), and the simulated UV-vis spectrum (solid line) obtained by a mixture of $[\text{CuL1Cu}]^{4+}$, $[\text{CuL1Cu/L2}]^{2+}$, $[\text{L2/CuL1Cu/L2}]^0$, $[\text{CuL1Cu/L2/CN}]^+$, $[\text{L2/CuL1Cu/L2/CN}]^-$ and $[\text{CN/L2/CuL1Cu/L2/CN}]^{2-}$ where (b) K_1 , K_2 , K_3 , K_4 and $K_5 = 1$, (c) $K_1 = 1 \times 10^{-3} \text{ M}^{-1}$, $K_2 = 1 \times 10^{-1} \text{ M}^{-1}$, $K_3 = 1 \times 10^{-1} \text{ M}^{-1}$, $K_4 = 1 \times 10^1 \text{ M}^{-1}$ and $K_5 = 1 \times 10^2 \text{ M}^{-1}$.

Based on the equilibrium constants set ($K_1 = 1 \times 10^{-3} \text{ M}^{-1}$, $K_2 = 1 \times 10^{-1} \text{ M}^{-1}$, $K_3 = 1 \times 10^{-1} \text{ M}^{-1}$, $K_4 = 1 \times 10^1 \text{ M}^{-1}$ and $K_5 = 1 \times 10^2 \text{ M}^{-1}$), the mixture of 75.26% $[\text{CuL1Cu}]^{4+}$, 2.75% $[\text{CuL1Cu/L2}]^{2+}$, 0.37% $[\text{L2/CuL1Cu/L2}]^0$, 0.37% $[\text{CuL1Cu/L2/CN}]^+$, 0.65% $[\text{L2/CuL1Cu/L2/CN}]^-$ and 20.61% $[\text{CN/L2/CuL1Cu/L2/CN}]^{2-}$ is supposed to be at the end of titration of **Set II**. This indicated that the formation of the $[\text{CN/L2/CuL1Cu/L2/CN}]^{2-}$ is the most effect to amount of the titrating solution (CN^-).

3.2.3.3 Reaction energies of complex formations and all related reactions

Reaction energies of complex formations and all reactions steps occurring in two sets of titrations are listed in Table 4. Results showed that the $[\text{CN/L2/CuL1Cu/L2/CN}]^{2-}$ corresponding with the highest value of $K_5 = 1 \times 10^2 \text{ M}^{-1}$ was found to be high stable compared to those of cyanide-bound species.

Table 3.3 The reaction energies (ΔE_{react} in kcal/mol) of complex formation occurring within two sets of UV-vis titrations.

Reaction	Equilibrium constant	ΔE_{react}
<i>[CuL1Cu]⁴⁺ formation:</i>		
$\text{L1}^0(\text{free}) \rightarrow \text{L1}^0(\text{complex})$	–	37.24
$\text{L1}^0(\text{complex}) + 2\text{Cu}^{2+}(\text{D}) \rightarrow [\text{CuL1Cu}]^{4+}$	–	–385.27
$\text{L1}^0(\text{free}) + 2\text{Cu}^{2+}(\text{D}) \rightarrow [\text{CuL1Cu}]^{4+}$	–	–348.04
<i>[CuL1Cu]⁴⁺ vs L2 titration:</i>		
$[\text{CuL1Cu}]^{4+} + \text{L2}^{2-} \rightarrow [\text{CuL1Cu/L2}]^{2+}$	K_1	–77.96
$[\text{CuL1Cu/L2}]^{2+} + \text{L2}^{2-} \rightarrow [\text{L2/CuL1Cu/L2}]^0$	K_2	–13.07
<i>L2 complexes with [CuL1Cu]⁴⁺ vs CN⁻ titration:</i>		
$[\text{CuL1Cu/L2}]^{2+} + \text{CN}^- \rightarrow [\text{CuL1Cu/L2/CN}]^+$	K_3	–63.60
$[\text{L2/CuL1Cu/L2}]^0 + \text{CN}^- \rightarrow [\text{L2/CuL1Cu/L2/CN}]^-$	K_4	–19.86
$[\text{L2/CuL1Cu/L2/CN}]^- + \text{CN}^- \rightarrow [\text{CN/L2/CuL1Cu/L2/CN}]^{2-}$	K_5	–83.87

3.2.4 Proposed mechanism

According to the experimental studies, we proposed the reaction mechanism of $\text{Cu}_2\text{L1-PGR}$ ensemble *via* nucleophilic addition of cyanide on **PGR** unit. From theoretical calculations, the charge density on atoms suggested that the carbon atom on the heterocycle of **PGR** has the electrophilic character that could undergo nucleophilic attack of cyanide. This would interrupt the electronic delocalization resulting in the disappearance of the visible band of the $\text{Cu}_2\text{L1-PGR}$ ensemble as observed in the UV-vis titrations. The theoretical results are consistent with the experimental phenomena. In addition, the high stability of $[\text{CN/L2/CuL1Cu/L2/CN}]^{2-}$ was found to be dominant species of the UV-vis titrations. As shown in Figure 3.23, the binding mode of this specie is composed of two cyanide ions, each bound to a separate **PGR** which is ensembled with copper ion of the dinuclear complex. Considering the above evidences, we can suggest that the cyanide sensing mechanism of this system arises from the nucleophilic addition of cyanide to the heterocycle of **PGR** which formed the ensemble with $\text{Cu}_2\text{L1}$.

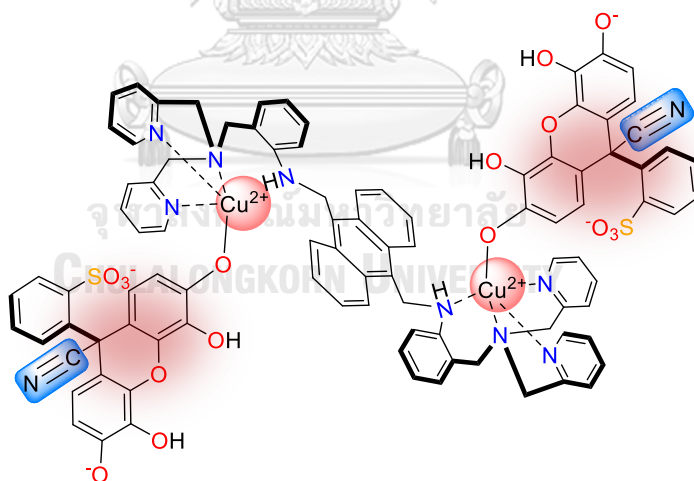


Figure 3.23 The cyanide-bound dominant species in $\text{Cu}_2\text{L1-PGR}$ system depicted from the computational calculation results.

3.3 Conclusion

In summary, we have reported a unique system that is capable of colorimetric detection of cyanide using the ensemble between the dinuclear Cu(II) complex of anthracene based tripodal tetramine ($\text{Cu}_2\text{L1}$) and pyrogallol red. In most ensemble systems, any binding would produce indicator displacement whereas the mechanism of the response to cyanide in this work is different. The sensing mechanism of this system is based on the nucleophilic addition of cyanide to the electron deficient heterocycle of **PGR** in which $\text{Cu}_2\text{L1}$ plays an important role in the induction of its charge density. UV-vis titration experiments together with DFT calculations provide insights into the binding of cyanide to the ensemble. The results suggested that the formation of the $[\text{CN}/\text{L2}/\text{CuL1Cu}/\text{L2}/\text{CN}]^{2-}$ is the most effect to amount of the titrating solution. Furthermore, this system could be used to detect cyanide selectively even in the presence of a strong competitive anions. The detection limit was calculated to be 0.029 ppm which was satisfactory for monitoring cyanide levels in physiological and environmental systems.

3.4 Experimental section

3.4.1 General considerations

All commercially available reagents (analytical grade) were used as received without further purification. All aqueous solutions were prepared with Milli-Q water provided by ultra-pure water system. In the titration experiments, all solvents as high purity grade were used, and all anions (F^- , Cl^- , Br^- , I^- , CN^- , AcO^- , BzO^- , ClO_4^- , H_2PO_4^- , OH^- , NO_3^- , SO_4^{2-} , HPO_4^{2-} , CO_3^{2-} , SCN^- , and HCO_3^-) were added in the form of tetrabutyl ammonium (TBA) salts. NMR spectra were recorded on a Varian Mercury (400 MHz) spectrometer at room temperature. Chemical shifts are given in ppm and are referenced to residual ^1H or ^{13}C solvent signals. UV-vis absorption spectra were recorded at ambient temperature using a Varian Cary 50 UV-vis spectrophotometer, with a quartz cuvette (path length 1 cm).

3.4.2 Synthesis of Cu₂L1

Ligand **L1** was synthesized according to our previously published literature [29]. A methanolic solution of Cu(ClO₄)₂·6H₂O (182 mg, 0.50 mmol) was added dropwise to a stirred solution of **L1** (101 mg, 0.13 mmol) in CH₂Cl₂. After stirring for two hours at room temperature, the resulting solids were filtered off and washed with CH₂Cl₂ and MeOH to obtain Cu₂L1 (155 mg, 0.12 mmol) as green precipitates with a 92% yield. HRMS (ESI⁺) for [Cu₂L1 + 3ClO₄⁻]⁺, the fragmentation at m/z = 1235.0554 was confirmed.

3.4.3 Colorimetric and UV-vis experiments

All experiments were performed in 20% (v/v) water-acetonitrile solution buffered with HEPES (10 mM). Physiological pH value of 7.4 was chosen as detection conditions.

Screening tests for the selective cyanide sensing. To prepare the Cu₂L1–**PGR** ensemble, a solution of **PGR** indicator (200 μL, 4.0 × 10⁻⁴ M) was added into a solution of Cu₂L1 (2.0 mL, 2.0 × 10⁻⁵ M). Subsequently, A solution of tetrabutylammonium salt of each anion (300 μL, 1.0 × 10⁻³ M) was added to the as-prepared ensemble. The resulting mixtures were allowed to stand still for 2 min and then subjected to UV-vis spectroscopic measurements. Photographs were taken using a smartphone camera.

Titration of PGR with Cu₂L1. A solution of **PGR** (2.0 mL, 2.0 × 10⁻⁵ M) was titrated with 10 μL aliquots of Cu₂L1 solution (4.0 × 10⁻⁴ M). After each addition, the resulting mixtures were stirred for 2 min and then subjected to UV-vis spectroscopic measurements.

Titration of Cu₂L1-PGR ensemble with cyanide. A 1 : 1 ensemble solution of Cu₂L1–**PGR** (2.0 mL, 2.0 × 10⁻⁵ M) was titrated with 10 μL aliquots of tetrabutylammonium cyanide solution (TBACN, 4.0 × 10⁻⁴ M). After each addition, the resulting mixtures were stirred for 2 min and then subjected to UV-vis spectroscopic measurements.

Selectivity of the sensing system. A 300 μL of each anion solution (7.5 equiv., 1.0×10^{-3} M) was added into the 1 : 1 ensemble solution of $\text{Cu}_2\text{L1-PGR}$ (2.0 mL, 2.0×10^{-5} M). After stirring for 2 min, UV-vis spectra were taken at room temperature.

Competition of $\text{Cu}_2\text{L1-PGR}$ ensemble toward various anions. A 100 μL of TBACN solution (2.5 equiv., 1.0×10^{-3} M) was added into the 1 : 1 ensemble solution of $\text{Cu}_2\text{L1-PGR}$ (2.0 mL, 2.0×10^{-5} M). Then, 300 μL of each anion solution (7.5 equiv., 1.0×10^{-3} M) was added into the mixed solution. After stirring for 2 min, UV-vis spectra were taken at room temperature.

Cyanide detection in real water samples. Commercially available drinking water was purchased from the local market. Tap water and pond water samples were collected from the laboratory and our university, respectively. All samples were kept at room temperature for a period of not more than 24 h prior to analysis. Then, the top layer of them was filtrated through 0.45 μm filters for removing suspended material. For the analysis of water samples, suitable aliquot of standard stock solution of potassium cyanide was added to 10 mL of water samples. Recovery experiments were carried out by spiking the samples (200 μL) to our system at three concentrations of cyanide, namely 30, 50 and 70 μM . The experiment was repeated 3 times with each sample.

3.4.4 Theoretical CHULALONGKORN UNIVERSITY

3.4.4.1 Structure optimizations of all studied species

The structure optimizations of anthracene based tripodal tetramine compound (ligand **L1**), dinuclear Cu(II) complexes in forms of $[\text{CuL1Cu}]^{4+}$, $[\text{CuL1Cu}]^{4+}$, their complexes with pyrogallol red (**PGR**, denoted by **L2** compound which is present as L2^{2-} species, see later section) i.e. $[\text{CuL1Cu/L2}]^{2+}$, $[\text{L2/CuL1Cu/L2}]^0$, their complexes with cyanide ion and all related species were carried out using the CAM-B3LYP/6-31G(d) level of theory [93-95] in combination with polarizable continuum model (PCM) [96-98] and solvent effect model. The conductor-like polarizable continuum model (CPCM) of water ($\epsilon = 78.3553$) with the non-electrostatic terms and

UFF atomic radii for the solvation cavity were detailed for the solvent effect task. All density functional theory (DFT) calculations with solvent effect model were performed using the Gaussian 09 program package [99]. The Natural bond orbital (NBO) analysis on the optimized molecular structures using the NBO 3.1 program integrated within the Gaussian 09 program package [99] was also performed at the CPCM/CAM-B3LYP/6-31G(d) level of theory.

3.4.4.2 UV-vis simulations of all studied species

The UV-vis spectroscopic data for each species were obtained from electron-transition excitation computations [100] using the time-dependent DFT approach with the PCM solvation (PCM/TD-DFT) at the CPCM/TD/CAM-B3LYP/6-31G(d) level of theory with solvent effect (water) model. Vertical excitation energies were computed for the first 25 singlet and triplet excited states and overall transitions based on the same theory were considered. The UV-vis spectroscopic data for each species were derived from the Gaussian function and the full width at half maximum (FWHM) set to 3000 cm^{-1} as implemented in the GaussSum 3.0 program [101] using the Gaussian 09 output files. The simulated UV-vis spectra for mixtures of related species were obtained by weight average method and estimated formation constants of all related species to compare with their observed spectra.

CHAPTER IV

ALIZARIN RED S CONJUGATED BORONIC ACID ENSEMBLES FOR THE SELECTIVE DETERMINATION OF CYANIDE IN AQUEOUS MEDIA USING INDICATOR DISPLACEMENT ASSAY APPROACH

4.1 Introduction

The development of new strategies for determination of cyanide ions has gained much importance due to the roles of them in human health and environmental processes. Among the powerful tools for cyanide detection, colorimetric and fluorometric molecular sensors have received much attention due to their simplicity, low cost, and rapid measurement and many synthetic receptors have been reported so far [102-104].

To date, synthetic receptors with different functional groups, such as thiourea, dicyano-vinyl, hydrazone, and Schiff base derivatives [105], have been developed for the selective recognition of cyanide. Among them, boronic acid derivatives (**BAs**) have attracted considerable interest from researchers due to the strong nucleophilic addition of cyanide to boronic acid group [106-108]. In boronic acid-based sensors as shown in Figure 4.1, the boronic acid group $R-B(OH)_2$ serve as Lewis acids that react with nucleophilic cyanide ions leading to the formation of tricyano borate $R-B^-(CN)_3$. As a result, optical changes can be observed due to the perturbation of the charge transfer nature of the excited state[109]. Examples of such boronic acid-based cyanide sensors include pyridinium [110] and naphthoquinone imidazole [111] boronic acid derivatives, compound **XVII** and **XVIII**, respectively, as shown in Figure 4.2.

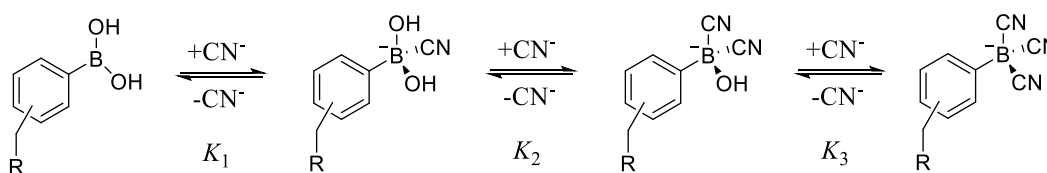


Figure 4.1 Equilibrium involved in the interaction between the boronic acid group and cyanide[109].

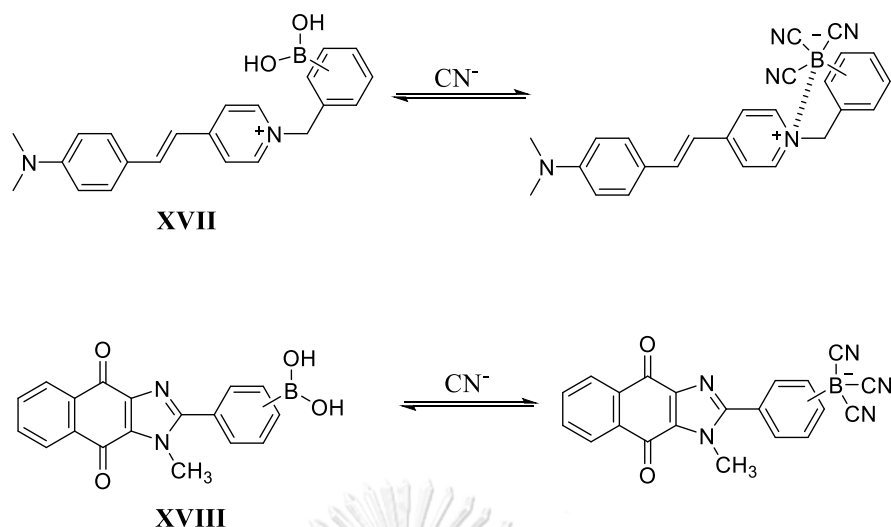


Figure 4.2 Cyanide addition to compound **XVII** and **XVIII** [110, 111].

However, most of the synthetic receptors have restricted by some of their own disadvantages such as complicated synthesis of the molecules and poor solubility in aqueous systems. Thus, finding a simple system for detection of cyanide in aqueous media is still a great challenge.

Indicator Displacement Assay (IDA) is an alternative approach that can meet the demand for quick analysis in aqueous solutions [112]. This assay is used to convert synthetic receptors into sensors without requiring the covalent connection of a reporter moiety [113]. With this system, a receptor is pre-equilibrated with an indicator, which matches the recognition site of the receptor. The addition of a competitive analyte results in the displacement of the indicator from the receptor, leading to a detectable signal change [114]. Owing to its visual responses and easy operation, this approach has been employed by many research groups [115, 116].

Recently, IDAs using **BAs** in combination with diol-containing dye have been developed for the detection of various analytes in aqueous solutions [86, 117, 118]. For example, Minami and co-workers have reported systems featuring catechol dyes (alizarin red S, bromopyrogallol red and pyrogallol red) ensembled with 3-nitrophenylboronic acid (**NPBA**) capable of detecting of metal ions under competitive conditions (Figure 4.3). This self-assembly colorimetric sensor is fast, simple and easy-to-handle.

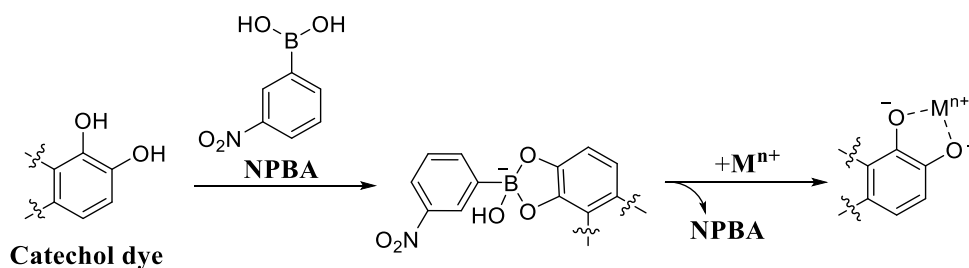


Figure 4.3 The self-assembled chemosensor utilizing the building blocks (a catechol dye and NPBA) for the easy-to-prepare colorimetric assay.

Among various catechol dyes, alizarin red S (**ARS**) is of remarkable interest due to its interesting fluorescent property. **ARS**, a commercially available 1,2-diol containing dye with a planar heterocyclic ring structure (Figure 4.4), is nearly nonfluorescent owing to the excited state intramolecular proton transfer (ESIPT) from the phenol hydroxyl group of **ARS** to the ketone oxygen resulting in the fluorescence quenching of free **ARS** [119]. Upon complexed with **BAs**, it shows a dramatic increase in fluorescence intensity in aqueous solutions at nearly physiological pH [120-122]. Moreover, it should be noted that **ARS** has reasonable water solubility, up to 10^{-3} M [123]. In this regard, **ARS** has been adopted as an indicator in competitive binding assays in aqueous systems for many sensing applications [123-125].

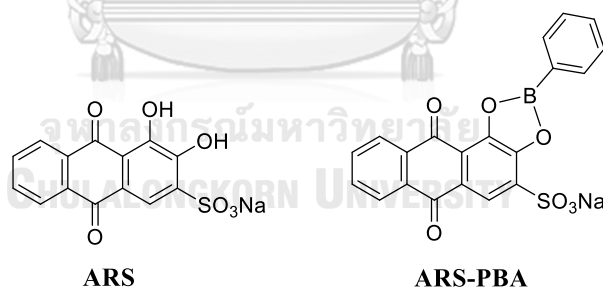


Figure 4.4 Chemical structure of **ARS**, and **ARS-PBA**.

Since **ARS** has a coordination site for metal ions, it is possible to develop a sensor for metal ions using the reversible linkage of **ARS-PBA** ensemble (**PBA** refers to phenylboronic acid). Kubo and co-workers have shown that the **ARS-PBA** ensemble can be used as a fluorescent sensor for detection of Cu^{2+} [126]. Furthermore, many groups have attempted to use the ensemble between **ARS** and **PBA** derivatives for the detection of various analytes such as saccharides [127, 128], reactive oxygen species [31, 122, 129] and anions [130].

For instance, Arimori and co-workers developed the displacement system for detection of D-glucose. The **ARS-PBA** ensemble displayed an enhanced response to D-glucose when compared to simple phenylboronic acid (**PBA**) [131]. Lampard and co-workers achieved determination of fructose using hydrogels of **ARS-BA**. The sensing of fructose in this system occurred through the release of **ARS** from the ensemble, providing an optical change in solution as depicted in [132] (Figure 4.5).

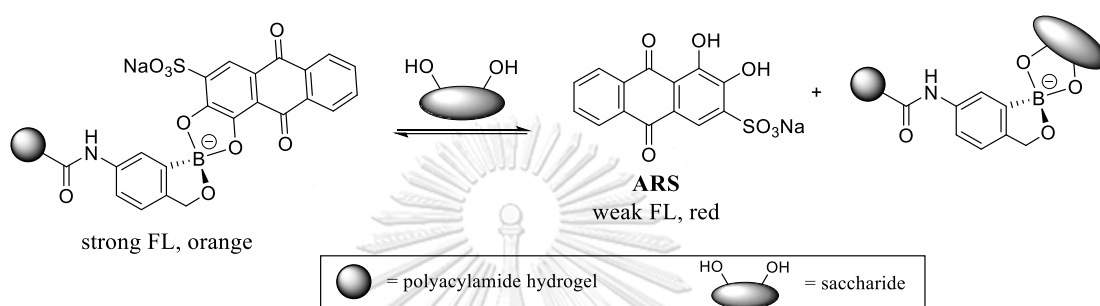


Figure 4.5 Dye displacement assay utilizing an **ARS**-bound hydrogel for fructose detection [132].

Another example is involved in the reactive oxygen species (ROS) detection reported by Sun and co-workers [129]. In this case, **ARS-PBA** complex assembled with the assistance of surfactant has been employed for H_2O_2 sensing. The use of CTAB assemblies brings many advantages, including enhanced quantum yield, stability and solubility in aqueous solution. The oxidation between boronic ester and H_2O_2 leads to the release of **ARS** and generation of phenol as shown in Figure 4.6.

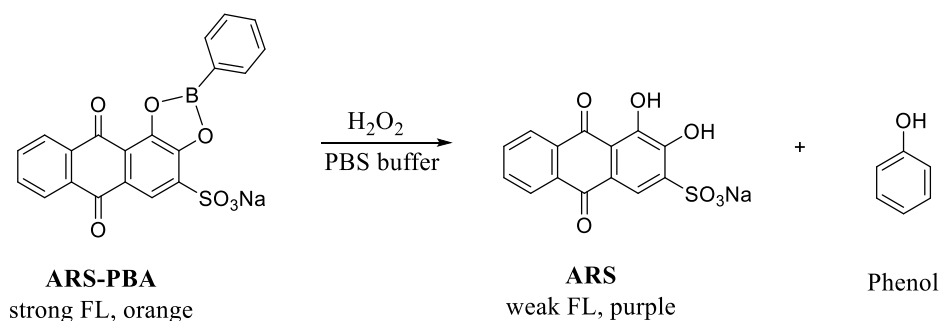


Figure 4.6 **ARS-PBA** ensemble for the detection of H_2O_2 in neutral aqueous buffer with added CTAB [129].

In addition to serving as sensors for metal ions, saccharides and ROS, **ARS-PBA** ensemble can be used as chemical probes for anions based on Lewis acid-base interactions. Kubo and co-workers have found that anion-induced **ARS-PBA** association gave a specific and sensitive response towards fluoride and acetate anions and the order of the sensitivity was related to the basicity of the added anions [126, 130].

According to previous literature, it occurred to us that the **ARS-BAs** ensemble for cyanide detection have not been reported. In view of the need for cyanide detection exclusively in water, our attention focused on a simple *in situ* formed **ARS-BAs** which can rapidly sense cyanide with specific selectivity. We selected **ARS** and phenylboronic acid derivatives (**PBA**, **APBA**, **NPBA** and **MNPBA**) which are commercially available for the construction of an IDA. The sensing of cyanide occurs through a “turn-off” fluorescent strategy by just taking the advantage of the unique cyanide-boron interaction. When CN^- is added to the **ARS-BAs** ensemble, **ARS** molecules are displaced by the formation of tricyano borate. Since the **ARS** displays characteristically different spectroscopic signatures when free or bound, the optical signal reports on the free **ARS**. The proposed mechanism for detection of cyanide based on **ARS-BAs** ensemble is shown in Figure 4.7.

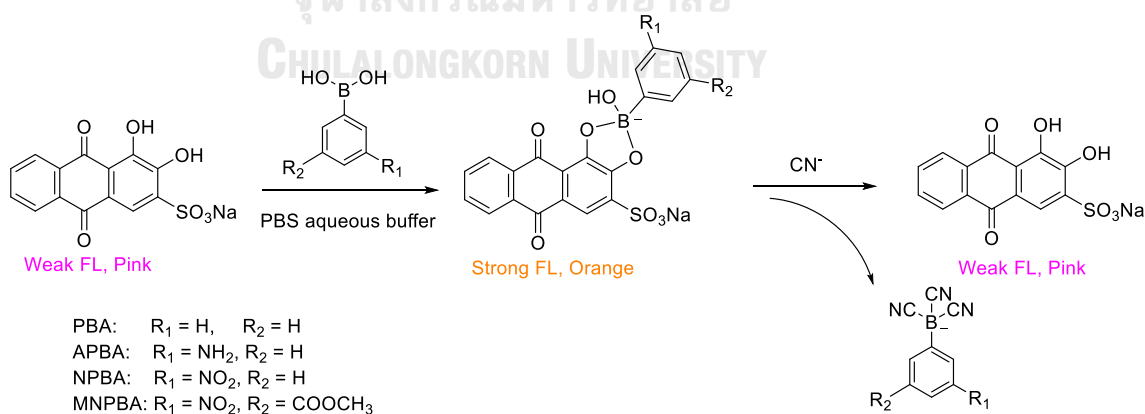


Figure 4.7 Proposed mechanism for detection of CN^- based on **ARS** and boronic acid derivatives in this work.

4.2 Results and discussion

4.2.1 Studies of absorption and emission of ARS–NPBA ensemble

Owing to its water-soluble nature of **ARS**, we started the detection in an aqueous PBS buffer. To test the feasibility of this assay method, the complexation of **ARS** and **BAs** in PBS buffer at pH 8.0 was first investigated by UV-vis and fluorescence spectroscopy. The absorption and emission spectra of **ARS** and **ARS** complexed with 3-nitrophenylboronic acid (**ARS–NPBA**) *in situ* are presented in Figure 4.8.

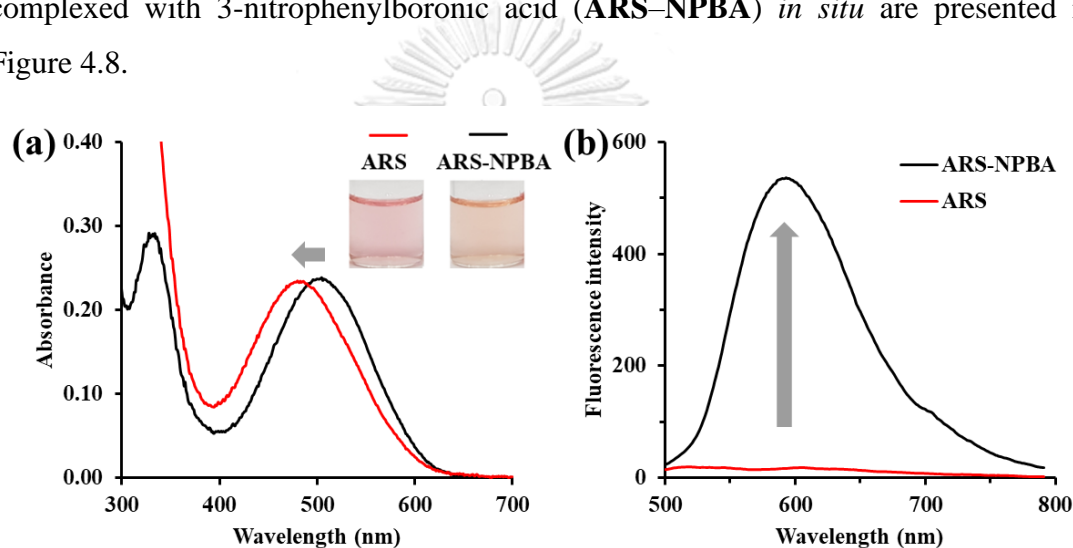


Figure 4.8 (a) Absorption and (b) emission spectra ($\lambda_{\text{ex}} = 460 \text{ nm}$) of **ARS** ($5.0 \times 10^{-5} \text{ M}$) and **ARS–NPBA** (**ARS**, $5.0 \times 10^{-5} \text{ M}$; **NPBA**, $2.0 \times 10^{-4} \text{ M}$) in 0.01 M PBS buffer at pH 8.0.

In the UV-vis spectra, the free **ARS** showed the maximum absorption centered at 500 nm. The addition of **NPBA** to **ARS** solution caused a blue shift from the maximum absorbance at 500 nm to 475 nm with an isosbestic point as can be seen from Figure 4.8a. Furthermore, a significant color change from pink to orange was observed which was attributed to the binding of **NPBA** to the catechol diol of **ARS**. The color difference can be noticed by the naked eyes.

ARS is known to be nearly nonfluorescent due to the ESIPT quenching, it is therefore reasonable to expect that boronate ester formation between **ARS** and **BAs** will increase the fluorescence of the system through the removal of the fluorescence quenching mechanism. As expected, in terms of emission spectra (Figure 4.8b), the addition of **NPBA** to the **ARS** solution led to an increase in its fluorescence emission around 595 nm, indicating that the boronate esterification between **ARS** and **NPBA** was occurred. Mass spectrometric analysis in the negative mode also supported the formation of **ARS–NPBA** ensemble which exhibited the peak at $m/z = 489.91$ (calc. = 490.00) for $[\text{C}_{20}\text{H}_{10}\text{BNNaO}_{10}\text{S}]^-$ (Appendix 3).

4.2.2 Optimization of parameters for cyanide detection

The type of boronic acids, reaction time, concentration of boronic acid (**BA**), concentration of buffer, and pH of the solution were found to affect the emission property of **ARS**. To optimize assay parameters, the fluorescence emission of **ARS–BA** and **ARS–BA** in the presence of CN^- were examined under different conditions.

4.2.2.1 Effect of type of boronic acids

Encouraged by the emission property of **ARS–NPBA**, we next investigated how this ensemble could serve as a sensor for CN^- . However, it should be noted that types of **BAs** impact the binding affinity of the **ARS–BAs** complex and the sensitivity of the sensing system. Thus, the effects of types of boronic acid on the emission intensity of **ARS** were studied. By screening several boronic acids, four derivatives with different substituents which possess different electron withdrawing abilities including phenylboronic acid (**PBA**), 3-aminophenylboronic acid (**APBA**), 3-nitrophenylboronic acid (**NPBA**), and (3-(methoxycarbonyl)-5-nitrophenyl)boronic acid (**MNPBA**) were examined. The chemical structures of these derivatives are shown in Figure 4.9.

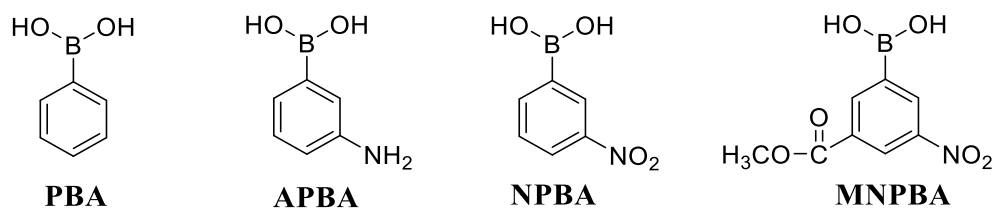


Figure 4.9 Chemical structure of phenylboronic acid derivatives employed in this study.

The fluorescence intensity of each **ARS–BA** ensemble before (F_0) and after (F) the addition of CN^- were measured and the levels of fluorescence quenching were used as a factor for choosing the best ensemble for displacement assay. The percentage of quenching is defined in equation (4.1).

$$\text{Percentage of quenching} = \frac{F_0 - F}{F_0} \times 100 \quad (4.1)$$

As can be seen in Figure 4.10, different pairs of **ARS–BAs** at the same concentration displayed different fluorescence intensities. Upon the addition of CN^- , these ensembles exhibited different quenching abilities and the sequence is **ARS–NPBA** > **ARS–MNPBA** > **ARS–PBA** > **ARS–APBA**. This result revealed that the substituted group on the phenyl ring of boronic acids plays a crucial role in the formation of the ensemble. The introduction of electron withdrawing groups such as nitro groups onto phenylboronic acids can stabilize the boronate form and lowers the $\text{p}K_a$ value which facilitate the ester formation [133].

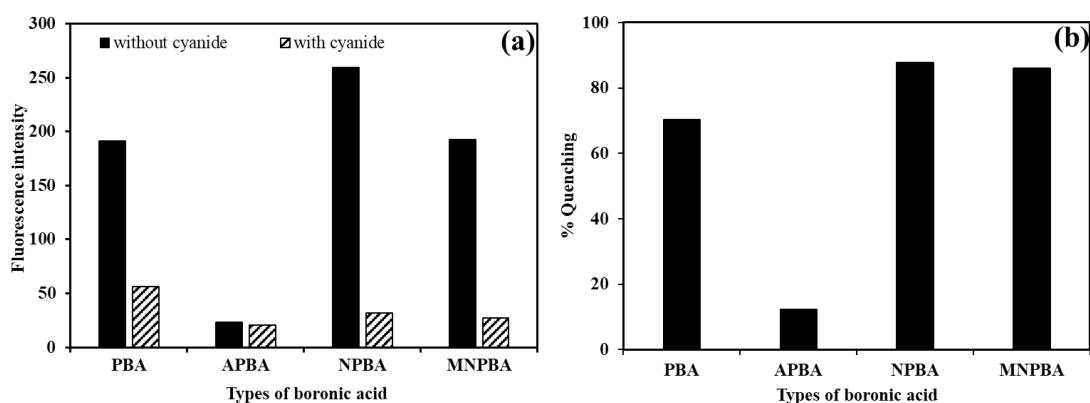


Figure 4.10 (a) The effect of boronic acid types on the fluorescence intensity of **ARS–BAs** in the absence and in the presence of KCN in 0.01 M PBS buffer at pH 8.0. (b) Fluorescence quenching of **ARS–NPBA** by 2.44×10^{-3} M (**ARS**, 5.0×10^{-5} M; **BAs**, 2.0×10^{-4} M).

Additionally, the binding affinity of **ARS–BAs** complexes was determined by monitoring the fluorescence of **ARS** at different concentrations of **BAs**. As shown in Figure 4.11, the fluorescence intensity increases with increasing the concentrations of **BAs** in all of the **BAs** tested (**PBA**, **APBA**, **NPBA** and **MNPBA**). The results were fitted based on nonlinear least-squares regression [122] and the binding constant of each **ARS–BAs** complex was then calculated. As listed in Table 4.1, the binding constant of the ensemble between **ARS** and **NPBA** is higher than those of other **BAs** examined supporting the high quenching ability reported above. Therefore, **NPBA** was chosen as a suitable boronic acid in further investigations.

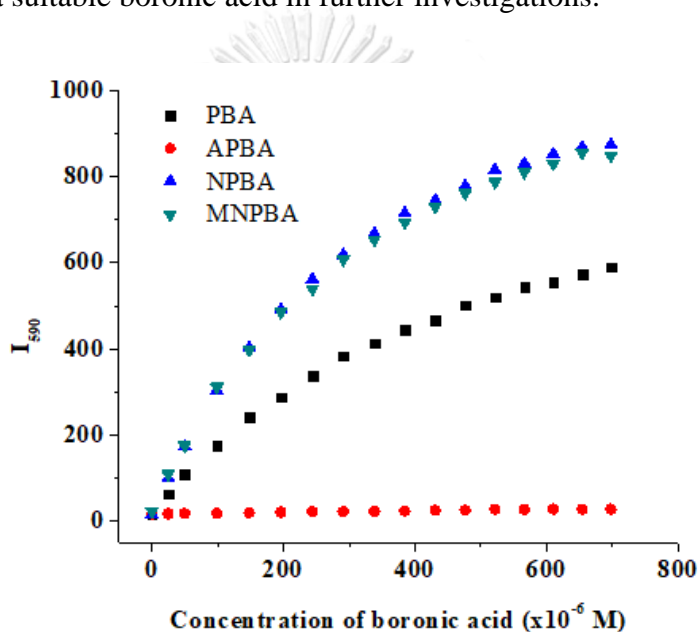


Figure 4.11 Fluorescence intensity change at 590 nm as a function of **BAs** concentration in the range of 0 – 0.7 mM ($[\text{ARS}] = 5.0 \times 10^{-5}$ M).

Table 4.1 Binding constant of **ARS** with phenylboronic acid derivatives

Boronic acid	K_a (M^{-1})
PBA	1946 ± 99
APBA	431 ± 20
NPBA	3225 ± 76
MNPBA	2947 ± 60

All studies were done in triplicate.

4.2.2.2 Effect of reaction time

The solution of **ARS-NPBA** in the absence and in the presence of CN^- were incubated at ambient temperature and the fluorescence emission was recorded every 5 min for a period of 60 min. The plot of fluorescence intensity at 590 nm versus the reaction time is presented in Figure 4.12. It was found that the fluorescence intensity in both cases became steady for a long time, indicating that our system gave a stable response which is one of the efficient chemical sensing parameters. To obtain a complete interaction, we chose reaction time of 20 min for the formation of **ARS-NPBA** ensemble.

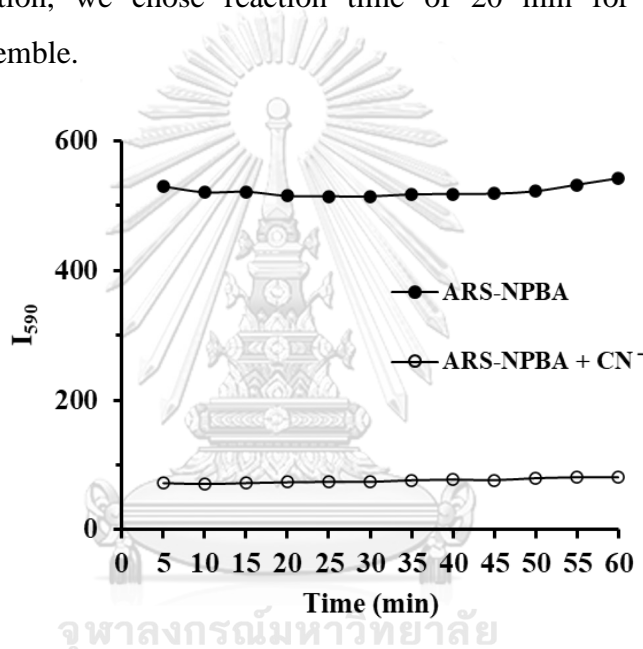


Figure 4.12 The effect of reaction time on the emission intensity at 590 nm of **ARS-NPBA** ensemble in the absence and in the presence of KCN in 0.01 M PBS buffer at pH 8.0 (**ARS**, 5.0×10^{-5} M; **NPBA**, 2.0×10^{-4} M).

4.2.2.3 Effect of NPBA concentration

The presence of **NPBA** as the recognition site in the reacting solution is the most important condition for the successful realization of this assay. Thus, the suitable concentration of **NPBA** will be a key factor to achieve the good sensitivity for CN^- detection. The effect of **NPBA** concentration was investigated by using different concentration of **NPBA** ranging from 0.5 to 4.0×10^{-4} M. Differences in fluorescence

intensity of the **ARS–NPBA** ensemble in the absence and in the presence of CN^- , and the percentage quenching are presented in Figure 4.13a and 4.11b, respectively. Considering the highest quenching ability, 2.0×10^{-4} M of **NPBA** was selected for further experiments.

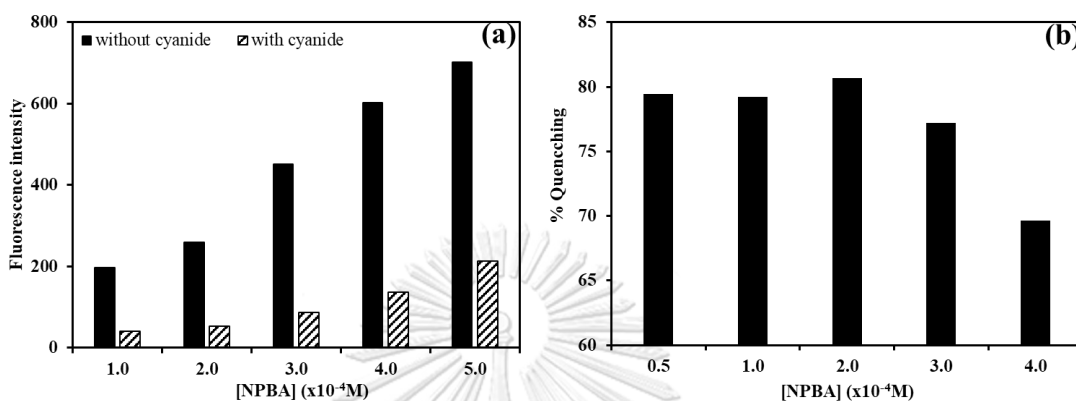


Figure 4.13 (a) The effect of **NPBA** concentrations on the fluorescence intensity of **ARS** in the absence and in the presence of KCN in 0.01 M PBS buffer at pH 8.0. (b) Fluorescence quenching of **ARS–NPBA** by 2.44×10^{-3} M CN^- (**ARS**, 5.0×10^{-5} M).

4.2.2.4 Effect of pH and concentration of buffer

The form of boronic acid (trigonal planar or tetrahedral form) is critically dependent on pH. When the solution pH is around the pK_a , boronic acids exist as the tetrahedral boronate anions that favors the binding with diols [119, 134]. Therefore, the effect of pH on the formation of the **ARS–NPBA** ensemble and the displacement ability upon the addition of CN^- was investigated. A series of pH buffer solution from 4 to 12 was tested and the pH profile is presented in Figure 4.14. The maximum difference of fluorescence intensity of **ARS–NPBA** ensemble before and after the addition of CN^- was obtained at pH 8.0, thus the solution was buffered at pH 8.0 in further studies.

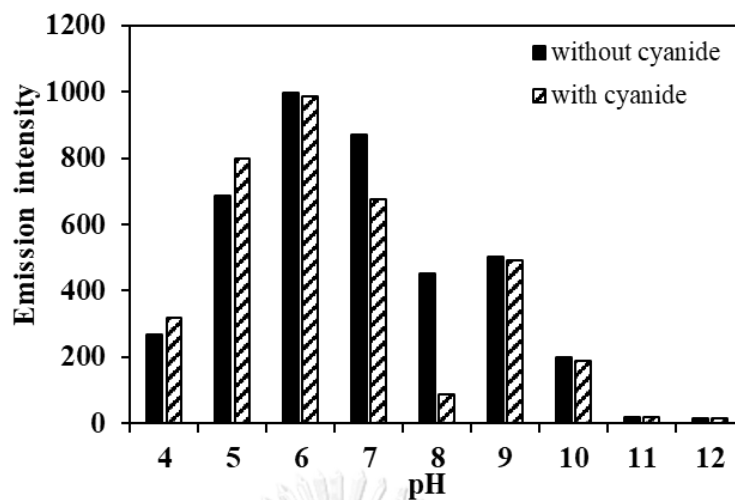


Figure 4.14 The effect of pH on the fluorescence intensity of ARS in the absence and in the presence of 2.44×10^{-3} M CN^- (ARS, 5.0×10^{-5} M; NPBA, 2.0×10^{-4} M).

Furthermore, the influence of the concentration of phosphate buffer solution (PBS) over the fluorescence intensity of the system was studied. As shown in Figure 4.15b, the fluorescence quenching decreased with the increasing the concentration of buffer. The highest percentage quenching was achieved with 0.01 M PBS, thus the concentration of PBS at 0.01 M was selected for the optimal concentration.

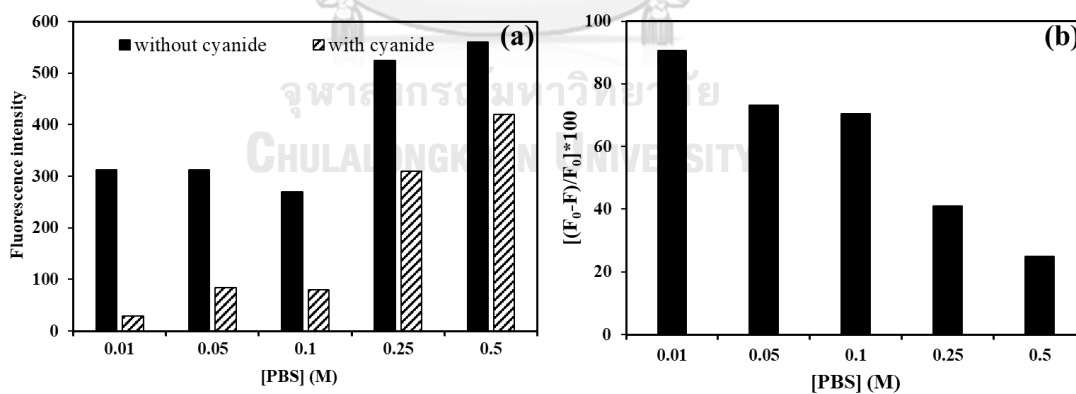


Figure 4.15 (a) The effect of PBS concentrations on the fluorescence intensity of ARS in the absence and in the presence of KCN at pH 8.0. (b) Fluorescence quenching of ARS–NPBA by 2.44×10^{-3} M CN^- (ARS, 5.0×10^{-5} M; NPBA, 2.0×10^{-4} M).

4.2.3 Studies of selectivity and cyanide sensing

The anion sensing ability of the **ARS–NPBA** ensemble was investigated using various anions including F^- , Cl^- , Br^- , I^- , AcO^- , ClO_4^- , SO_4^{2-} , NO_3^- , SCN^- , and CN^- in 0.01 M PBS buffer at pH 8.0. Solutions of **ARS–NPBA** were incubated with 50 equiv. of these anions for 20 min and then subjected to optical measurements. As illustrated in Figure 4.16, **ARS–NPBA** displayed only a distinct response to CN^- and other anions had no obvious effect in absorption and emission spectra. After the addition of the CN^- , there was a red shift in the absorption maxima at 475 nm into 500 nm with one isosbestic points at 304 nm and a decrease in the fluorescence emission at 590 nm. Moreover, the addition of CN^- to the solution of **ARS–NPBA** also caused a color change from orange to pink which was observed by the naked eyes (Figure 4.16c). All these findings suggested that **ARS–NPBA** allowed for the selective CN^- detection over other anions. We propose that this selectivity is attributed to its strong basicity and weak hydration enthalpy (-295 kJ mol^{-1}) of CN^- compared to other anions including most basic fluoride ions in aqueous media [12].

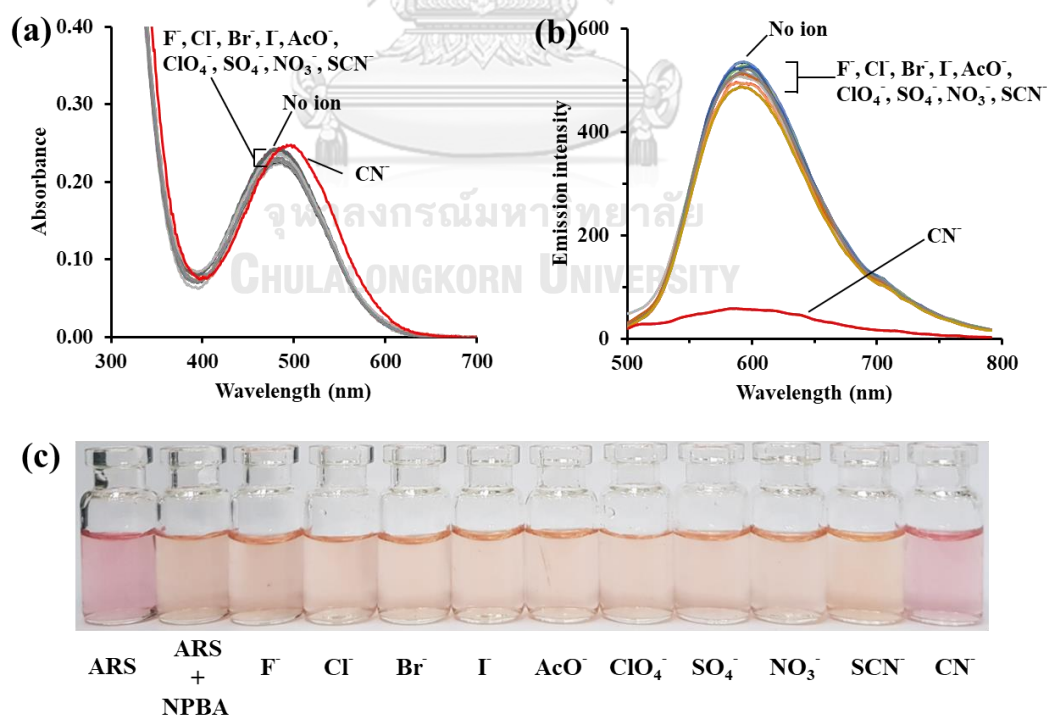


Figure 4.16 Changes in (a) absorption, (b) emission, and (c) color of **ARS–NPBA** (**ARS**, $5.0 \times 10^{-5} \text{ M}$; **NPBA**, $2.0 \times 10^{-4} \text{ M}$) upon addition of various anions (50 equiv.) in 0.01 M PBS buffer at pH 8.0.

It is well understanding that the interaction between **ARS** and **NPBA** in aqueous media through reversible boronate formation can be easily occurred because of the high affinity of boronic acids and diol moieties. However, boron possesses an empty p orbital that can accept an external lone pair electron, and thus strong nucleophilic CN^- can interact with the boron atom. Therefore, the corresponding complex with a tetrahedral configuration will be generated, which can weaken the linkage between boronic acid and diol [135]. The dissociation of this boronate ester bond leads to disassembling of **ARS** from the ensemble and the quenching of fluorescence.

To gain better insight into the sensing behavior of the **ARS-NPBA** to CN^- , ^{11}B NMR experiments were carried out. As shown in Figure 4.17, The ^{11}B NMR signal of **NPBA** in PBS buffer shows one boron signal at 27.3 ppm. The signal shifted to 2.5 ppm upon addition of CN^- , which attributed to a change from sp^2 to sp^3 boron on CN^- binding. On the other hand, the addition of CN^- into the solution of **ARS-NPBA** caused a signal at 3.5 ppm corresponding to tetrahedral $[\text{nCN}^--\text{NPBA}]^-$. To support the mentioned behavior, the solutions of **ARS-NPBA** before and after addition of CN^- were performed by ESI-MS spectrometry experiments. Upon reaction with CN^- , the MS peak at m/z 210.98 ascribed to $[\text{3CN}^--\text{NPBA}]^-$ was detected (Appendix 3). Considering the above evidences, we can suggest that the cyanide sensing behavior of this system arises from the reaction of cyanide and boronic acid to form tricyano borate resulting in the breakage of boronate ester bond and displacement of **ARS** from the ensemble.

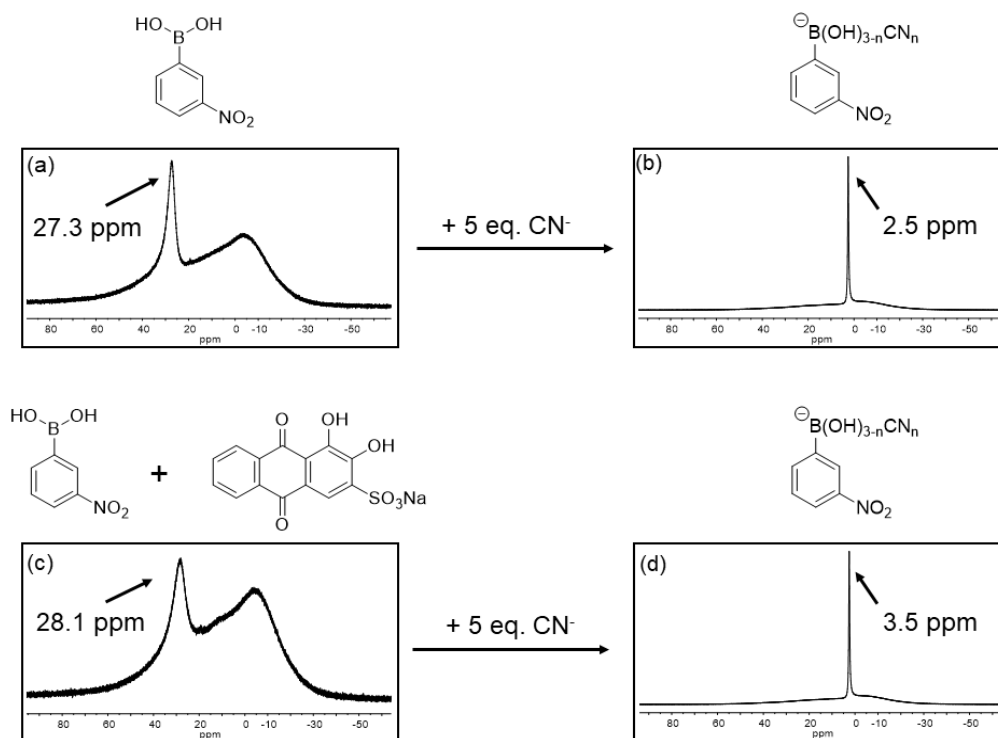


Figure 4.17 ^{11}B NMR spectra of NPBA in the absence or presence of ARS upon addition of KCN in 0.01 M PBS buffer at pH 8.0.

4.2.4 Studies of limit of detection and interferences

For quantitative analysis of cyanide ions, fluorescence titration with CN^- in varying concentrations was conducted. As shown in Figure 4.18, after gradual addition of the cyanide ions to the solution of ARS–NPBA, the emission intensity of ARS–NPBA at 590 nm gradually decreased and it was quenched linearly as a function of cyanide ion concentration. The detection limit of ARS–NPBA for CN^- was calculated to be 19.1 μM based on the fluorescence titration data using equation $3\sigma/m$, where σ refers the standard deviation of the blank solutions and m is the slope of the linear regression curve as shown in Figure 4.19.

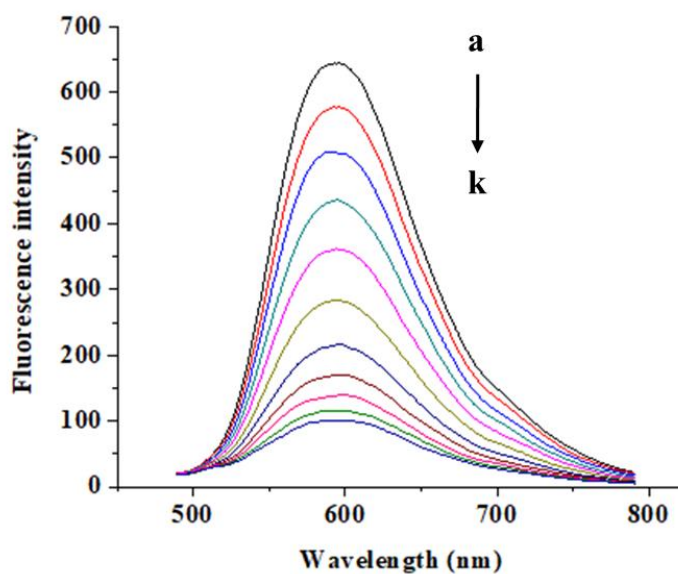


Figure 4.18 Fluorescence spectral changes of ARS–NPBA (ARS, 5.0×10^{-5} M; NPBA, 2.0×10^{-4} M) in the presence of different concentrations of CN^- in 0.01 M PBS buffer at pH 8.0. (a) 0 mM (0 eq.), (b) 0.25 mM (5 eq.), (c) 0.50 mM (10 eq.), (d) 0.74 mM (15 eq.), (e) 0.99 mM (20 eq.), (f) 1.23 mM (25 eq.), (g) 1.48 mM (30 eq.), (h) 1.72 mM (35 eq.), (i) 1.96 mM (40 eq.), (j) 2.20 mM (45 eq.), (k) 2.44 mM (50 eq.).

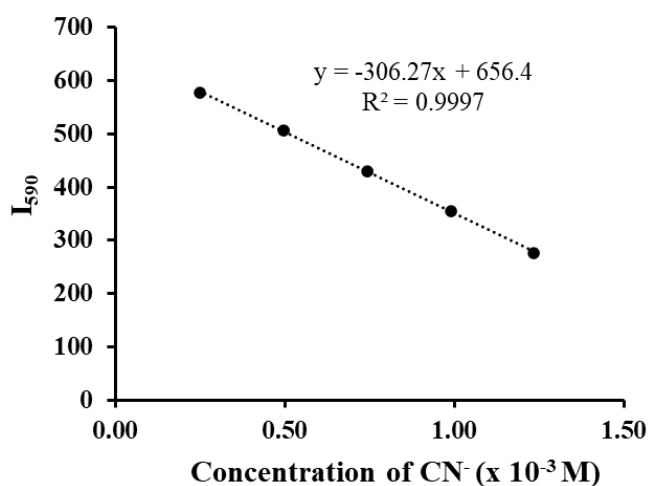


Figure 4.19 Calibration curve for detection cyanide using ARS–NPBA ensemble.

To test whether **ARS-NPBA** can detect CN^- selectively even in the presence of other anions, competitive experiments were carried out. The fluorescence signal of **ARS-NPBA** before and after the addition of CN^- (25 equiv., 1.25 mM) and other anions (50 equiv., 2.5 mM) was recorded. As presented in Figure 4.20, it is noticeable that the competitive anions did not lead to any significant change and CN^- ions still resulted in the similar fluorescence quenching in the presence of competitive anions. This result illustrated the high selectivity of the **ARS-NPBA** for CN^- over potential competitors and suggested that it could be used to detect CN^- in aqueous solutions.

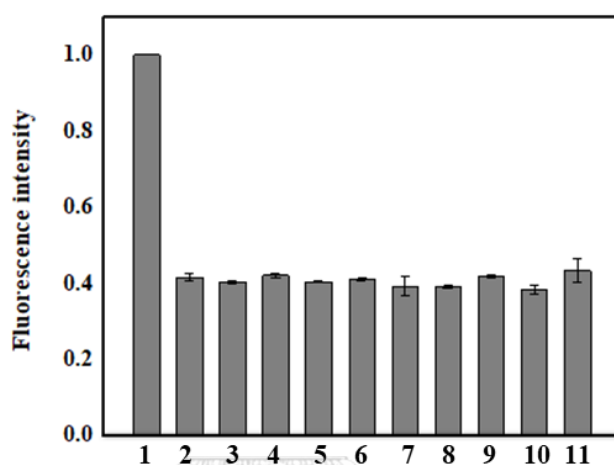


Figure 4.20 Competition experiments in the **ARS-NPBA-CN⁻** system with common foreign anions (**ARS**, 5.0×10^{-5} M; **NPBA**, 2.0×10^{-4} M; CN^- , 1.25 mM; X^- , 2.5 mM) in 0.01 M PBS buffer at pH 8.0 ; (1) = **ARS-NPBA**, (2) = **ARS-NPBA** + CN^- , (3) = (2) + F^- , (4) = (2) + Cl^- , (5) = (2) + Br^- , (6) = (2) + I^- , (7) = (2) + AcO^- , (8) = (2) + ClO_4^- , (9) = (2) + SO_4^{2-} , (10) = (2) + NO_3^- and (11) = (2) + SCN^- .

4.2.5 Determination of cyanide in real water samples

To investigate the practical applications of **ARS-NPBA** ensemble in real water samples, the sensing of CN^- was demonstrated in different source of water including drinking water, tap water, and pond water collected from Chulalongkorn university. The insoluble materials in the water samples were removed using a syringe filter (pore diameter 0.45 μm) prior to analysis. Three levels of cyanide concentrations of 0.4, 0.65, and 0.9 mM were performed for each sample to determine recoveries and the measured results were listed in Table 4.2. The recovery was in the range of 96 – 109 %, indicating that **ARS-NPBA** was suitable for the determination of CN^- concentration and could be applied in environmental analysis.

Table 4.2 The determination of cyanide ions in real water samples using **ARS–NPBA** sensor.

Sample	Added CN ⁻ (mM)	Found CN ⁻ (mM)	% Recovery	%RSD
Drinking water	0.40	0.44	108.9	1.17
	0.65	0.66	101.2	0.71
	0.90	0.87	96.3	1.76
Tap water	0.40	0.44	109.5	0.97
	0.65	0.67	103.6	1.04
	0.90	0.95	105.4	1.34
Pond water	0.40	0.43	107.3	0.26
	0.65	0.69	105.9	1.8
	0.90	0.98	109.1	2.41

4.2.6 Theoretical calculations

To clearly demonstrate the cyanide sensing behavior of the **ARS–NPBA** ensemble, theoretical calculations were performed. We first studied the reaction mechanism of **ARS–NPBA** formation and interaction with CN⁻ which can be proposed in equations (4.2) – (4.7). The optimized structures and calculated thermodynamic properties of all related steps in water are illustrated in Appendix 4 and 5.

Formation of ARS–NPBA(OH⁻):



Reaction with CN⁻:



It was found that the complexation between **ARS** and **NPBA** in aqueous solution is in a form of **ARS–NPBA(OH⁻)** with sp³ configuration (anionic form) as shown in **Figure 4.21**. The interaction of **ARS–NPBA** ensemble with two CN⁻ leads to the dissociation of **ARS** from the ensemble (equation (4.5 and 4.6)). In addition, an

excess of CN^- causes the formation of $\text{NPBA}(\text{CN})_3^-$ (equation (4.7)). Considering the dissociation of **ARS** when the ensemble interacts with two or more CN^- ions, the reaction should display no fluorescence emission. To corroborate this hypothesis, the simulated UV-vis of **ARS**, **ARS-NPBA**(OH^-), **ARS-NPBA**(CN^-) and **ARS/NPBA**($\text{CN})_2$ and fluorescence spectra of the **ARS-NPBA**(OH^-), **ARS-NPBA**(CN^-) were investigated by TD/DFT calculations and their maximum wavelengths are shown in Table 4.3.

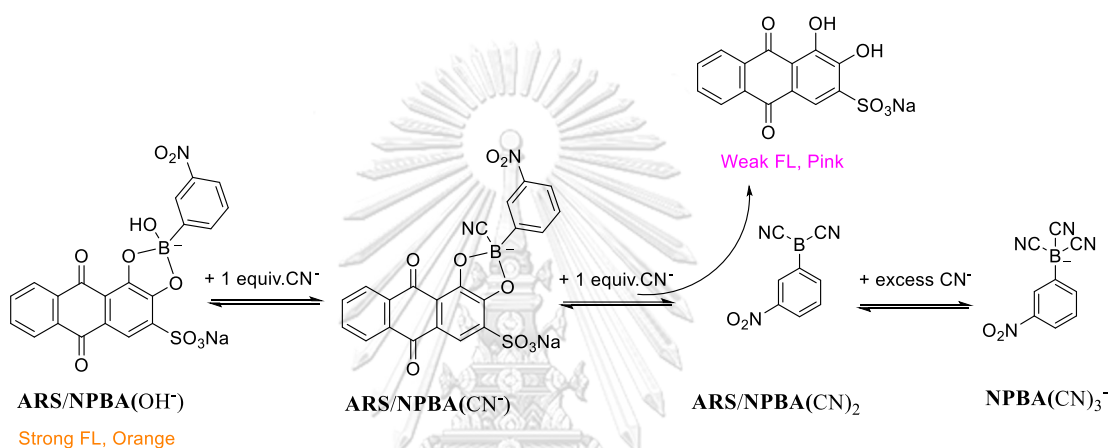


Figure 4.21 Proposed **ARS-NPBA** formation and interaction with CN^- .

Table 4.3 Computed UV-vis of **ARS**, its dominant complexes and fluorescence spectra of **ARS-NPBA**(OH^-) and **ARS-NPBA**(CN^-) in water, compared with experimental values.

Species	$\lambda_{\text{max}}^{\text{UV-Vis}}$ ^a		$\lambda_{\text{max}}^{\text{FL}}$ ^a		Stokes shift ^a	
	Exp. ^b	Comp.	Exp. ^b	Comp.	Exp.	Comp.
ARS	504	437 ^c	–	–	–	–
ARS-NPBA (OH^-)	486	436 ^c	580	558 ^e	94	122
ARS-NPBA (CN^-)	–	470 ^c	–	578 ^f	–	108
ARS/NPBA ($\text{CN})_2$	–	230, 508 ^d	–	–	–	–

^a In nm.

^b 0.01 M PBS buffer at pH 8.0.

^c Single-point calculation at the TD-CPCM/UFF/B3LYP/6-311+G(d,p) level.

^d Single-point calculation at the TD-CPCM/UFF/B3LYP/6-311G(d,p) level, separated two weak peaks of a combined peak.

^e Optimized at the TD-CPCM/UFF/B3LYP/6-311+G(d,p) level.

^f Optimized at the TD-CPCM/UFF/B3LYP/6-311G(d,p) level.



จุฬาลงกรณ์มหาวิทยาลัย
CHULALONGKORN UNIVERSITY

As indicated in Table 4.3, the ensemble in the form of **ARS-NPBA(OH⁻)** displays both absorption and emission and the calculated bands are close to those observed experimentally. The **ARS-NPBA(CN⁻)** specie still gives fluorescent emission indicating that the **ARS** is not displaced from the ensemble upon the interaction with one **CN⁻**. On the other hand, when interacting with two **CN⁻**, the **ARS** is displaced from the ensemble resulting in no emission in the **ARS/NPBA(CN)₂** specie. In addition, to evaluate spectral differences of the **ARS-NPBA** ensemble between free and bound cyanide, the UV-vis and fluorescence spectra of **ARS-NPBA(OH⁻)** and **ARS-NPBA(CN⁻)** were simulated and their optimized structures are depicted in Appendix 6. As shown in Figure 4.22, upon cyanide binding to the ensemble, the redshift in UV-vis bands and the decrease in fluorescence intensities are observed which is in agreement with the experimental phenomena.

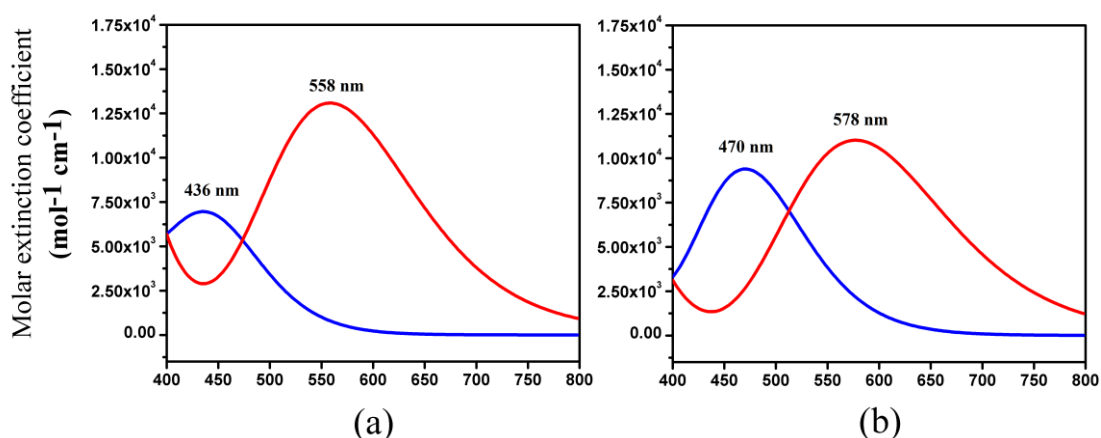


Figure 4.22 The simulated UV-vis and fluorescence spectra of (a) **ARS-NPBA(OH⁻)**, (b) **ARS-NPBA(CN⁻)**. The UV-vis and fluorescence bands are located at the left (in blue) and right (in red), respectively.

4.3 Conclusions

In summary, we have reported a colorimetric and fluorometric sensing system for cyanide detection in aqueous media using only the combination of commercially available compounds, **ARS** and **NPBA**, based on indicator displacement assay. Several parameters were studied to optimize the assay conditions including type of boronic acid, concentration of boronic acid, pH of the solution, and concentration of buffer. The effective sensing of the **ARS–NPBA** ensemble comes from the conversion of boronate ester to tricyano borate upon the addition of CN^- which leads to the dissociation of **ARS** from the ensemble, resulting in the recovery of the quenched fluorescence of the free **ARS**. This view is also supported by the results from the computational studies, in which the spectral changes agree well with the experimental ones. Our system provides an excellent selectivity toward cyanide over other common interfering anions and can be applied for the analysis of CN^- in real water samples including drinking, tap, and pond water. This assay method exhibits a cost-effective, rapid and simple solution for the determination of cyanide contamination in aqueous samples and does not involve complicated organic synthesis.

4.4 Experimental Section

4.4.1 General considerations

All commercially available reagents (analytical grade) were used as received without further purification. All aqueous solutions were prepared with Milli-Q water provided by ultra-pure water system. In the titration experiments, all solvents as high purity grade were used, and all anions (F^- , Cl^- , Br^- , I^- , CN^- , AcO^- , ClO_4^- , NO_3^- , SO_4^{2-} and SCN^-) were added in the form of potassium salts. ^{11}B NMR spectra were measured with a Bruker Advance III HD 500 MHz using boron trifluoride diethyl etherate, as external reference. UV-vis absorption spectra were recorded in a standard quartz cuvette cell of 1 cm in length at ambient temperature using a Varian Cary 50 UV-vis spectrophotometer. Fluorescence spectra were measured by a Varian Eclipse fluorescence spectrophotometer with parameters: excitation wavelength = 460 nm,

excitation/emission slit width = 10/10 nm, PMT = 700 V, and scan rate = 600 nm/min. Photographs were taken using a smartphone camera.

4.4.2 Spectroscopic experiments

Absorption and emission properties of ARS–NPBA. To prepare the ARS–NPBA ensemble, a solution of ARS (20 μL , 5.0×10^{-3} M) were mixed with a solution of NPBA (40 μL , 1.0×10^{-2} M) in 0.01 M PBS buffer at pH 8.0 to obtain the ARS–NPBA ensemble (2.0 mL, 5.0×10^{-5} M ARS, 2.0×10^{-4} M NPBA). The resulting mixture was incubated at room temperature for 20 min and then subjected to UV-vis and fluorescence measurements.

Effect of type of boronic acids. The ARS–BAs solution (2.0 mL, 5.0×10^{-5} M ARS, 2.0×10^{-4} M BAs) in 0.01 M PBS buffer at pH 8.0 in the absence and in the presence of potassium cyanide solution (KCN, 50 μL , 0.1 M) was investigated with different type of BAs. Four boronic acid derivatives studied in this work include phenylboronic acid (PBA), 3-aminophenylboronic acid (APBA), 3-nitrophenylboronic acid (NPBA), and (3-(methoxycarbonyl)-5-nitrophenyl)boronic acid (MNPBA).

Binding affinity of ARS with various BAs. The ARS solution (2.0 mL, 5.0×10^{-5} M) in 0.01 M PBS buffer at pH 8.0 was titrated with 5 μL aliquots of BA solution (0.01 M). After each addition, the resulting mixture was stirred for 5 min and then subjected to fluorescence measurements. Four boronic acid including PBA, APBA, NPBA and MNBA were used in this study. Experiments were performed in triplicate.

Effect of reaction time. The ARS–NPBA solution (2.0 mL, 5.0×10^{-5} M ARS, 2.0×10^{-4} M NPBA) in 0.01 M PBS buffer at pH 8.0 in the absence and in the presence of potassium cyanide solution (KCN, 50 μL , 0.1 M) was investigated and monitored by fluorescence spectroscopy every 5 min for a period of 60 min.

Effect of NPBA concentration. The ARS–NPBA solution (2 mL) was prepared with the final concentration of 5.0×10^{-5} M for ARS, and varying the concentration of NPBA ranging from 0.5 to 4.0×10^{-4} M. After incubated for 20 min, the fluorescence spectra were taken in the absence and in the presence of potassium cyanide solution (KCN, 50 μL , 0.1 M).

Effect of pH. The **ARS–NPBA** solution (2.0 mL, 5.0×10^{-5} M **ARS**, 2.0×10^{-4} M **NPBA**) in the absence and in the presence of potassium cyanide solution (KCN, 50 μ L, 0.1 M) was investigated with different pH of buffer solutions in the range of 4.0–12.0. The solution pHs were controlled by using 0.01 M of acetic-acetate buffer solution (pH 4.0–5.0), phosphate buffer solution (PBS, pH 6.0–8.0), sodium borate buffer solution (pH 6.0–8.0), and phosphate-NaOH buffer solution (pH 11.0–12.0).

Effect of PBS concentration. The **ARS–NPBA** solution (2.0 mL, 5.0×10^{-5} M **ARS**, 2.0×10^{-4} M **NPBA**) in the absence and in the presence of potassium cyanide solution (KCN, 50 μ L, 0.1 M) in PBS buffer at pH 8.0 was investigated with different concentration of PBS: 0.01 M, 0.05 M, 0.1 M, 0.25 M and 0.5 M.

Selectivity of the sensing system. A 50 μ L of each anion solution (0.1 M) was added into the ensemble solution of **ARS–NPBA** (2.0 mL, 5.0×10^{-5} M **ARS**, 2.0×10^{-4} M **NPBA**) in 0.01 M PBS buffer at pH 8.0. After incubated for 20 min, the fluorescence spectra were taken.

Titration of ARS–NPBA ensemble with cyanide. The **ARS–NPBA** solution (2.0 mL, 5.0×10^{-5} M **ARS**, 2.0×10^{-4} M **NPBA**) in 0.01 M PBS buffer at pH 8.0 was prepared and incubated for 20 min. The prepared ensemble was then titrated with 5 μ L aliquots of potassium cyanide solution (KCN, 0.1 M). After each addition, the resulting mixture was stirred for 5 min and then subjected to fluorescence measurements.

Competition of ARS–NPBA ensemble toward various anions. A 25 μ L of KCN solution (0.1 M) and 50 μ L of each anion solution (0.1 M) were added into the ensemble solution of **ARS–NPBA** (2.0 mL, 5.0×10^{-5} M **ARS**, 2.0×10^{-4} M **NPBA**) in 0.01 M PBS buffer at pH 8.0. After incubated for 20 min, the fluorescence spectra were taken.

Cyanide detection in real water samples. Commercially available drinking water was purchased from the local market. Tap water and pond water samples were collected from the laboratory and our university, respectively. All samples were kept at room temperature for a period of not more than 24 h prior to analysis. Then, the top layer of them was filtrated through 0.45 μ m filters for removing suspended material. For the analysis of water samples, suitable aliquot of standard stock solution of

potassium cyanide was added to 10 mL of water samples. Recovery experiments were carried out by spiking the samples (1 mL) to our system at three concentrations of cyanide, namely 0.4, 0.65 and 0.9 mM. The experiment was repeated 3 times with each sample.

4.4.3 Theoretical

4.4.3.1 DFT optimized structures in solution phases, energetics and thermodynamics properties

Structures optimizations of the **ARS**, **NPBA**, their complexes such as **ARS–NPBA(OH⁻)**, **ARS–NPBA(OH⁻)/H₃O⁺**, **ARS–NPBA(CN⁻)** and related species were carried out using density functional theory (DFT) method of which calculations were performed with the B3LYP which is the hybrid exchange-correlation functionals B3LYP [136, 137]. The 6-311+G(d,p) [138] and/or 6-311G(d,p) [139] basis sets were employed with the B3LYP, denoted by B3LYP/6-311+G(d,p) and B3LYP/6-311G(d,p) methods, respectively. Structures optimizations of all studied compounds in water were carried out by including with solvent-effect of the CPCM [140-142] method which is the polarizable continuum model (PCM) [143-145] with molecular cavity model of the united atoms radii using UFF force field [146]. All structure optimizations are therefore called as the CPCM/UFF/B3LYP/6-311+G(d,p) method. The zero-point energies (E_{ZPE}) of all studied compounds were derived from frequency calculations which are corrected by ZPVE (zero-point vibrational energy). Energy (ΔE_{ZPE}), enthalpy (ΔH_{298}°) and Gibbs free energy changes (ΔG_{298}°) of reactions, at 1 atm and 298 K, were derived from related frequency calculations.

4.4.3.2 Simulated UV-vis and Fluorescence spectra

The UV-vis spectra of **ARS**, **ARS–NPBA(OH⁻)**, **ARS–NPBA(CN⁻)** and **ARS/NPBA(CN)₂** in water were obtained using single-point TD-DFT calculation [147, 148] of their CPCM/UFF/B3LYP/6-311+G(d,p)-optimized structures. The TD-CPCM/UFF/B3LYP/6-311+G(d,p), the number of singlet states of electronic states

of 25 (NStates=25) was used. All the UV-vis spectra were simulated by the GaussView 5 software [149] using oscillator strengths outputs of the single-point TD-DFT calculation. The full width at half-maximum (FWHM) of $2,700\text{ cm}^{-1}$ was selected for construction of the simulated UV-vis spectrum.

The fluorescence spectra of **ARS** and **ARS-NPBA(OH⁻)** were simulated using the TD-CPCM/UFF/B3LYP/6-311+G(d,p)-optimized excited-state structures where the 6-311+G(d,p) basis set was selected due to reduction of computational time. All calculations of DFT, TD-DFT, simulated UV-vis and fluorescence spectra were performed with the GAUSSIAN 09 program [150] and GaussView 5 software [149].



CHAPTER V

CONCLUSIONS

Summary and future work

The objectives of this dissertation were to develop boron- and copper complex-based receptors for anion recognition, to conduct experiments based on chemosensing ensemble approach, and to perform applications in fluoride and cyanide sensing. All of these objectives have been met and fully discussed in the corresponding Chapters.

Lewis acid organoboron compounds were selected for investigation in the first project, with the main focus being on the chemistry of them for the complexation of fluoride and cyanide anions. Two boranes, mono- and bis-functionalized anthracene derivatives **1** and **2**, were successfully synthesized. The X-ray crystal structures of them were obtained and the interesting photophysical properties upon complexing with fluoride and cyanide were discovered. Given the fact that the chemistry of Lewis acids for anion recognition can be extended, future directions for this project are suggested. Such examples include the enhancement of the Lewis acidity of the boranes by incorporation of the electron-withdrawing substituents, and the development of anthracene-based Lewis acids using other main group elements instead of boron (antimony, tellurium and bismuth).

Another objective of this research is based on chemosensing ensemble approach described in the second and third project. The $\text{Cu}_2\text{L1-PGR}$ ensemble, reported in the second project, displayed a high selective sensing ability toward cyanide and was able to detect cyanide at concentration as low as 0.029 ppm. However, the sensing behavior did not involve an indicator displacement. There was also trouble in confirming the sensing mechanism by experimental studies due to the limitation of Cu(II) nuclear spin. Thus, the sensing mechanism of this system, proposed to be $\text{Cu}_2\text{L1}$ induced nucleophilic addition of cyanide to **PGR** unit, was supported by TD/DFT calculations. Future work may be directed toward the design of

various metal complexes that contain several subunits to assist and stabilize the binding status between metal centers, indicators, and target analytes for sensing of cyanide and other anions. However, synthetic difficulties will need to be overcome.

The last project involved a fluorometric and colorimetric sensing system for detection of cyanide using an easy-to-prepare ensemble. The combination of **ARS** indicator with different commercial phenylboronic acid receptor was tested and **ARS-NPBA** was found to be the best ensemble for sensing of cyanide. The optimum conditions were obtained by varying various parameters. Also, this system was successfully applied in determination of cyanide concentration in real water samples. In the future, the development of **ARS-BAs** ensemble with the use of surfactants, polymers, and hydrogels to facilitate and improve the sensitivity of the sensing system should be considered.



REFERENCES

- [1] Dhillon, A., Nair, M., and Kumar, D. Analytical methods for determination and sensing of fluoride in biotic and abiotic sources: a review. Analytical Methods 8(27) (2016): 5338-5352.
- [2] Yang, S., Liu, Y., and Feng, G. Rapid and selective detection of fluoride in aqueous solution by a new hemicyanine-based colorimetric and fluorescent chemodosimeter. RSC Advances 3(43) (2013): 20171-20178.
- [3] Zhou, Y., Zhang, J.F., and Yoon, J. Fluorescence and Colorimetric Chemosensors for Fluoride-Ion Detection. Chemical Reviews 114(10) (2014): 5511-5571.
- [4] Chansaenpak, K., Kamkaew, A., Weeranantanapan, O., Suttisintong, K., and Tumcharern, G. Coumarin Probe for Selective Detection of Fluoride Ions in Aqueous Solution and Its Bioimaging in Live Cells. Sensors 18(7) (2018).
- [5] Bhat, M.P., et al. Turmeric, naturally available colorimetric receptor for quantitative detection of fluoride and iron. Chemical Engineering Journal 303 (2016): 14-21.
- [6] Hirai, M., Myahkostupov, M., Castellano, F.N., and Gabbai, F.P. 1-Pyrenyl- and 3-Perylenyl-antimony(V) Derivatives for the Fluorescence Turn-On Sensing of Fluoride Ions in Water at Sub-ppm Concentrations. Organometallics 35(11) (2016): 1854-1860.
- [7] Jo, H.Y., Park, G.J., Na, Y.J., Choi, Y.W., You, G.R., and Kim, C. Sequential colorimetric recognition of Cu²⁺ and CN⁻ by asymmetric coumarin-conjugated naphthol groups in aqueous solution. Dyes and Pigments 109 (2014): 127-134.
- [8] Zheng, W., He, X., Chen, H., Gao, Y., and Li, H. Colorimetric fluorescent cyanide chemodosimeter based on triphenylimidazole derivative. Spectrochimica Acta Part A: Molecular and Biomolecular Spectroscopy 124 (2014): 97-101.
- [9] Zali-Boeini, H. and Zareh Jonaghani, M. New Fluorescent and Colorimetric Chemosensor for Detection of Cyanide with High Selectivity and Sensitivity in Aqueous Media. Journal of fluorescence 27(3) (2017): 1035-1040.
- [10] Wang, L., Chen, X., and Cao, D. A cyanide-selective colorimetric “naked-eye” and fluorescent chemosensor based on a diketopyrrolopyrrole-hydrazone conjugate and its use for the design of a molecular-scale logic device. RSC Advances 6(99) (2016): 96676-96685.
- [11] Kumar, R., Chaudhri, N., and Sankar, M. Ratiometric and colorimetric “naked eye” selective detection of CN⁻ ions by electron deficient Ni(ii) porphyrins and their reversibility studies. Dalton Transactions 44(19) (2015): 9149-9157.
- [12] Keshav, K., et al. Highly selective optical and reversible dual-path chemosensor for cyanide detection and its application in live cells imaging. Biosens Bioelectron 92 (2017): 95-100.
- [13] Roy, S.B., Maity, A., and Rajak, K.K. A turn-off fluorescence sensor for cyanide detection which in turn inhibit 2-way ESIPT investigated by experimental and theoretical study. Inorganic Chemistry Communications 76 (2017): 81-86.
- [14] Sun, W., Guo, S., Hu, C., Fan, J., and Peng, X. Recent Development of Chemosensors Based on Cyanine Platforms. Chem Rev 116(14) (2016): 7768-7817.

- [15] Wiskur, S.L., Ait-Haddou, H., Lavigne, J.J., and Anslyn, E.V. Teaching Old Indicators New Tricks. Accounts of Chemical Research 34(12) (2001): 963-972.
- [16] Wu, J., Kwon, B., Liu, W., Anslyn, E.V., Wang, P., and Kim, J.S. Chromogenic/Fluorogenic Ensemble Chemosensing Systems. Chem Rev 115(15) (2015): 7893-7943.
- [17] Fabbrizzi, L., Leone, A., and Taglietti, A. A Chemosensing Ensemble for Selective Carbonate Detection in Water Based on Metal–Ligand Interactions. Angewandte Chemie International Edition 40(16) (2001): 3066-3069.
- [18] Galbraith, E. and James, T.D. Boron based anion receptors as sensors. Chem Soc Rev 39(10) (2010): 3831-42.
- [19] Sole, S. and Gabbai, F.P. A bidentate borane as colorimetric fluoride ion sensor. Chem Commun (Camb) (11) (2004): 1284-5.
- [20] Yamaguchi, S., Akiyama, S., and Tamao, K. Colorimetric Fluoride Ion Sensing by Boron-Containing π -Electron Systems. Journal of the American Chemical Society 123(46) (2001): 11372-11375.
- [21] Katz, H.E. Hydride sponge: complexation of 1,8-naphthalenediylbis(dimethylborane) with hydride, fluoride, and hydroxide. The Journal of Organic Chemistry 50(25) (1985): 5027-5032.
- [22] Williams, V.C., Piers, W.E., Clegg, W., Elsegood, M.R.J., Collins, S., and Marder, T.B. New Bifunctional Perfluoroaryl Boranes. Synthesis and Reactivity of the ortho-Phenylene-Bridged Diboranes 1,2-[B(C₆F₅)₂]₂C₆X₄ (X = H, F). Journal of the American Chemical Society 121(13) (1999): 3244-3245.
- [23] Han, M.S. and Kim, D.H. Naked-Eye Detection of Phosphate Ions in Water at Physiological pH: A Remarkably Selective and Easy-To-Assemble Colorimetric Phosphate-Sensing Probe. Angewandte Chemie International Edition 41(20) (2002): 3809-3811.
- [24] Amendola, V., et al. Halide-Ion Encapsulation by a Flexible Dicopper(II) Bis-Tren Cryptate. Angewandte Chemie International Edition 39(16) (2000): 2917-2920.
- [25] Liu, X., Ngo, H.T., Ge, Z., Butler, S.J., and Jolliffe, K.A. Tuning colourimetric indicator displacement assays for naked-eye sensing of pyrophosphate in aqueous media. Chemical Science 4(4) (2013): 1680-1686.
- [26] Mishra, A., et al. Self-assembled metalla-bowls for selective sensing of multicarboxylate anions. Dalton Transactions 41(4) (2012): 1195-1201.
- [27] Tang, L., et al. Tight Binding and Fluorescent Sensing of Oxalate in Water. Journal of the American Chemical Society 130(38) (2008): 12606-12607.
- [28] Rhaman, M.M., Alamgir, A., Wong, B.M., Powell, D.R., and Hossain, M.A. A highly efficient dinuclear Cu(ii) chemosensor for colorimetric and fluorescent detection of cyanide in water. RSC Advances 4(97) (2014): 54263-54267.
- [29] Watchasit, S., Suktanarak, P., Suksai, C., Ruangpornvisuti, V., and Tuntulani, T. Discriminate sensing of pyrophosphate using a new tripodal tetramine-based dinuclear Zn(II) complex under an indicator displacement assay approach. Dalton Trans 43(39) (2014): 14701-14709.
- [30] Guo, Z., Shin, I., and Yoon, J. Recognition and sensing of various species using boronic acid derivatives. Chem Commun (Camb) 48(48) (2012): 5956-67.
- [31] Sun, X., et al. Reaction-based Indicator displacement Assay (RIA) for the selective colorimetric and fluorometric detection of peroxyxynitrite. Chem Sci 6(5)

- (2015): 2963-2967.
- [32] Park, G., Brock, D.J., Pellois, J.P., and Gabbai, F.P. Heavy Pnictogenium Cations as Transmembrane Anion Transporters in Vesicles and Erythrocytes. Chem 5(8) (2019): 2215-2227.
- [33] Park, G. and Gabbai, F.P. Phosphonium Boranes for the Selective Transport of Fluoride Anions across Artificial Phospholipid Membranes. Angew Chem Int Ed Engl 59(13) (2020): 5298-5302.
- [34] von Grotthuss, E., Prey, S.E., Bolte, M., Lerner, H.W., and Wagner, M. Dual Role of Doubly Reduced Arylboranes as Dihydrogen- and Hydride-Transfer Catalysts. J Am Chem Soc 141(14) (2019): 6082-6091.
- [35] Taylor, J.W., McSkimming, A., Guzman, C.F., and Harman, W.H. N-Heterocyclic Carbene-Stabilized Boranthrene as a Metal-Free Platform for the Activation of Small Molecules. J Am Chem Soc 139(32) (2017): 11032-11035.
- [36] Jiang, C., Blacque, O., and Berke, H. Metal-free hydrogen activation and hydrogenation of imines by 1,8-bis(dipentafluorophenylboryl)naphthalene. Chem Commun (Camb) (37) (2009): 5518-20.
- [37] Wang, B. and Kinjo, R. Boron-based stepwise dioxygen activation with 1,4,2,5-diazadiborinine. Chem Sci 10(7) (2019): 2088-2092.
- [38] Tsukahara, N., Asakawa, H., Lee, K.H., Lin, Z., and Yamashita, M. Cleaving Dihydrogen with Tetra(o-tolyl)diborane(4). J Am Chem Soc 139(7) (2017): 2593-2596.
- [39] Schweighauser, L. and Wegner, H.A. Bis-Boron Compounds in Catalysis: Bidentate and Bifunctional Activation. Chemistry 22(40) (2016): 14094-103.
- [40] Lewis, S.P., Taylor, N.J., Piers, W.E., and Collins, S. Isobutene Polymerization Using a Chelating Diborane Co-Initiator. Journal of the American Chemical Society 125(48) (2003): 14686-14687.
- [41] Chai, J., et al. Formation of Chelated Counteranions Using Lewis Acidic Diboranes: Relevance to Isobutene Polymerization. Organometallics 26(23) (2007): 5667-5679.
- [42] Chen, D., Xu, G., Zhou, Q., Chung, L.W., and Tang, W. Practical and Asymmetric Reductive Coupling of Isoquinolines Templated by Chiral Diborons. J Am Chem Soc 139(29) (2017): 9767-9770.
- [43] Katz, H.E. 1,8-Naphthalenediylbis(dichloroborane) chloride: the first bis boron chloride chelate. Organometallics 6(5) (1987): 1134-1136.
- [44] Solé, S. and Gabbai, F.P. A bidentate borane as colorimetric fluoride ion sensor. Chemical Communications (11) (2004): 1284-1285.
- [45] Melaimi, M. and Gabbai, F.P. A Heteronuclear Bidentate Lewis Acid as a Phosphorescent Fluoride Sensor. Journal of the American Chemical Society 127(27) (2005): 9680-9681.
- [46] Dorsey, C.L., et al. Fluoride ion complexation by a B₂/Hg heteronuclear tridentate lewis acid. Dalton Transactions (33) (2008): 4442-4450.
- [47] Zhao, H. and Gabbai, F.P. On the Synergy of Coulombic and Chelate Effects in Bidentate Diboranes: Synthesis and Anion Binding Properties of a Cationic 1,8-Diborylnaphthalene. Organometallics 31(6) (2012): 2327-2335.
- [48] Huh, J.O., Kim, H., Lee, K.M., Lee, Y.S., Do, Y., and Lee, M.H. o-Carborane-assisted Lewis acidity enhancement of triarylboranes. Chem Commun (Camb) 46(7) (2010): 1138-40.

- [49] Scheer, M. The coordination chemistry of group 15 element ligand complexes--a developing area. Dalton Trans (33) (2008): 4372-86.
- [50] Wade, C.R., Broomsgrove, A.E.J., Aldridge, S., and Gabbai, F.P. Fluoride Ion Complexation and Sensing Using Organoboron Compounds. Chemical Reviews 110(7) (2010): 3958-3984.
- [51] Chen, C.H. and Gabbai, F.P. Large-bite diboranes for the $\mu(1,2)$ complexation of hydrazine and cyanide. Chem Sci 9(29) (2018): 6210-6218.
- [52] Katz, H.E. 1,8-Anthracenediethynylbis(catechol boronate): a bidentate Lewis acid on a novel framework. The Journal of Organic Chemistry 54(9) (1989): 2179-2183.
- [53] Niermeier, P., et al. Bidentate Boron Lewis Acids: Selectivity in Host-Guest Complex Formation. Angew Chem Int Ed Engl 58(7) (2019): 1965-1969.
- [54] Zheng, Y., Xiong, J., Sun, Y., Pan, X., and Wu, J. Stepwise Reduction of 9,10-Bis(dimesitylboryl)anthracene. Angew Chem Int Ed Engl 54(44) (2015): 12933-6.
- [55] Liu, K., Lalancette, R.A., and Jakle, F. Tuning the Structure and Electronic Properties of B-N Fused Dipyridylanthracene and Implications on the Self-Sensitized Reactivity with Singlet Oxygen. J Am Chem Soc 141(18) (2019): 7453-7462.
- [56] Grossman, O., Azerraf, C., and Gelman, D. Palladium Complexes Bearing Novel Strongly Bent Trans-Spanning Diphosphine Ligands: Synthesis, Characterization, and Catalytic Activity. Organometallics 25(2) (2006): 375-381.
- [57] Liu, X.Y., Bai, D.R., and Wang, S. Charge-Transfer Emission in Nonplanar Three-Coordinate Organoboron Compounds for Fluorescent Sensing of Fluoride. Angewandte Chemie International Edition 45(33) (2006): 5475-5478.
- [58] Zhao, S.-B., et al. Impact of the Linker on the Electronic and Luminescent Properties of Diboryl Compounds: Molecules with Two BMes₂ Groups and the Peculiar Behavior of 1,6-(BMes₂)₂pyrene. Organometallics 27(24) (2008): 6446-6456.
- [59] Chen, C.H. and Gabbai, F.P. Exploiting the Strong Hydrogen Bond Donor Properties of a Borinic Acid Functionality for Fluoride Anion Recognition. Angew Chem Int Ed Engl 57(2) (2018): 521-525.
- [60] Su, Y. and Kinjo, R. Boron-containing radical species. Coordination Chemistry Reviews 352 (2017): 346-378.
- [61] Cummings, S.A., et al. An Estimate of the Reduction Potential of B(C₆F₅)₃ from Electrochemical Measurements on Related Mesityl Boranes. Organometallics 25(7) (2006): 1565-1568.
- [62] Loutfy, R.O. and Loutfy, R.O. The interrelation between polarographic half-wave potentials and the energies of electronic excited states. Canadian Journal of Chemistry 54(9) (1976): 1454-1463.
- [63] Fabre, B., Bassani, D.M., Liang, C.-K., Ray, D., Hui, F., and Hapiot, P. Anthracene and Anthracene:C₆₀ Adduct-Terminated Monolayers Covalently Bound to Hydrogen-Terminated Silicon Surfaces. The Journal of Physical Chemistry C 115(30) (2011): 14786-14796.
- [64] Wurth, C., Grabolle, M., Pauli, J., Spieles, M., and Resch-Genger, U. Relative and absolute determination of fluorescence quantum yields of transparent samples. Nat Protoc 8(8) (2013): 1535-50.

- [65] Ke, I.S., Myahkostupov, M., Castellano, F.N., and Gabbai, F.P. Stibonium ions for the fluorescence turn-on sensing of F⁻ in drinking water at parts per million concentrations. J Am Chem Soc 134(37) (2012): 15309-11.
- [66] O'Neil, E.J. and Smith, B.D. Anion recognition using dimetallic coordination complexes. Coordination Chemistry Reviews 250(23) (2006): 3068-3080.
- [67] Xue, Z., Xiong, L., Peng, H., Rao, H., Liu, X., and Lu, X. A selective colorimetric sensing strategy for cysteine based on an indicator-displacement mechanism. New Journal of Chemistry 42(6) (2018): 4324-4330.
- [68] Nguyen, B.T. and Anslyn, E.V. Indicator-displacement assays. Coordination Chemistry Reviews 250(23-24) (2006): 3118-3127.
- [69] Coggins, M.K., Parker, A.M., Mangalum, A., Galdamez, G.A., and Smith, R.C. Dizinc Phosphohydrolase Model Built on a m-Terphenyl Scaffold and Its Use in Indicator Displacement Assays for Pyrophosphate Under Physiological Conditions. European Journal of Organic Chemistry 2009(3) (2009): 343-348.
- [70] Yu, W., et al. Ammonium-Bearing Dinuclear Copper(II) Complex: A Highly Selective and Sensitive Colorimetric Probe for Pyrophosphate. Organic Letters 16(8) (2014): 2220-2223.
- [71] Ngo, H.T., Liu, X., and Jolliffe, K.A. Anion recognition and sensing with Zn(II)-dipicolylamine complexes. Chem Soc Rev 41(14) (2012): 4928-65.
- [72] Ojida, A., Mito-oka, Y., Inoue, M.-a., and Hamachi, I. First Artificial Receptors and Chemosensors toward Phosphorylated Peptide in Aqueous Solution. Journal of the American Chemical Society 124(22) (2002): 6256-6258.
- [73] Blackman, A.G. The coordination chemistry of tripodal tetraamine ligands. Polyhedron 24(1) (2005): 1-39.
- [74] Blackman, A.G. Tripodal Tetraamine Ligands Containing Three Pyridine Units: Theother Polypyridyl Ligands. European Journal of Inorganic Chemistry 2008(17) (2008): 2633-2647.
- [75] Qiang, J., et al. A dinuclear-copper(II) complex-based sensor for pyrophosphate and its applications to detecting pyrophosphatase activity and monitoring polymerase chain reaction. Sensors and Actuators B: Chemical 233 (2016): 591-598.
- [76] Rhaman, M.M., Fronczek, F.R., Powell, D.R., and Hossain, M.A. Colourimetric and fluorescent detection of oxalate in water by a new macrocycle-based dinuclear nickel complex: a remarkable red shift of the fluorescence band. Dalton Trans 43(12) (2014): 4618-21.
- [77] Das, B., et al. Water oxidation catalyzed by molecular di- and nonanuclear Fe complexes: importance of a proper ligand framework. Dalton Transactions 45(34) (2016): 13289-13293.
- [78] Buryak, A. and Severin, K. An organometallic chemosensor for the sequence-selective detection of histidine- and methionine-containing peptides in water at neutral pH. Angew Chem Int Ed Engl 43(36) (2004): 4771-4.
- [79] Esteves, C.V., Esteban-Gomez, D., Platas-Iglesias, C., Tripier, R., and Delgado, R. Steric Effects on the Binding of Phosphate and Polyphosphate Anions by Zinc(II) and Copper(II) Dinuclear Complexes of m-Xylyl-bis-cyclen. Inorg Chem 57(11) (2018): 6466-6478.
- [80] Zwicker, V.E., Long, B.M., and Jolliffe, K.A. Selective sensing of pyrophosphate in physiological media using zinc(ii)dipicolylamino-

- functionalised peptides. Organic & Biomolecular Chemistry 13(28) (2015): 7822-7829.
- [81] Zhu, Z., Zhou, J., Li, Z., and Yang, C. Dinuclear zinc complex for fluorescent indicator-displacement assay of citrate. Sensors and Actuators B: Chemical 208 (2015): 151-158.
- [82] Jolliffe, K.A. Pyrophosphate Recognition and Sensing in Water Using Bis[zinc(II)dipicolylamino]-Functionalized Peptides. Acc Chem Res 50(9) (2017): 2254-2263.
- [83] Kim, S.K., Lee, D.H., Hong, J.-I., and Yoon, J. Chemosensors for Pyrophosphate. Accounts of Chemical Research 42(1) (2009): 23-31.
- [84] Li, Z., et al. Di-nuclear Cu(II) complex bearing guanidinium arms for sensing pyrophosphate and monitoring the activity of PPase. Dyes and Pigments 163 (2019): 243-248.
- [85] Watchasit, S., Kaowliw, A., Suksai, C., Tuntulani, T., Ngeontae, W., and Pakawatchai, C. Selective detection of pyrophosphate by new tripodal amine calix[4]arene-based Cu(II) complexes using indicator displacement strategy. Tetrahedron Letters 51(26) (2010): 3398-3402.
- [86] Sasaki, Y., Minamiki, T., Tokito, S., and Minami, T. A molecular self-assembled colourimetric chemosensor array for simultaneous detection of metal ions in water. Chem Commun (Camb) 53(49) (2017): 6561-6564.
- [87] Wang, M., Xu, J., Liu, X., and Wang, H. A highly selective pyrene based “off-on” fluorescent chemosensor for cyanide. New Journal of Chemistry 37(12) (2013).
- [88] Gupta, R.C., et al. An efficient Hg²⁺ ensemble based on a triazole bridged anthracene and quinoline system for selective detection of cyanide through fluorescence turn-off-on response in solution and live cell. Sensors and Actuators B: Chemical 251 (2017): 729-738.
- [89] Jang, H.J., Kang, J.H., Lee, M., Lim, M.H., and Kim, C. Fluorescent Sensor for Sequentially Monitoring Zinc(II) and Cyanide Anion in Near-Perfect Aqueous Media. Industrial & Engineering Chemistry Research 57(1) (2017): 54-62.
- [90] Kaushik, R., Ghosh, A., Singh, A., Gupta, P., Mittal, A., and Jose, D.A. Selective Detection of Cyanide in Water and Biological Samples by an Off-the-Shelf Compound. ACS Sensors 1(10) (2016): 1265-1271.
- [91] Bhalla, V., Singh, H., and Kumar, M. Triphenylene based copper ensemble for the detection of cyanide ions. Dalton Trans 41(37) (2012): 11413-8.
- [92] Alreja, P., Saini, D., Gautam, S.S., Navneet, and Kaur, N. Novel 1,10-phenanthroline - di-2-picoylamine scaffold as a selective chemosensor for copper and cyanide ions. Inorganic Chemistry Communications 70 (2016): 125-128.
- [93] Yanai, T., Tew, D.P., and Handy, N.C. A new hybrid exchange-correlation functional using the Coulomb-attenuating method (CAM-B3LYP). Chemical Physics Letters 393(1) (2004): 51-57.
- [94] J. M. Hehre, W., Ditchfield, R., and Pople, J.A. Self-Consistent Molecular Orbital Methods. XII. Further Extensions of Gaussian-Type Basis Sets for Use in Molecular Orbital Studies of Organic Molecules. Vol. 56, 1972.
- [95] Gordon, M.S. The isomers of silacyclopropane. Chemical Physics Letters 76(1) (1980): 163-168.

- [96] Cancès, E., Mennucci, B., and Tomasi, J. A new integral equation formalism for the polarizable continuum model: Theoretical background and applications to isotropic and anisotropic dielectrics. The Journal of Chemical Physics 107(8) (1997): 3032-3041.
- [97] Mennucci, B. and Tomasi, J. Continuum solvation models: A new approach to the problem of solute's charge distribution and cavity boundaries. Vol. 106, 1997.
- [98] Tomasi, J., Mennucci, B., and Cancès, E. The IEF version of the PCM solvation method: An overview of a new method addressed to study molecular solutes at the QM ab initio level. 1999. 211-226.
- [99] Frisch, M.J., et al. Gaussian 09 Revision D.01. Wallingford, CT: Gaussian Inc., 2014.
- [100] Caricato, M., et al. Formation and relaxation of excited states in solution: A new time dependent polarizable continuum model based on time dependent density functional theory. Vol. 124, 2006.
- [101] O'Boyle, N.M., Tenderholt, A.L., and Langner, K.M. cclib: a library for package-independent computational chemistry algorithms. J Comput Chem 29(5) (2008): 839-45.
- [102] Chaicham, A., Kulchat, S., Tumcharern, G., Tuntulani, T., and Tomapatanaget, B. Synthesis, photophysical properties, and cyanide detection in aqueous solution of BF₂-curcumin dyes. Tetrahedron 66(32) (2010): 6217-6223.
- [103] Zhou, X., Lv, X., Hao, J., Liu, D., and Guo, W. Coumarin⁶-indanedione conjugate as a doubly activated Michael addition type probe for the colorimetric and ratiometric fluorescent detection of cyanide. Dyes and Pigments 95(2) (2012): 168-173.
- [104] Zheng, W., He, X., Chen, H., Gao, Y., and Li, H. Colorimetric fluorescent cyanide chemodosimeter based on triphenylimidazole derivative. Spectrochim Acta A Mol Biomol Spectrosc 124 (2014): 97-101.
- [105] Xu, Z., Chen, X., Kim, H.N., and Yoon, J. Sensors for the optical detection of cyanide ion. Chem Soc Rev 39(1) (2010): 127-137.
- [106] Feng, L., Wang, Y., Liang, F., Liu, W., Wang, X., and Diao, H. A specific sensing ensemble for cyanide ion in aqueous solution. Sensors and Actuators B: Chemical 168 (2012): 365-369.
- [107] Jamkratoke, M., Ruangpornvisuti, V., Tumcharern, G., Tuntulani, T., and Tomapatanaget, B. A-D-A Sensors Based on Naphthoimidazoledione and Boronic Acid as Turn-On Cyanide Probes in Water. The Journal of Organic Chemistry 74(10) (2009): 3919-3922.
- [108] Guan, R., Chen, H., Cao, F., Cao, D., and Deng, Y. Two fluorescence turn-on chemosensors for cyanide anions based on pyridine cation and the boronic acid moiety. Inorganic Chemistry Communications 38 (2013): 112-114.
- [109] Badugu, R., Lakowicz, J.R., and Geddes, C.D. Cyanide-sensitive fluorescent probes. Dyes and Pigments 64(1) (2005): 49-55.
- [110] Badugu, R., Lakowicz, J.R., and Geddes, C.D. Enhanced Fluorescence Cyanide Detection at Physiologically Lethal Levels- Reduced ICT-Based Signal Transduction. J. Am. Chem. Soc. 127(10) (2005): 3635-3641.
- [111] Jamkratoke, M., Tumcharern, G., Tuntulani, T., and Tomapatanaget, B. A selective spectrofluorometric determination of micromolar level of cyanide in

- water using naphthoquinone imidazole boronic-based sensors and a surfactant cationic CTAB micellar system. J Fluoresc 21(3) (2011): 1179-1187.
- [112] Liang, X. and Bonizzoni, M. Boronic acid-modified poly(amidoamine) dendrimers as sugar-sensing materials in water. Journal of Materials Chemistry B 4(18) (2016): 3094-3103.
- [113] Zhong, Z. and Anslyn, E.V. A Colorimetric Sensing Ensemble for Heparin. Journal of the American Chemical Society 124(31) (2002): 9014-9015.
- [114] Suksai, C. and Tuntulani, T. Chromogenic anion sensors. Chemical Society Reviews 32(4) (2003).
- [115] Zhu, L., Zhong, Z., and Anslyn, E.V. Guidelines in Implementing Enantioselective Indicator-Displacement Assays for α -Hydroxycarboxylates and Diols. Journal of the American Chemical Society 127(12) (2005): 4260-4269.
- [116] Zhang, S. and Glass, T.E. An indicator displacement assay with independent dual wavelength emission. Tetrahedron letters 51(1) (2010): 112-114.
- [117] Minami, T., Emami, F., Nishiyabu, R., Kubo, Y., and Anzenbacher, P. Quantitative analysis of modeled ATP hydrolysis in water by a colorimetric sensor array. Chem Commun (Camb) 52(50) (2016): 7838-41.
- [118] Nonaka, A., Horie, S., James, T.D., and Kubo, Y. Pyrophosphate-induced reorganization of a reporter-receptor assembly via boronate esterification; a new strategy for the turn-on fluorescent detection of multi-phosphates in aqueous solution. Organic & Biomolecular Chemistry 6(19) (2008): 3621-3625.
- [119] Springsteen, G. and Wang, B. A detailed examination of boronic acid-diol complexation. Tetrahedron 58(26) (2002): 5291-5300.
- [120] Wu, H. and Jin, L. Assembly of alizarin red S/boric acid ultrathin films based on layered double hydroxide for fluorescence turn on detection of tiopronin. Journal of Materials Chemistry C 4(16) (2016): 3415-3421.
- [121] Tomsho, J.W. and Benkovic, S.J. Elucidation of the mechanism of the reaction between phenylboronic acid and a model diol, Alizarin Red S. J Org Chem 77(5) (2012): 2098-106.
- [122] Feng, C., Wang, F., Dang, Y., Xu, Z., Yu, H., and Zhang, W. A Self-Assembled Ratiometric Polymeric Nanoprobe for Highly Selective Fluorescence Detection of Hydrogen Peroxide. Langmuir 33(13) (2017): 3287-3295.
- [123] Springsteen, G. and Wang, B. Alizarin Red S. as a general optical reporter for studying the binding of boronic acids with carbohydrates. Chemical Communications (17) (2001): 1608-1609.
- [124] Kaushik, R., et al. Alizarin red S-zinc(ii) fluorescent ensemble for selective detection of hydrogen sulphide and assay with an H₂S donor. RSC Advances 5(97) (2015): 79309-79316.
- [125] Villamil-Ramos, R. and Yatsimirsky, A.K. Selective fluorometric detection of pyrophosphate by interaction with alizarin red S-dimethyltin(IV) complex. Chem Commun (Camb) 47(9) (2011): 2694-6.
- [126] Kubo, Y., Ishida, T., Kobayashi, A., and James, T.D. Fluorescent alizarin-phenylboronic acid ensembles: design of self-organized molecular sensors for metal ions and anions. Journal of Materials Chemistry 15(27-28) (2005).
- [127] Lampard, E.V., et al. Dye Displacement Assay for Saccharides using Benzoxaborole Hydrogels. ChemistryOpen (2018).
- [128] Ngamdee, K., Noipa, T., Martwiset, S., Tuntulani, T., and Ngeontae, W.

- Enhancement of sensitivity of glucose sensors from alizarin–boronic acid adducts in aqueous micelles. Sensors and Actuators B: Chemical 160(1) (2011): 129-138.
- [129] Sun, X., et al. Reaction-based indicator displacement assay (RIA) for the colorimetric and fluorometric detection of hydrogen peroxide. Organic Chemistry Frontiers 4(6) (2017): 1058-1062.
- [130] Kubo, Y., Kobayashi, A., Ishida, T., Misawa, Y., and James, T.D. Detection of anions using a fluorescent alizarin-phenylboronic acid ensemble. Chemical Communications (22) (2005): 2846-2848.
- [131] Arimori, S., Ward, C.J., and James, T.D. A d-glucose selective fluorescent assay. Tetrahedron Letters 43(2) (2002): 303-305.
- [132] Lampard, E.V., et al. Dye Displacement Assay for Saccharides using Benzoxaborole Hydrogels. ChemistryOpen 7(3) (2018): 266-268.
- [133] Mulla, H.R., Agard, N.J., and Basu, A. 3-Methoxycarbonyl-5-nitrophenyl boronic acid: high affinity diol recognition at neutral pH. Bioorganic & Medicinal Chemistry Letters 14(1) (2004): 25-27.
- [134] Jayeoye, T.J., Cheewasedtham, W., Putson, C., and Rujiralai, T. A selective probe based on 3-aminophenyl boronic acid assembly on dithiobis(succinimidylpropionate) functionalized gold nanoparticles for sialic acid detection in human serum. Journal of Molecular Liquids 281 (2019): 407-414.
- [135] Xue, M., Wang, X., Duan, L., Gao, W., Ji, L., and Tang, B. A new nanoprobe based on FRET between functional quantum dots and gold nanoparticles for fluoride anion and its applications for biological imaging. Biosens Bioelectron 36(1) (2012): 168-73.
- [136] Becke, A.D. Density-functional thermochemistry. III. The role of exact exchange. The Journal of Chemical Physics 98(7) (1993): 5648-5652.
- [137] Lee, C., Yang, W., and Parr, R.G. Development of the Colle-Salvetti correlation-energy formula into a functional of the electron density. Physical Review B 37(2) (1988): 785-789.
- [138] Hehre, W.J., Ditchfield, K., and Pople, J.A. Self-consistent molecular orbital methods. XII. Further extensions of gaussian-type basis sets for use in molecular orbital studies of organic molecules. The Journal of Chemical Physics 56(5) (1972): 2257-2261.
- [139] McLean, A.D. and Chandler, G.S. Contracted Gaussian basis sets for molecular calculations. I. Second row atoms, Z=11-18. The Journal of Chemical Physics 72(10) (1980): 5639-5648.
- [140] Barone, V. and Cossi, M. Quantum calculation of molecular energies and energy gradients in solution by a conductor solvent model. Journal of Physical Chemistry A 102(11) (1998): 1995-2001.
- [141] Cossi, M. and Barone, V. Analytical second derivatives of the free energy in solution by polarizable continuum models. Journal of Chemical Physics 109(15) (1998): 6246-6254.
- [142] Cossi, M., Rega, N., Scalmani, G., and Barone, V. Energies, structures, and electronic properties of molecules in solution with the C-PCM solvation model. Journal of Computational Chemistry 24(6) (2003): 669-681.
- [143] Cancès, E., Mennucci, B., and Tomasi, J. A new integral equation formalism for

- the polarizable continuum model: Theoretical background and applications to Isotropic and anisotropic dielectrics. Journal of Chemical Physics 107(8) (1997): 3032-3041.
- [144] Tomasi, J., Mennucci, B., and Cammi, R. Quantum mechanical continuum solvation models. Chemical Reviews 105(8) (2005): 2999-3093.
- [145] Tomasi, J. and Persico, M. Molecular Interactions in Solution: An Overview of Methods Based on Continuous Distributions of the Solvent. Chemical Reviews 94(7) (1994): 2027-2094.
- [146] Rappé, A.K., Casewit, C.J., Colwell, K.S., Goddard, W.A., III, and Skiff, W.M. UFF, a Full Periodic Table Force Field for Molecular Mechanics and Molecular Dynamics Simulations. Journal of the American Chemical Society 114(25) (1992): 10024-10035.
- [147] Adamo, C. and Jacquemin, D. The calculations of excited-state properties with time-dependent density functional theory. Chemical Society Reviews 42(3) (2013): 845-856.
- [148] Laurent, A.D., Adamo, C., and Jacquemin, D. Dye chemistry with time-dependent density functional theory. Physical Chemistry Chemical Physics 16(28) (2014): 14334-14356.
- [149] Dennington, R.K., T.; Millam, J. GaussView, Version 5. 2009, Shawnee Mission, KS: Semichem Inc.
- [150] Frisch, M.J., et al. Gaussian 09, Revision D.01. 2014, Gaussian, Inc.: Wallingford, CT.
- [151] Atala, E., et al. Mechanism of pyrogallol red oxidation induced by free radicals and reactive oxidant species. A kinetic and spectroelectrochemistry study. J Phys Chem B 117(17) (2013): 4870-9.



VITA

NAME Ratanakorn Teerasarunyanon

DATE OF BIRTH 16 January 1989

PLACE OF BIRTH Nakhon Pathom

INSTITUTIONS ATTENDED Ph. D., Chemistry, Chulalongkorn University, Bangkok, Thailand, August 2020
M. SC., Chemistry, Chulalongkorn University, Bangkok, Thailand, August 2014
B. SC., Chemistry, Silpakorn University, Nakhon Pathom, Thailand, March 2011

HOME ADDRESS 44, Moo.1, Thap Luang Sub-district, Mueang Nakhon Pathom District, Nakhon Pathom Province, Thailand, 73000

PUBLICATION 1. R. Teerasarunyanon, L. C. Wilkins, G. Park and F. P. Gabbai, Dalton Trans 2019, 48, 14777-14782.
2. R. Teerasarunyanon, S. Watchasit, C. Suksai, T. Tuntulani and V. Ruangpornvisuti, Inorganic Chemistry Communications 2019, 108, 107502.



APPENDIX

จุฬาลงกรณ์มหาวิทยาลัย
CHULALONGKORN UNIVERSITY

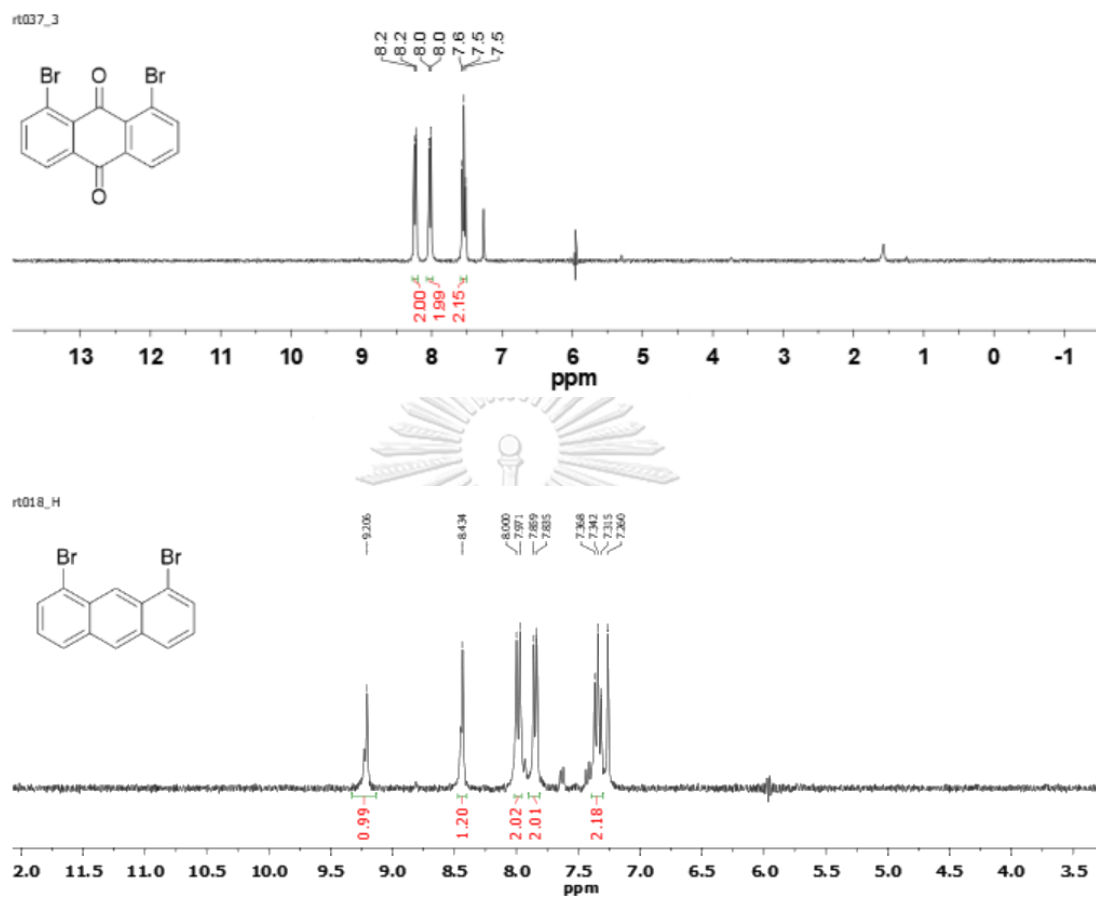
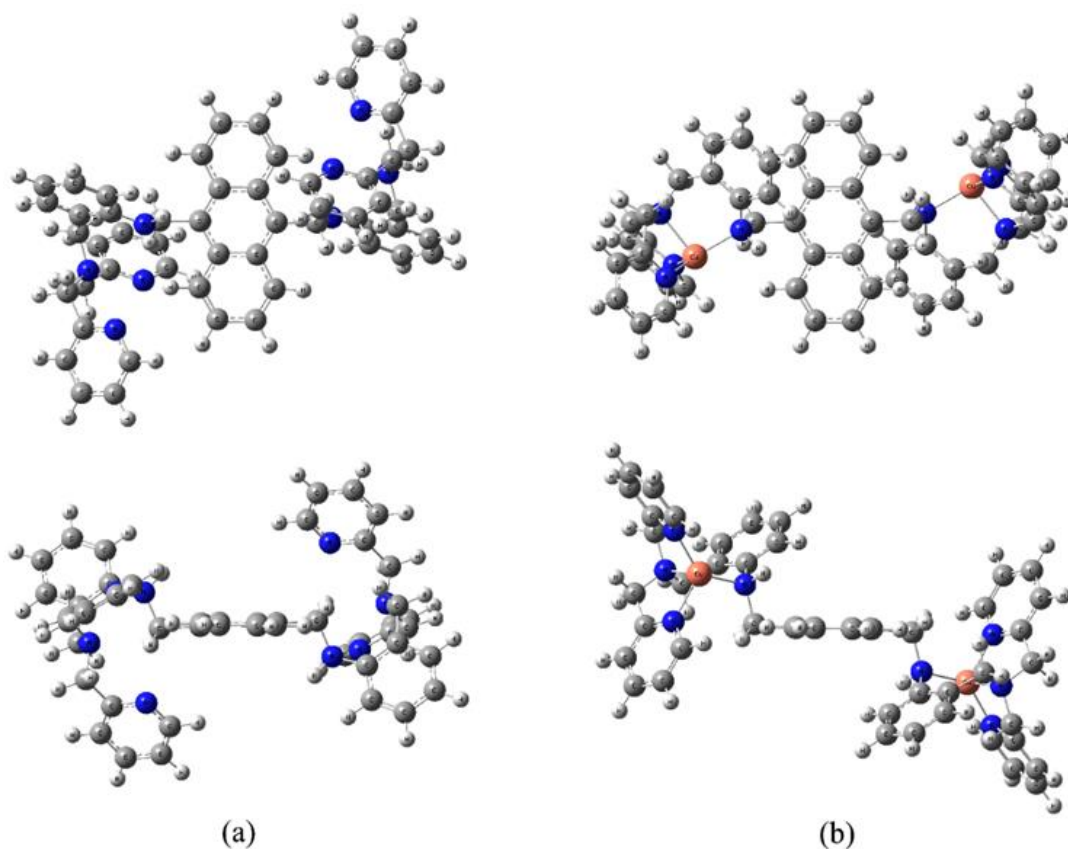
APPENDIX 1: ^1H NMR spectra of related compounds in Project I

Figure S1 ^1H NMR (300 MHz, CDCl_3) spectrum of 1,8-dibromoanthraquinone (top) and 1,8-dibromoanthracene (down).

APPENDIX 2: Geometry optimizations in Project II

Optimized structures of L1 and [CuL1Cu]⁴⁺

The geometry optimizations of free ligand **L1** and its complex with copper(II), [CuL1Cu]⁴⁺ are illustrated in Figure S2.



CHULALONGKORN UNIVERSITY

Figure S2 The CPCM/CAM-B3LYP/6-31G(d)-optimized structures of (a) free L1 (anthracene based tripodal tetramine) and (b) [CuL1Cu]⁴⁺ complex. Their top and side views are located at top and bottom, respectively.

Optimized structures of PGR (denoted by L2)

Since **PGR** can dissociate in water and exist as **L2**, **L2⁻**, **L2²⁻** and **L2³⁻** species that are involved in protonation–deprotonation equilibria depending on the pH of the solution [151], the geometry optimizations of all these species were performed (Figure S3). However, to match the real experimental condition, only the dianion **L2²⁻** (Figure S5), the dominant species in water at pH 7.4, were considered to form the ensemble with $[\text{CuL1Cu}]^{4+}$.

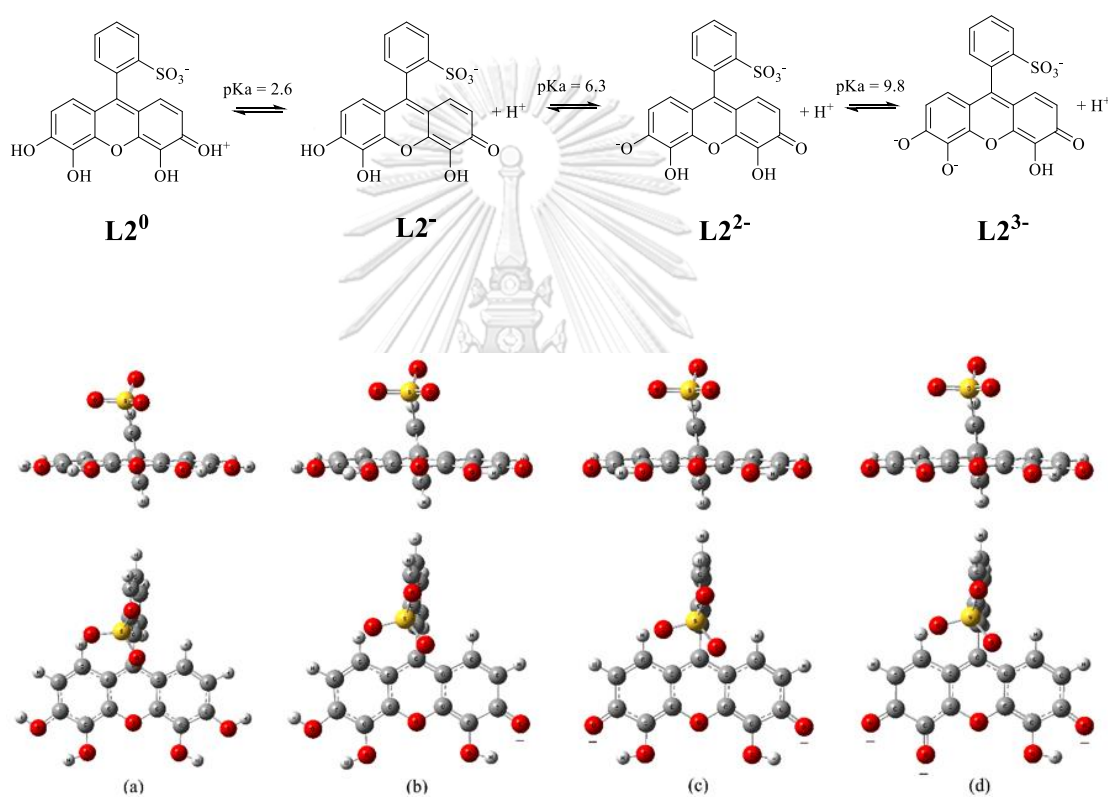


Figure S3 The B3LYP/-31G(d,p)-optimized structures of (a) **L2⁰**, (b) **L2²⁻**, (c) **L2²⁻** and (d) **L2³⁻** species in water. Their top and side views are located at top and bottom, respectively.

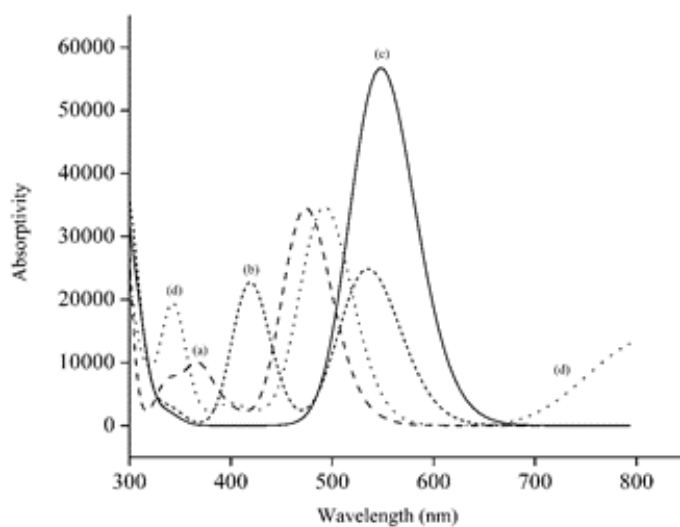


Figure S4 The corresponding simulated UV-vis spectra of (a) $L2^0$, (b) $L2^-$, (c) $L2^{2-}$ and (d) $L2^{3-}$ species in water which are scaled by 1.20.

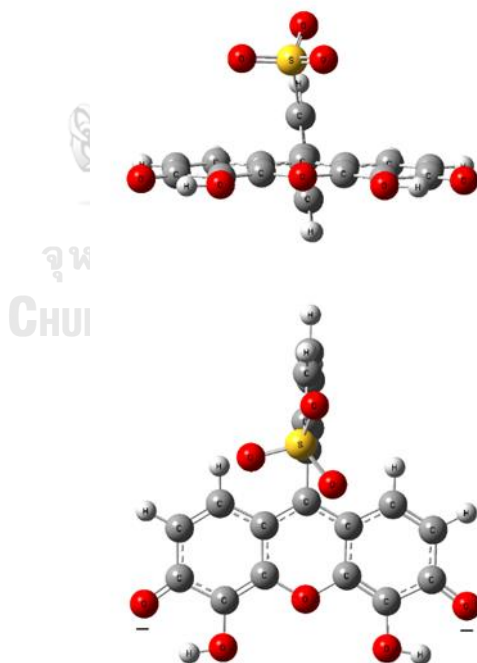
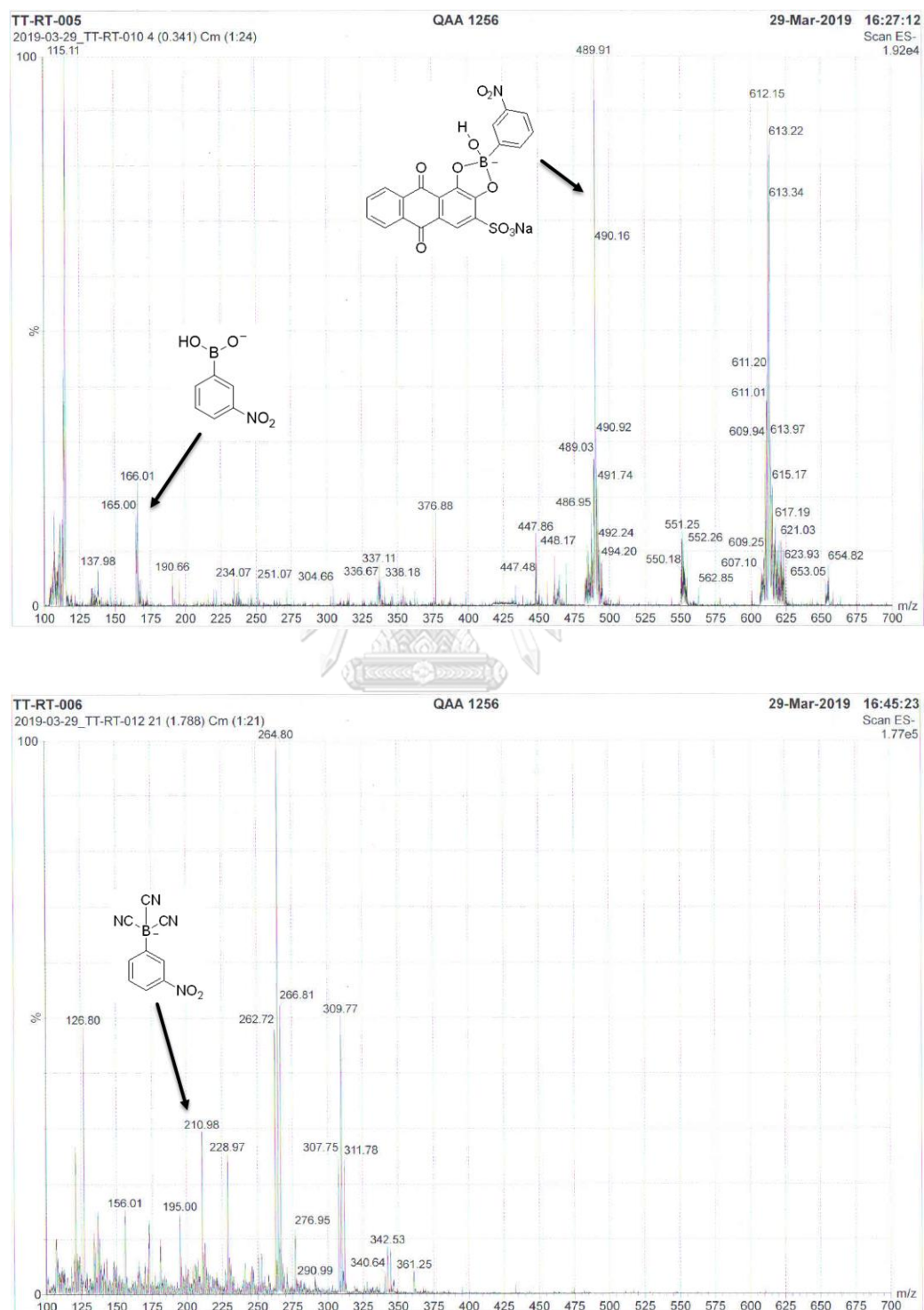


Figure S5 The CPCM/CAM-B3LYP/6-31G(d)-optimized structure of **L2 (PGR)**, as $L2^{2-}$ species.

APPENDIX 3: MS data of ARS-NPBA before and after reacting with CN^- 

APPENDIX 4: The optimized structures of all related species in the formation of ARS–NPBA ensemble and interaction with CN^-

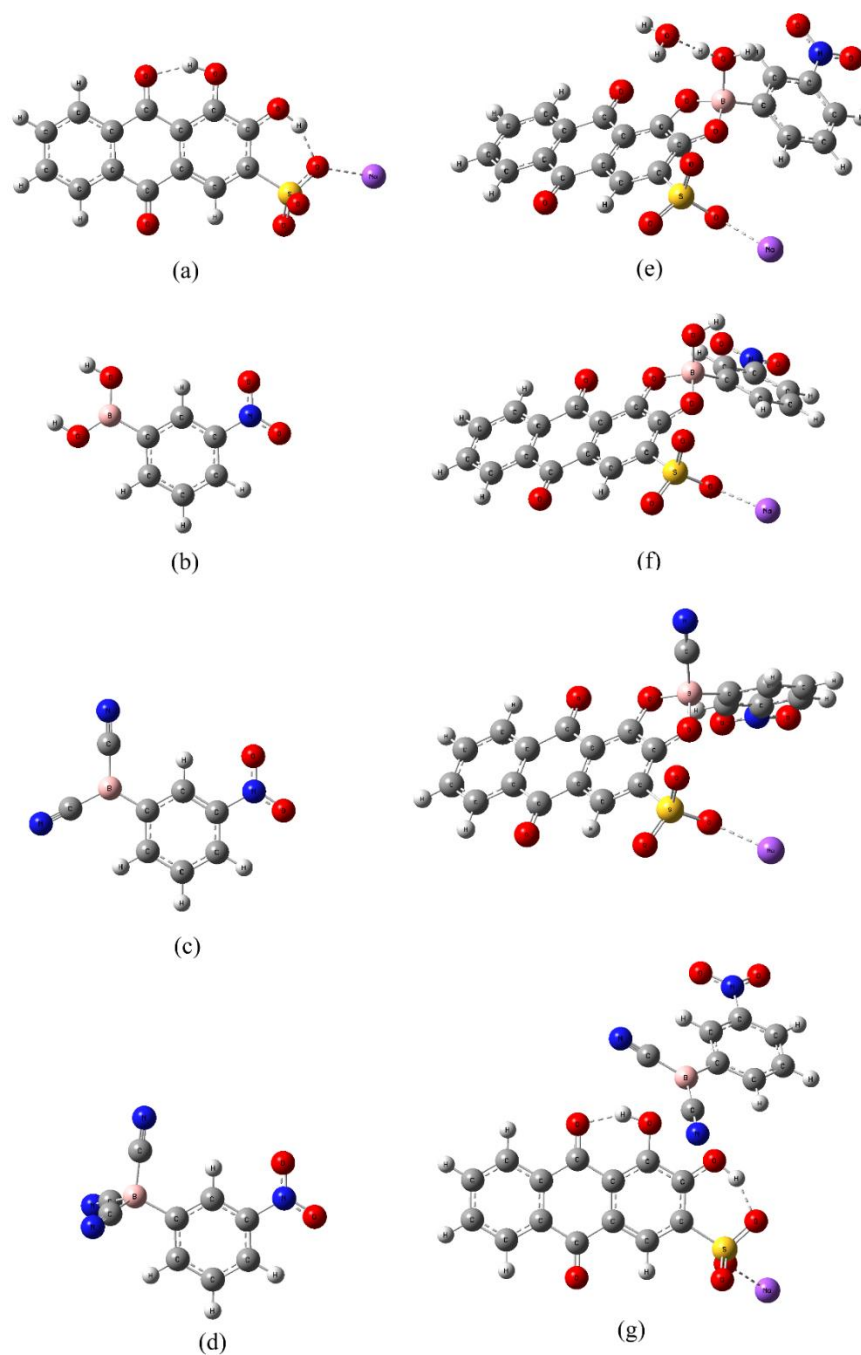


Figure S7 The CPCM/UFF/B3LYP/6-311+G(d,p)-optimized structures of (a) ARS, (b) NPBA, (c) NPBA(CN)₂, (d) NPBA(CN)₃⁻, (e) ARS–NPBA(OH⁻)/H₃O⁺, (f) ARS–NPBA(OH⁻), (g) ARS–NPBA(CN⁻) and (h) ARS/NPBA(CN)₂.

APPENDIX 5: The reaction energies and thermodynamic quantities of **ARS–NPBA** formation and interaction with CN^- ion.

Table S1 The reaction energies and thermodynamic quantities of **ARS–NPBA** formation and interaction with CN^- ion.

Reactions	ΔE_{ZPE}^a	$\Delta H_{298}^{\circ a}$	$\Delta G_{298}^{\circ a}$
<i>Formation of ARS–NPBA(OH⁻):</i>			
$\text{ARS} + \text{NPBA} \rightarrow \text{ARS–NPBA(OH}^-)/\text{H}_3\text{O}^+$	10.21	11.43	20.70
$\text{ARS–NPBA(OH}^-)/\text{H}_3\text{O}^+ \rightarrow \text{ARS–NPBA(OH}^-) + \text{H}_3\text{O}^+$	32.04	32.33	23.41
<i>Reaction with CN⁻:</i>			
$\text{ARS–NPBA(OH}^-) + \text{CN}^- \rightarrow \text{ARS–NPBA(CN}^-) + \text{OH}^-$	26.07	26.38	27.10
$\text{ARS–NPBA(CN}^-) + \text{CN}^- + 2\text{H}_3\text{O}^+ \rightarrow \text{ARS/NPBA(CN)}_2 + 2\text{H}_2\text{O}$	-60.82	-60.45	-53.14
$\text{ARS/NPBA(CN)}_2 \rightarrow \text{ARS} + \text{NPBA(CN)}_2$	1.28	0.44	-8.25
$\text{NPBA(CN)}_2 + \text{CN}^- \rightarrow \text{NPBA(CN)}_3^-$	-48.57	-49.27	-39.20

^a in kcal/mol.

